

# Kernel Cuts: MRF meets Kernel & Spectral Clustering

Meng Tang\*

Dmitrii Marin\*

Ismail Ben Ayed†

Yuri Boykov\*

\*Computer Science, University of Western Ontario, Canada  
mtang73@csd.uwo.ca dmitrii.a.marin@gmail.com†École de Technologie Supérieure, University of Quebec, Canada  
ismail.benayed@etsmtl.ca yuri@csd.uwo.ca

**Abstract**—We propose a new segmentation model combining common regularization energies, *e.g.* Markov Random Field (MRF) potentials, and standard pairwise clustering criteria like Normalized Cut (NC), average association (AA), *etc.* These clustering and regularization models are widely used in machine learning and computer vision, but they were not combined before due to significant differences in the corresponding optimization, *e.g.* spectral relaxation and combinatorial max-flow techniques. On the one hand, we show that many common applications using MRF segmentation energies can benefit from a high-order NC term, *e.g.* enforcing balanced clustering of arbitrary high-dimensional image features combining color, texture, location, depth, motion, *etc.* On the other hand, standard clustering applications can benefit from an inclusion of common pairwise or higher-order MRF constraints, *e.g.* edge alignment, bin-consistency, label cost, *etc.* To address joint energies like NC+MRF, we propose efficient *Kernel Cut* algorithms based on bound optimization. While focusing on graph cut and move-making techniques, our new unary (linear) *kernel* and *spectral* bound formulations for common pairwise clustering criteria allow to integrate them with any regularization functionals with existing discrete or continuous solvers.

## 1 INTRODUCTION AND MOTIVATION

The terms *clustering* and *segmentation* are largely synonyms. The latter is common specifically in computer vision when data points are intensities or some other features  $I_p \in \mathcal{R}^N$  sampled at regularly spaced image pixels or voxels  $p \in \mathcal{R}^M$ . Pixel's location is essential information. Many image segmentation methods working with functions treat  $I_p$  as a mapping  $I : \mathcal{R}^M \rightarrow \mathcal{R}^N$  and process pixel intensity and location in fundamentally different ways. This applies to a large class of regularization methods for image segmentation including discrete MRF-based techniques [1] and continuous variational methods [2]. For example, such methods often use pixel locations to represent the segments geometry and intensities to represent the segments appearance [3], [4], [5], [6].

The term *clustering* is often used in the general context where data point  $I_p$  is an arbitrary observation indexed by integer  $p$ . There are many data clustering techniques [7] widely used outside of computer vision. Variants of *K-means*, spectral techniques, or other clustering methods are also used for image segmentation. They often join pixel's location and observed feature information into one combined data point in  $\mathcal{R}^{N+M}$ . We focus on a well-known group of general and powerful *pairwise clustering* methods [8] based on some estimated *affinities* between all pairs of points.

While independently developed from different methodologies, standard regularization and pairwise clustering methods are de-

finied by objective functions that have many complementary properties reviewed later. Our goal is to combine these functions into a joint energy applicable to image segmentation or general clustering problems. Such objectives could not be combined before due to significant differences in the underlying optimization methods, *e.g.* combinatorial graph cut versus spectral relaxation. While focused on MRF regularization, our approach to integrating pairwise clustering is based on a bound formulation that easily extends to any regularization functional with existing solvers.

We use basic notation applicable to either image segmentation or general data clustering. Let  $\Omega$  be a set of pixels, voxels, or any other points  $p$ . For example, for 2D images  $\Omega$  could be a subset of regularly spaced points in  $\mathcal{R}^2$ . Set  $\Omega$  could also represent data points indices. Assume that every  $p \in \Omega$  comes with an observed feature  $I_p \in \mathcal{R}^N$ . For example,  $I_p$  could be a greyscale intensity in  $\mathcal{R}^1$ , an RGB color in  $\mathcal{R}^3$ , or any other high-dimensional observation. If needed,  $I_p$  could also include pixel's location.

A segmentation of  $\Omega$  can be equivalently represented either as a labeling  $S := (S_p | p \in \Omega)$  including integer node labels  $1 \leq S_p \leq K$  or as a partitioning  $\{S^k\}$  of set  $\Omega$  into  $K$  non-overlapping subsets or segments  $S^k := \{p \in \Omega | S_p = k\}$ .

We combine standard pairwise clustering criteria such as *Average Association* (AA) or *Normalized Cut* (NC) [8] and common regularization functionals such as pairwise or high-order MRF potentials [1], [9]. The general form of our joint energy is

$$E(S) = E_A(S) + \gamma \sum_{c \in \mathcal{F}} E_c(S_c) \quad (1)$$

where the first term is some pairwise clustering objective based on data *affinity matrix* or *kernel*  $A := [A_{pq}]$  with  $A_{pq} := A(I_p, I_q)$  defined by some similarity function  $A(\cdot, \cdot)$ . The second term in (1) is a general formulation of arbitrary MRF *potentials* [10], [11], [12]. Constant  $\gamma$  is a relative weight of this term. Subset  $c \subset \Omega$  represent a *factor* typically made of pixels with nearby locations. Factor labels  $S_c := (S_p | p \in c)$  is a restriction of labeling  $S$  to  $c$ . Potentials  $E_c(S_c)$  for a given set of factors  $\mathcal{F}$  represent various forms of unary, second, or higher order constraints, where factor size  $|c|$  defines the order. Factor features  $\{I_p | p \in c\}$  often work as parameters for potential  $E_c$ . Section 1.1 reviews standard MRF potentials. Note that standard clustering methods encourage balanced segments using ratio-based objectives. They correspond to high-order potential  $E_A(S)$  of order  $|\Omega|$  in (1). Sections 1.2 and 1.3 review standard clustering objectives used in our paper.

### 1.1 Overview of MRF regularization

Probably the most basic MRF regularization potential corresponds to the second-order Potts model [10] used for **edge alignment**

$$\sum_{c \in \mathcal{F}} E_c(S_c) = \sum_{pq \in \mathcal{N}} w_{pq} \cdot [S_p \neq S_q] \approx \|\partial S\| \quad (2)$$

where a set of pairwise factors  $\mathcal{F} = \mathcal{N}$  includes *edges*  $c = \{pq\}$  between pairs of neighboring nodes and  $[\cdot]$  are *Iverson brackets*. Weight  $w_{pq}$  is a discontinuity penalty between  $p$  and  $q$ . It could be a constant or may be set by a decreasing function of intensity difference  $I_p - I_q$  attracting the segmentation boundary to image contrast edges [4]. This is similar to the image-based boundary length in geodesic contours [3], [5].

A useful **bin consistency** constraint enforced by the  $P^n$ -Potts model [11] is defined over an arbitrary collection of high-order factors  $\mathcal{F}$ . Factors  $c \in \mathcal{F}$  correspond to predefined subsets of nodes such as *superpixels* [11] or *bins* of pixels with the same color/feature [13], [14]. The model penalizes inconsistency in segmentation of each factor

$$\sum_{c \in \mathcal{F}} E_c(S_c) = \sum_{c \in \mathcal{F}} \min\{T, |c| - |S_c|^*\} \quad (3)$$

where  $T$  is some threshold and  $|S_c|^* := \max_k |S^k \cap c|$  is the cardinality of the largest segment inside  $c$ . Potential (3) has its lowest value (zero) when all nodes in each factor are within the same segment.

Standard **label cost** [12] is a sparsity potential defined for a single high-order factor  $c = \Omega$ . In its simplest form this potential penalizes the number of distinct segments (labels) in  $S$

$$E_\Omega(S) = \sum_k h_k \cdot [|S^k| > 0] \quad (4)$$

where  $h_k$  could be a constant or a cost for each specific label.

Potentials (2), (3), (4) are only a few examples of regularization terms widely used in combination with powerful discrete solvers like graph cut [10], belief propagation [15], TRWS [16], LP relaxation [17], [18], or continuous methods [19], [20], [21].

Image segmentation methods often combine regularization with a **likelihood term** integrating segments/objects color models. For example, [4], [22] used graph cuts to combine second-order edge alignment (2) with a unary (first-order) appearance term

$$-\sum_k \sum_{p \in S^k} \log P^k(I_p) \quad (5)$$

where  $\{P^k\}$  are given probability distributions. Unary terms like (5) are easy to integrate into any of the solvers above.

If unknown, parameters of models  $\{P^k\}$  in a regularization energy including (5) are often estimated by iteratively minimizing the energy with respect to  $S$  and model parameters [23], [24], [25], [26], [12]. In presence of variable model parameters, (5) can be seen as a *maximum likelihood* (ML) model-fitting term or a *probabilistic K-means* clustering objective [27]. The next section reviews K-means and other standard clustering methods.

### 1.2 Overview of K-means and clustering

Many clustering methods are based on K-means (KM). The most basic iterative KM algorithm [28] can be described as the *block-coordinate descent* for the following *mixed* objective

$$F(S, m) := \sum_k \sum_{p \in S^k} \|I_p - m_k\|^2 \quad (6)$$

combining discrete variables  $S = \{S^k\}_{k=1}^K$  with continuous variables  $m = \{m_k\}_{k=1}^K$  representing clusters “centers”. Norm  $\|\cdot\|$  denotes the Euclidean metric. For any given  $S$  the optimal centers  $\arg \min_m F(S, m)$  are the means

$$\mu_{S^k} := \frac{\sum_{p \in S^k} I_p}{|S^k|} \quad (7)$$

where  $|S^k|$  denotes the segment’s cardinality. Assuming current segments  $S_t^k$  the update operation giving  $\arg \min_S F(S, \mu_{S_t})$

$$\left( \begin{array}{l} \text{basic KM} \\ \text{procedure} \end{array} \right) \quad S_p \leftarrow \arg \min_k \|I_p - \mu_{S_t^k}\| \quad (8)$$

defines the next solution  $S_{t+1}$  as per standard K-means algorithm. This greedy descent technique converges only to a local minimum of KM objective (A-3), which is known to be NP hard to optimize. There are also other approximation methods. Below we review the properties of KM objective (A-3) independently of optimization.

The optimal centers  $m_k$  in (7) allow to represent (A-3) via an equivalent objective of a single argument  $S$

$$\sum_k \sum_{p \in S^k} \|I_p - \mu_{S^k}\|^2 \equiv \sum_k |S^k| \cdot \text{var}(S^k). \quad (9)$$

The sum of squared distances between data points  $\{I_p | p \in S^k\}$  and mean  $\mu_{S^k}$  normalized by  $|S^k|$  gives the *sample variance* denoted by  $\text{var}(S^k)$ . Formulation (9) presents the basic KM objective as a standard *variance criterion* for clustering. That is, K-means attempts to find  $K$  compact clusters with small variance.

K-means can also be presented as a pairwise clustering criteria with Euclidean affinities. The *sample variance* can be expressed as the sum of distances between all pairs of the points. For example, plugging (7) into (9) reduces this KM objective to

$$\sum_k \frac{\sum_{pq \in S^k} \|I_p - I_q\|^2}{2 |S^k|}. \quad (10)$$

Taking the square in the denominator transforms (10) to another equivalent KM energy with Euclidean dot-product affinities<sup>1</sup>

$$\underline{c} = - \sum_k \frac{\sum_{pq \in S^k} \langle I_p, I_q \rangle}{|S^k|}. \quad (11)$$

Alternatively, K-means clustering can be seen as Gaussian model fitting. Formula (5) for normal distributions with variable means  $m_k$  and some fixed variance

$$- \sum_k \sum_{p \in S^k} \log N(I_p | m_k) \quad (12)$$

equals objective (A-3) up to a constant.

Various extensions of objectives (A-3), (9), (10), (11), or (12) lead to many powerful clustering methods such as kernel K-means, average association, and Normalized Cut, see Tab.1 and Fig.34.

#### 1.2.1 Probabilistic K-means (pKM) and model fitting

One way to generalize K-means is to replace squared Euclidean distance in (A-3) by other *distortion* measures  $\|\cdot\|_d$  leading to a general *distortion energy* commonly used for clustering

$$\sum_k \sum_{p \in S^k} \|I_p - m_k\|_d. \quad (13)$$

The optimal value of parameter  $m_k$  may no longer correspond to a *mean*. For example, optimal  $m_k$  for non-squared  $L_2$  metric is a *geometric median* and metric in (25) gives a *mode* [29], [30].

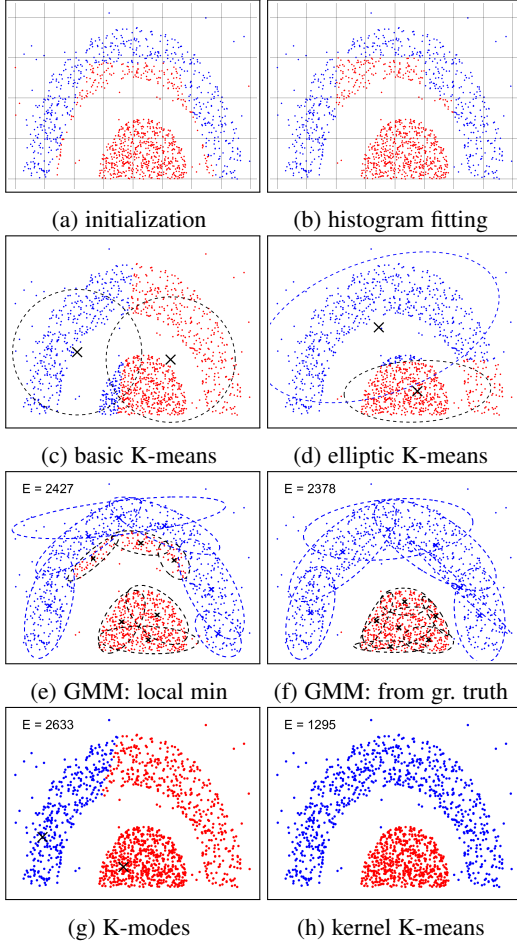


Fig. 1: *Model fitting (14) vs kernel K-means (22)*. Histogram fitting always converges in one step assigning initially dominant bin label (a) to all points in the bin (b): energy (14,15) is minimal at any volume-balanced solution with one label inside each bin [27]. Basic and elliptic K-means (one mode GMM) under-fit the data (c,d). Six mode GMMs over-fit (e) similarly to histograms (b). GMMs have a local minimum issue; ground-truth initialization (f) yields lower energy (14,15). Kernel K-means (21,22) with Gaussian kernel  $k$  in (h) outperforms its weak version (B-1) with explicit estimation of  $\mu$ , that is *K-modes* (B-2) in (g).

A seemingly different way to generalize K-means is to treat both means and covariance matrices for the normal distributions in (12) as variables. This corresponds to the standard *elliptic K-means* [31], [32], [12]. In this case variable model parameters  $\theta_k = \{m_k, \Sigma_k\}$  and data points  $I_p$  are not in the same space. Yet, it is still possible to present elliptic K-means as distortion clustering (13) with “distortion” between  $I_p$  and  $\theta_k$  defined as

$$\|I_p - \theta_k\|_d := -\log N(I_p|\theta_k).$$

Similar distortion measure can be defined for arbitrary probability distributions with any variable parameters  $\theta_k$ . Then, distortion clustering (13) generalizes to ML model fitting objective

$$\sum_k \sum_{p \in S^k} \|I_p - \theta_k\|_d \equiv -\sum_k \sum_{p \in S^k} \log P(I_p|\theta_k) \quad (14)$$

1. We use  $\equiv$  and  $\approx$  for “up to additive constant” relations.

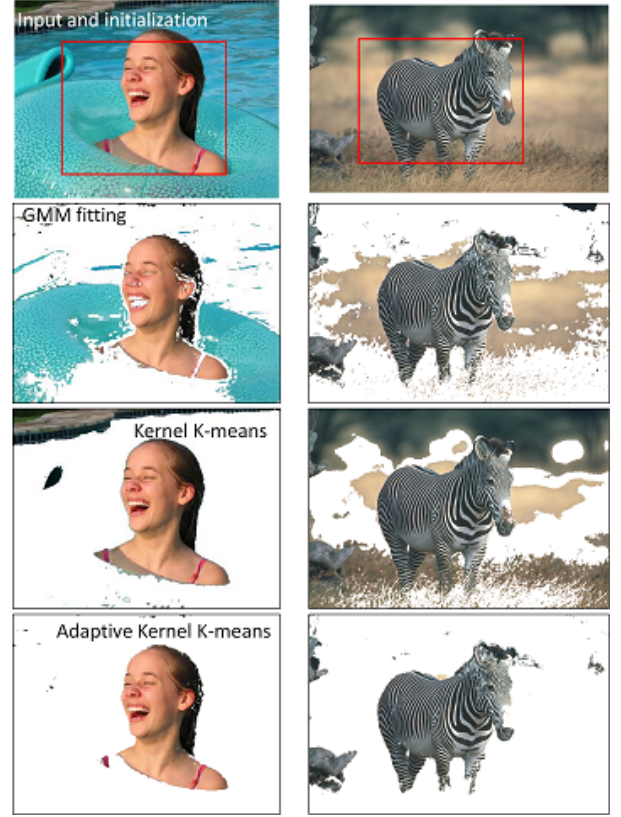


Fig. 2: Without edge alignment (2) iterative GMM fitting [26] shows stronger data over-fit compared to pairwise clustering [8].

which is (5) with explicit model parameters  $\theta_k$ . This formulation suggests *probabilistic K-means*<sup>2</sup> (pKM) as a good idiomatic name for ML model fitting or distortion clustering (13), even though the corresponding parameters  $\theta_k$  are not “means”, in general.

Probabilistic K-means (14) is used in image segmentation with models such as elliptic Gaussians [31], [32], [12], gamma/exponential [25], or other generative models [33]. Zhu-Yuille [23] and GrabCut [26] use pKM with highly descriptive probability models such as GMM or histograms. Information theoretic analysis in [27] shows that in this case pKM objective (14) reduces to the standard *entropy criterion* for clustering

$$\sum_k |S^k| \cdot H(S^k) \quad (15)$$

where  $H(S^k)$  is the entropy of the distribution for  $\{I_p | p \in S^k\}$ .

Intuitively, minimization of the entropy criterion (15) favors clusters with tight or “peaked” distributions. This criterion is widely used in categorical clustering [34] or decision trees [35], [36] where the entropy evaluates histograms over “naturally” discrete features. However, the entropy criterion with either discrete histograms or continuous GMM densities has limitations in the context of *continuous* feature spaces, see Appendix C. Iterative fitting of descriptive models is highly sensitive to local minima [14], [37] and easily over-fits even low dimensional features in  $\mathcal{R}^2$  or  $\mathcal{R}^3$  (e.g. RGB colors), see Figs. 1, 2. This may explain why this approach to clustering is not too common in the learning

2. The name *probabilistic K-means* in the general clustering context was coined by [27]. They formulated (14) after representing distortion energy (13) as ML fitting of Gibbs models  $\frac{1}{Z_d} e^{-\|x-m\|_d}$  for arbitrary integrable metrics.



community. As proposed in (1), instead of entropy criterion we will combine MRF regularization with general pairwise clustering objectives  $E_{\mathcal{A}}$  widely used for balanced partitioning of arbitrary high-dimensional features [8].

### 1.2.2 Kernel K-means (kKM) and pairwise clustering

This section reviews pairwise extensions of K-means (11) such as *kernel K-means* (kKM) and related clustering criteria. In machine learning, kKM is a well established data clustering technique [42], [43], [44], [40], [45], [46] that can identify non-linearly separable structures. In contrast to pKM based on complex models, kKM corresponds to complex (nonlinear) mappings

$$\phi : \mathcal{R}^N \rightarrow \mathcal{H}$$

embedding data  $\{I_p | p \in \Omega\} \subset \mathcal{R}^N$  as points  $\phi_p \equiv \phi(I_p)$  in a higher-dimensional Hilbert space  $\mathcal{H}$ . The original non-linear problem often can be solved by simple linear separators of the embedded points  $\{\phi_p | p \in \Omega\} \subset \mathcal{H}$ . Kernel K-means corresponds to the basic K-means (A-3) in the embedding space

$$F(S, m) = \sum_k \sum_{p \in S^k} \|\phi_p - m_k\|^2. \quad (16)$$

Optimal segment centers  $m_k$  corresponding to the means

$$\mu_{S^k} = \frac{\sum_{q \in S^k} \phi_q}{|S^k|}. \quad (17)$$

reduce (16) to kKM energy of single variable  $S$  analogues to (9)

$$F(S) = \sum_k \sum_{p \in S^k} \|\phi_p - \mu_{S^k}\|^2. \quad (18)$$

Similarly to (10) and (11) one can write pairwise clustering criteria equivalent to (18) based on Euclidean distances  $\|\phi(I_p) - \phi(I_q)\|$  or dot products  $\langle \phi(I_p), \phi(I_q) \rangle$ , which are commonly represented via *kernel function*  $k(x, y)$

$$k(x, y) := \langle \phi(x), \phi(y) \rangle. \quad (19)$$

This kernel corresponds to some inner product in the original data space. Thus, it also defines *Hilbertian metric*<sup>3</sup>

$$\begin{aligned} \|x - y\|_k^2 &:= k(x, x) + k(y, y) - 2k(x, y) \\ &\equiv \|\phi(x) - \phi(y)\|^2 \end{aligned} \quad (20)$$

isometric to the Euclidean metric in the embedding space. Then, pairwise formulations (10) and (11) for K-means in the embedding space (18) can be written with respect to the original data points using isometric kernel distance  $\|\cdot\|_k^2$  in (20)

$$F(S) \equiv \sum_k \frac{\sum_{p, q \in S^k} \|I_p - I_q\|_k^2}{2|S^k|} \quad (21)$$

or using kernel function  $k$  in (19)

$$F(S) \triangleq - \sum_k \frac{\sum_{p, q \in S^k} k(I_p, I_q)}{|S^k|}. \quad (22)$$

The definition of kernel  $k$  in (19) requires embedding  $\phi$ . Since pairwise objectives (21) and (22) are defined for any kernel function in the original data space, it is possible to formulate kKM by directly specifying an affinity function or kernel  $k(x, y)$  rather

than embedding  $\phi(x)$ . This is typical for kKM explaining why the method is called *kernel K-means* rather than *embedding K-means*<sup>4</sup>.

To optimize kKM objectives (18), (21), (22) one can use the basic KM procedure (A-5) iteratively minimizing mixed objective (16) explicitly using embedding  $\phi$

$$\left( \begin{array}{l} \text{explicit kKM} \\ \text{procedure} \end{array} \right) \quad S_p \leftarrow \arg \min_k \|\phi_p - \mu_{S_t^k}\| \quad (23)$$

where  $\mu_{S_t^k}$  is the mean (17) for current segment  $S_t^k$ . Equivalently, this procedure can use kernel  $k$  instead of  $\phi$ . Indeed, as in Section 8.2.2 of [50], the square of the objective in (23) is

$$\|\phi_p\|^2 - 2\phi_p' \mu_{S_t^k} + \|\mu_{S_t^k}\|^2 = -2 \frac{\phi_p' \phi S_t^k}{|S_t^k|} + \frac{S_t^{k'} \phi' \phi S_t^k}{|S_t^k|^2}$$

where we use segment  $S^k$  as an indicator vector, embedding  $\phi$  as an *embedding matrix*  $\phi := [\phi_p]$  where points  $\phi_p \equiv \phi(I_p)$  are columns, and  $'$  denotes the transpose. Since the crossed term is a constant at  $p$ , the right hand side gives an equivalent objective for computing  $S_p$  in (23). Using *kernel matrix*  $\mathcal{K} := \phi' \phi$  and indicator vector  $\mathbf{1}_p$  for element  $p$  we get

$$\left( \begin{array}{l} \text{implicit} \\ \text{kKM} \\ \text{procedure} \end{array} \right) \quad S_p \leftarrow \arg \min_k \frac{S_t^{k'} \mathcal{K} S_t^k}{|S_t^k|^2} - 2 \frac{\mathbf{1}_p' \mathcal{K} S_t^k}{|S_t^k|} \quad (24)$$

where the kernel matrix is directly determined by kernel  $k$

$$\mathcal{K}_{pq} \equiv \phi_p' \phi_q = \langle \phi_p, \phi_q \rangle = k(I_p, I_q).$$

Approach (24) has quadratic complexity  $\mathcal{O}(|\Omega|^2)$  iterations. But, it avoids explicit high-dimensional embeddings  $\phi_p$  in (23) replacing them by kernel  $k$  in all computations, *a.k.a.* the *kernel trick*.

Note that the implicit kKM procedure is guaranteed to decrease pairwise kKM objectives (21) or (22) only for *positive semi-definite* (p.s.d.) kernels. Indeed, (24) is obtained from the standard K-means in the embedding space (23), but this reduction works only if there is some  $\phi$  such that  $k(I_p, I_q) = \langle \phi(I_p), \phi(I_q) \rangle$ . *Mercer's theorem* [51] states that any continuous p.s.d. kernel  $k(x, y)$  corresponds to a dot product in some Hilbert space. Thus, kKM is well-defined either by embeddings  $\phi$  or p.s.d. kernels  $k$ .

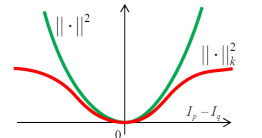
Pairwise energy (21) helps to explain the positive result for kKM with common Gaussian kernel  $k = \exp \frac{-(I_p - I_q)^2}{2\sigma^2}$  in Fig.1(h). Gaussian kernel distance (red plot below)

$$\|I_p - I_q\|_k^2 \propto 1 - k(I_p, I_q) = 1 - \exp \frac{-(I_p - I_q)^2}{2\sigma^2} \quad (25)$$

is a “robust” version of Euclidean metric (green) in basic K-means (10). Thus, Gaussian kKM finds clusters with small local variances, Fig.1(h). In contrast, basic K-means (c) tries to find good clusters with small global variances, which is impossible for non-compact clusters.

**Average association (AA) or distortion (AD):** Equivalent pairwise objectives (21) and (22) suggest natural extensions of kKM. For example, one can replace Hilbertian metric  $\|\cdot\|_k^2$  in (21) by an arbitrary zero-diagonal distortion matrix  $D = [D_{pq}]$  generating *average distortion* (AD) energy

$$E_{ad}(S) := \sum_k \frac{\sum_{p, q \in S^k} D_{pq}}{2|S^k|} \quad (26)$$



3. Such metrics can be isometrically embedded into a Hilbert space [47].

4. This could be a name for some clustering techniques constructing explicit embeddings [48], [49] instead of working with pairwise affinities/kernels.



A. basic K-means (KM) (e.g. [28])	
$\begin{aligned} & \sum_k \sum_{p \in S^k} \ I_p - \mu_{S^k}\ ^2 \\ &= \sum_k \frac{\sum_{p,q \in S^k} \ I_p - I_q\ ^2}{2 S^k } \\ &\stackrel{c}{=} - \sum_k \frac{\sum_{p,q \in S^k} \langle I_p, I_q \rangle}{ S^k } \\ &\stackrel{c}{=} - \sum_k \sum_{p \in S^k} \ln \mathcal{N}(I_p   \mu_{S^k}) \end{aligned}$	<b>Variance criterion</b> $\sum_k  S^k  \cdot \text{var}(S^k)$
<div style="display: flex; justify-content: space-between; align-items: center;"> <span>more complex probability models</span> <span>more complex data representation</span> </div>	
B. probabilistic K-means (pKM)	C. kernel K-means (kKM)
<i>equivalent energy formulations:</i> $\sum_k \sum_{p \in S^k} \ I_p - \theta_k\ _d = - \sum_k \sum_{p \in S^k} \ln \mathcal{P}(I_p   \theta_k)$	<i>equivalent energy formulations:</i> $\begin{aligned} \sum_k \sum_{p \in S^k} \ \phi(I_p) - \mu_{S^k}\ ^2 &= \sum_k \frac{\sum_{p,q \in S^k} \ I_p - I_q\ _k^2}{2 S^k } \\ &\stackrel{c}{=} - \sum_k \frac{\sum_{p,q \in S^k} k(I_p, I_q)}{ S^k } \end{aligned}$
<i>related examples:</i> elliptic K-means [31], [32] geometric model fitting [12] K-modes [29] or mean-shift [39] (weak kKM) Entropy criterion $\sum_k  S^k  \cdot H(S^k)$ [23], [26] <small>for highly descriptive models (GMMs, histograms)</small>	<i>related examples:</i> Average Association or Distortion [38] Average Cut [8] Normalized Cut [8], [40] (weighted kKM) Gini criterion $\sum_k  S^k  \cdot G(S^k)$ [35], [41] <small>for small-width normalized kernels (see Sec. 5.1)</small>

TABLE 1: *K-means and related clustering criteria*: Basic K-means (A) minimizes clusters variances. It works as Gaussian model fitting. Fitting more complex models like elliptic Gaussians [31], [32], [12], exponential distributions [25], GMM or histograms [23], [26] corresponds to *probabilistic K-means* [27] in (B). Pairwise clustering via *kernel K-means* (C) using more complex data representation.

reducing to *kKM* energy (21) for  $D_{pq} = \|I_p - I_q\|_k^2$ . Similarly, p.s.d. kernel  $k$  in (22) can be replaced by an arbitrary pairwise similarity or affinity matrix  $A = [A_{pq}]$  defining standard *average association* (AA) energy

$$E_{aa}(S) := - \sum_k \frac{\sum_{p,q \in S^k} A_{pq}}{|S^k|} \quad (27)$$

reducing to *kKM* objective (22) for  $A_{pq} = k(I_p, I_q)$ . We will also use association between any two segments  $S^i$  and  $S^j$

$$\text{assoc}(S^i, S^j) := \sum_{p \in S^i, q \in S^j} A_{pq} \equiv S^{i'} A S^j \quad (28)$$

allowing to rewrite AA energy (27) as

$$E_{aa}(S) \equiv - \sum_k \frac{\text{assoc}(S^k, S^k)}{|S^k|} \equiv - \sum_k \frac{S^{k'} A S^k}{\mathbf{1}' S^k} \quad (29)$$

The matrix expressions in (28) and (29) represent segments  $S^k$  as indicator vectors such that  $S_p^k = 1$  iff  $S_p = k$  and symbol  $'$  means a transpose. Matrix notation as in (29) will be used for all pairwise clustering objectives discussed in this paper.

*kKM* algorithm (24) is not guaranteed to decrease (27) for improper kernel matrix  $\mathcal{K} = A$ , but general AA and AD energies could be useful despite optimization issues. However, [38] showed that dropping metric and proper kernel assumptions are not essential; there exist p.s.d. kernels with *kKM* energies equivalent (up to constant) to AD (26) and AA (27) for arbitrary associations  $A$  and zero-diagonal distortions  $D$ , as illustrated in Fig. 3.

For example, for any given affinity  $A$  in (27) the *diagonal shift* trick of Roth et al. [38] generates the “kernel matrix”

$$\mathcal{K} = \frac{A + A'}{2} + \delta \cdot I. \quad (30)$$

For sufficiently large scalar  $\delta$  matrix  $\mathcal{K}$  is positive definite yielding a proper discrete kernel  $k(I_p, I_q) \equiv \mathcal{K}_{pq}$

$$k(I_p, I_q) : \chi \times \chi \rightarrow \mathcal{R}$$

for finite set  $\chi = \{I_p | p \in \Omega\}$ . It is easy to check that *kKM* energy (22) with kernel  $k \equiv \mathcal{K}$  in (30) is equivalent to AA energy (27) with affinity  $A$ , up to a constant. Indeed, for any indicator  $X \in \{0, 1\}^{|\Omega|}$  we have  $X'X = \mathbf{1}'X$  implying

$$\frac{X' \mathcal{K} X}{\mathbf{1}' X} = \frac{X' A X}{2(\mathbf{1}' X)} + \frac{X' A' X}{2(\mathbf{1}' X)} + \delta \frac{X' X}{\mathbf{1}' X} = \frac{X' A X}{\mathbf{1}' X} + \delta.$$

Also, formula (56) in Sec. 3.1 can use eigen decomposition of  $\mathcal{K}$  to construct an explicit finite-dimensional Euclidean embedding<sup>5</sup>  $\phi_p \in \mathcal{R}^{|\Omega|}$  satisfying isometry (20) for any p.d. discrete kernel  $k \equiv \mathcal{K}$ . Minimizing *kKM* energy (18) over such isometrically embedded points for  $\mathcal{K}$  in (30) is equivalent to optimizing (22) and, therefore, (27).

Since average distortion energy (26) for arbitrary  $D$  is equivalent to average association for  $A = -\frac{D}{2}$ , it can also be converted to *kKM* with a proper kernel [38]. Using the corresponding kernel matrix (30) and (20) it is easy to derive Hilbertian distortion (metric) equivalent to original distortions  $D$

$$\|I_p - I_q\|_k^2 := \frac{D + D'}{2} + 2\delta(\mathbf{1} \cdot \mathbf{1}' - I) \quad (31)$$

where matrix  $\mathbf{1} \cdot \mathbf{1}'$  has only elements 1.

**Weighted *kKM* and weighted AA:** Weighted K-means [28] is a common extension of KM techniques incorporating some given point weights  $w = \{w_p | p \in \Omega\}$ . In the context of embedded points  $\phi_p$  it corresponds to *weighted kKM* iteratively minimizing the weighted version of the mixed objective in (16)

$$F^w(S, m) := \sum_k \sum_{p \in S^k} w_p \|\phi_p - m_k\|^2. \quad (32)$$

5. Mercer’s theorem is a similar eigen decomposition for continuous p.d. kernels  $k(x, y)$  giving infinite-dimensional Hilbert embedding  $\phi(x)$ . Discrete kernel embedding  $\phi(I_p)$  in (56) has finite dimension  $|\Omega|$ , which is still much higher than the dimension of points  $I_p$ , e.g.  $\mathcal{R}^3$  for colors. Sec. 3.1 also shows even lower dimensional embeddings  $\phi(I_p)$  approximating isometry (20).

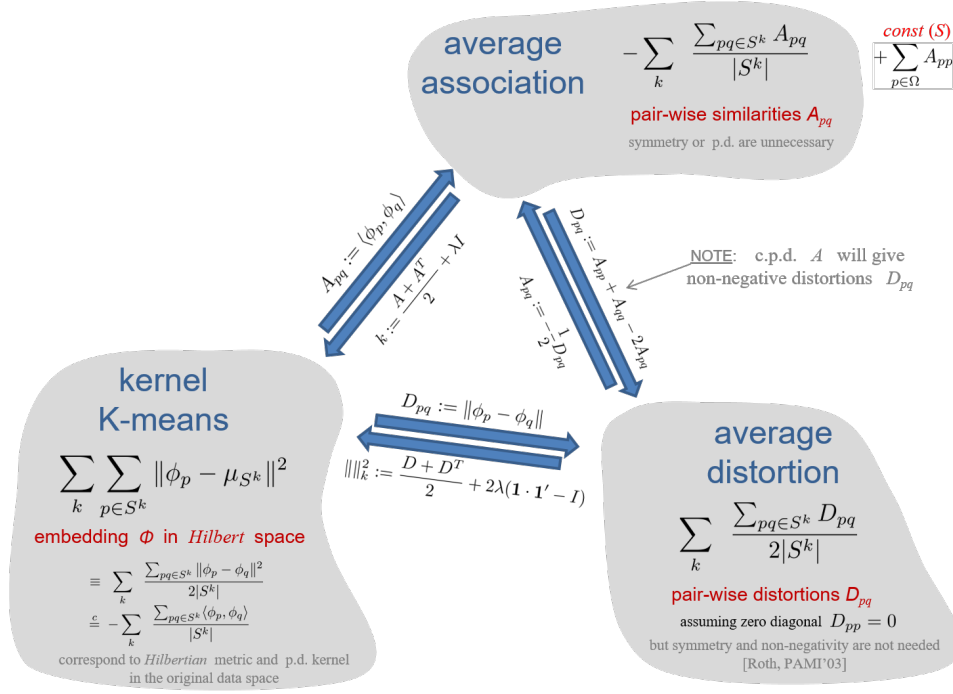


Fig. 3: Equivalence of pairwise clustering methods: *kernel K-means* (kKM), *average distortion* (AD), *average association* (AA) based on Roth et al. [38], see (30), (31). Equivalence of these methods in the general *weighted* case is discussed in Appendix A (Fig. 33).

Optimal segment centers  $m_k$  are now weighted means

$$\mu_{S^k}^w = \frac{\sum_{p \in S^k} w_p \phi_p}{\sum_{p \in S^k} w_p} \equiv \frac{\phi W S^k}{w' S^k} \quad (33)$$

where the matrix formulation has weights represented by column vector  $w \in \mathcal{R}^{|\Omega|}$  and diagonal matrix  $W := \text{diag}(w)$ . Assuming finite dimensional data embedding  $\phi_p \in \mathcal{R}^m$  this formulation uses *embedding matrix*  $\phi := [\phi_p]$  with column vectors  $\phi_p$ . This notation implies two simple identities used in (33)

$$\sum_{p \in S^k} w_p \equiv w' S^k \quad \text{and} \quad \sum_{p \in S^k} w_p \phi_p \equiv \phi W S^k. \quad (34)$$

Inserting weighted means (33) into mixed objective (32) produces pairwise energy formulation for weighted kKM similar to (22)

$$F^w(S) := \sum_k \sum_{p \in S^k} w_p \|\phi_p - \mu_{S^k}^w\|^2 \quad (35)$$

$$\begin{aligned} &\stackrel{c}{=} - \sum_k \frac{\sum_{pq \in S^k} w_p w_q \mathcal{K}_{pq}}{\sum_{p \in S^k} w_p} \quad (36) \\ &\equiv - \sum_k \frac{S^{k'} W \mathcal{K} W S^k}{w' S^k} \end{aligned}$$

where p.s.d kernel matrix  $\mathcal{K} = \phi' \phi$  corresponds to the inner products in the embedding space, i.e.  $\mathcal{K}_{pq} = \phi_p' \phi_q$ .

Replacing p.s.d. kernel with an arbitrary affinity matrix  $A$  defines weighted AA objective generalizing (27) and (29)

$$E_{aa}^w(S) := - \sum_k \frac{S^{k'} W A W S^k}{w' S^k}. \quad (37)$$

Weighted AD can also be defined. Equivalence of kKM, AA, and AD in the general *weighted* case is discussed in Appendix A.

**Other pairwise clustering criteria:** Besides AA there are many other standard pairwise clustering criteria defined by affinity matrices  $A = [A_{pq}]$ . For example, Average Cut (AC)

$$\begin{aligned} E_{ac}(S) &:= \sum_k \frac{\text{assoc}(S^k, \bar{S}^k)}{|S^k|} \equiv \sum_k \frac{S^{k'} A (\mathbf{1} - S^k)}{\mathbf{1}' S^k} \\ &= \sum_k \frac{S^{k'} (D - A) S^k}{\mathbf{1}' S^k} \end{aligned} \quad (38)$$

where  $D := \text{diag}(d)$  is a *degree matrix* defined by node degrees vector  $d := A \mathbf{1}$ . The formulation on the last line (38) comes from the following identity valid for Boolean  $X \in \{0, 1\}^{|\Omega|}$

$$X' D X = X' d.$$

Normalized Cut (NC) [8] in (39) is another well-known pairwise clustering criterion. Both AC and NC can also be reduced to kKM [38], [52], [40]. However, *spectral relaxation* [8] is more common optimization method for pairwise clustering objectives than iterative kKM procedure (24). Due to popularity of NC and spectral relaxation we review them in a dedicated Section 1.3.

### 1.2.3 Pairwise vs. pointwise distortions

Equivalence of kKM to pairwise distortion criteria (26) helps to juxtapose *kernel K-means* with *probabilistic K-means* (Sec.1.2.1) from one more point of view. Both methods generalize the basic K-means (A-3), (10) by replacing Euclidean metric with a more general distortion measure  $\|\cdot\|_d$ . While pKM uses “pointwise” formulation (13) where  $\|\cdot\|_d$  measures distortion between a point and a model, kKM uses “pairwise” formulation (21) where  $\|\cdot\|_d = \|\cdot\|_k^2$  measures distortion between pairs of points.

These two different formulations are equivalent for Euclidean distortion (i.e. basic K-means), but pairwise approach is strictly stronger than the pointwise version using the same Hilbertian distortion  $\|\cdot\|_d = \|\cdot\|_k^2$  for non-Euclidean metrics. The corresponding

pointwise approach is often called *weak kernel K-means* (see Appendix B). Interestingly, weak  $k$ KM with standard Gaussian kernel can be seen as  $K$ -modes [29]. Appendix B also details relations between  $K$ -modes and popular *mean-shift* clustering [39]. An extended version of Table 1 including weighted KM and weak  $k$ KM techniques is given in Figure 34.

### 1.3 Overview of Normalized Cut and spectral clustering

Section 1.2.2 has already discussed  $k$ KM and many related *pairwise clustering* criteria based on specified affinities  $A = [A_{pq}]$ . This section is focused on a related pairwise clustering method, Normalized Cut (NC) [8]. Shi and Malik [8] also popularized pairwise clustering optimization via *spectral relaxation*, which is different from iterative K-means algorithms (23) (24). Note that there are many other popular optimization methods for different clustering energies using pairwise affinities [53], [54], [55], [56], [57], which are outside the scope of this work.

#### 1.3.1 NC objective and its relation to AA and $k$ KM

Normalized Cut (NC) energy [8] can be written as

$$E_{nc}(S) := - \sum_k \frac{assoc(S^k, S^k)}{assoc(\Omega, S^k)} \equiv - \sum_k \frac{S^{k'} A S^k}{\mathbf{1}' A S^k} \quad (39)$$

where *association* (28) is defined by a given *affinity matrix*  $A$ . The second matrix formulation above shows that the difference between NC and AA (29) is in the normalization. AA objective uses denominator  $\mathbf{1}' S^k \equiv |S^k|$ , which is  $k$ -th segment's size. NC (39) normalizes by weighted size. Indeed, using  $d := A' \mathbf{1}$

$$\mathbf{1}' A S^k \equiv d' S^k \equiv \sum_{p \in S^k} d_p$$

where weights  $d = \{d_p | p \in \Omega\}$  are *node degrees*

$$d_p := \sum_{q \in \Omega} A_{pq}. \quad (40)$$

For convenience, NC objective can be formatted similarly to (29)

$$E_{nc}(S) \equiv - \sum_k \frac{S^{k'} A S^k}{d' S^k}. \quad (41)$$

For some common types of affinities where  $d_p \approx \text{const.}$ , e.g.  $K$ -nearest neighbor ( $KNN$ ) graphs, NC and AA objectives (41) and (29) are equivalent. More generally, Bach & Jordan [52], Dhillon et al. [40] showed that NC objective can be reduced to weighted AA or  $k$ KM with specific weights and affinities.

Our matrix notation makes equivalence between NC (41) and weighted AA (37) straightforward. Indeed, objective (41) with affinity  $A$  coincides with (37) for weights  $w$  and affinity  $\tilde{A}$

$$w = d = A' \mathbf{1} \quad \text{and} \quad \tilde{A} = W^{-1} A W^{-1}. \quad (42)$$

Weighted version of  $k$ KM procedure (24) detailed in Appendix A minimizes weighted AA (37) only for p.s.d. affinities, but positive definiteness of  $A$  in NC is not critical. For example, an extension of the *diagonal shift* (30) [38] can convert NC (41) with arbitrary  $A$  to an equivalent NC objective with p.s.d. affinity

$$\mathcal{K} = \frac{A + A'}{2} + \delta \cdot D \quad (43)$$

using *degree matrix*  $D := \text{diag}(d) \equiv W$  and sufficiently large  $\delta$ . Indeed, for indicators  $X \in \{0, 1\}^{|\Omega|}$  we have  $X' D X = d' X$  and

$$\frac{X' \mathcal{K} X}{d' X} = \frac{X' A X}{2(d' X)} + \frac{X' A' X}{2(d' X)} + \delta \frac{X' D X}{d' X} = \frac{X' A X}{d' X} + \delta.$$

Positive definite  $\mathcal{K}$  (43) implies p.d. affinity (42) of weighted AA

$$\tilde{\mathcal{K}} = D^{-1} \mathcal{K} D^{-1} = D^{-1} \left( \frac{A + A'}{2} \right) D^{-1} + \delta D^{-1}. \quad (44)$$

Weighted version of  $k$ KM procedure (24) for this p.d. kernel [58] greedily optimizes NC objective (41) for arbitrary  $A$ .

#### 1.3.2 Spectral relaxation and other optimization methods

There are many methods for approximate optimization of NP-hard pairwise clustering energies besides greedy K-mean procedures. In particular, Shi, Malik, and Yu [8], [59] popularized *spectral relaxation* methods in the context of normalized cuts. Such methods also apply to AA and other problems [8]. For example, similarly to [59] one can rewrite AA energy (27) as

$$E_A(S) = - \text{tr}(Z' A Z) \quad \text{for} \quad Z := \left[ \dots, \frac{S^k}{\sqrt{|S^k|}}, \dots \right]$$

where  $Z$  is a  $\Omega \times K$  matrix of normalized indicator vectors  $S^k$ . Orthogonality  $(S^i)' S^j = 0$  implies  $Z' Z = I_K$  where  $I_K$  is an identity matrix of size  $K \times K$ . Minimization of the *trace* energy above with relaxed  $Z$  constrained to a “unit sphere”  $Z' Z = I_K$  is a simple representative example of *spectral relaxation* in the context of AA. This relaxed trace optimization is a generalization of *Rayleigh quotient* problem that has an exact closed form solution in terms of  $K$  largest eigen vectors for matrix  $A$ . This approach extends to general multi-label weighted AA and related graph clustering problems, e.g. AC and NC [8], [59]. The main computational difficulties for spectral relaxation methods are explicit eigen decomposition for large matrices and integrality gap - there is a final heuristics-based discretization step for extracting an integer solution for the original combinatorial problem from an optimal relaxed solution. For example, one basic discretization heuristic is to run K-means over the row-vectors of the optimal relaxed  $Z$ .

Other optimization techniques are also used for pairwise clustering. Buhmann et al. [60], [38] address the general AD and AA energies via mean field approximation and *deterministic annealing*. It can be seen as a *fuzzy version*<sup>6</sup> of kernel K-means algorithm. In the context of normalized cuts Dhillon et al. [40], [58] use spectral relaxation to initialize  $k$ KM algorithm.

In computer vision it is common to combine various constraints or energy terms into one objective function. Similar efforts were made in the context of pairwise clustering as well. For example, to combine  $k$ KM or NC objectives with Potts regularization [62] normalizes the corresponding pairwise constraints by cluster sizes. This alters the Potts model to fit the problem to a standard trace-based formulation.

Adding non-homogeneous linear constraints into spectral relaxation techniques also requires approximations [63] or model modifications [64]. Exact optimization for the relaxed quadratic ratios (including NC) with arbitrary linear equality constraints is possible by solving a sequence of spectral problems [65].

Our bound optimization approach allows to combine many standard pairwise clustering objectives with any regularization terms with existing solvers. In our framework such pairwise clustering objectives are interpreted as high-order energy terms approximated via linear upper bounds during optimization.

6. Fuzzy version of K-means in Duda et al. [61] generalizes to  $k$ KM.



## 1.4 Our approach summary

We propose to combine standard pairwise clustering criteria such as AA, AC, or NC with standard regularization constraints such as geometric or MRF priors. To achieve this goal, we propose unary (linear) bounds for pairwise clustering objectives that can be easily integrated into any standard regularization algorithms. Below we summarize our motivation and detail our technical contributions.

### 1.4.1 Motivation and Related work

Due to significant differences in applicable optimization algorithms, Normalized Cut (NC) and Markov Random Fields (MRF) techniques are used separately in many applications of vision and learning. They have complementary strengths and weaknesses.

For example, NC can find a balanced partitioning of data points from pairwise affinities for high-dimensional features [8], [66], [67]. In contrast, discrete MRF as well as continuous regularization methods commonly use *model fitting* to partition image features [24], [23], [26], [12]. Such *probabilistic K-means* clustering [27] is well justified when data supports low complexity models, e.g. Gaussians [24] or geometric lines/planes [12]. However, data clustering by fitting complex models like GMM or histograms [23], [26] is highly sensitive to local minima and over-fitting even for low dimensional color features [14]. We made a similar point in our earlier paper [41] comparing [26] to an energy combining the Potts model and AA. Our energy (1) allows a general MRF framework to benefit from widely-known NC balanced clustering of high-dimensional image features. We show potent results for basic formulations of energy (1) with higher-dimensional features like RGBXY, RGBD, RGBM where standard MRF methods fail. In general, kernel-based clustering methods are a prevalent choice in the learning community as model fitting (e.g. EM) becomes intractable for high dimensions.

On the other hand, standard NC applications can also benefit from an inclusion of additional constraints [63], [65], [68]. We show how to add a wide class of standard MRF potentials. For example, standard NC segmentation has weak alignment to contrast edges [67]. While this can be addressed by post-processing, inclusion of the standard pair-wise Potts term [10], [4] offers a principled solution. We show benefits from combining NC with lower and higher-order constraints, such as sparsity or label costs [12]. In the context of a general graph clustering, higher-order consistency terms based on a  $P^n$ -Potts model [11] also give significant improvements.

The synergy of the joint energy (1) can be illustrated by juxtaposing the use of the pixel location information (XY) in standard NC and MRF techniques. The basic pairwise MRF Potts model for images typically works on the nearest-neighbor grids  $\mathcal{N}_4$  or  $\mathcal{N}_8$  where XY information allows accurate contrast edge alignment and enforces “smooth” segment boundaries. Wider connectivity Potts leads to denser graphs with slower optimization and poorer edge localization. In contrast, common NC methods [8] augment pixel features, e.g. color, with XY information using relatively wide kernels for the XY dimension. This encourages segments with spatially “compact” regions. Narrower XY kernels may improve edge alignment [67], but weaken regional color/feature consistency. On the other hand, an extremely large XY kernels ignore spatial information producing color-only clustering with incoherent segments. Combining regional color consistency with spatial coherence in a single NC energy requires a compromise XY kernel width. Our general energy (1) can separate the regional

consistency (e.g. balanced NC clustering term) from the boundary smoothness or edge alignment (e.g. Potts potential). Interestingly, it may still be useful to augment colors with XY in the NC term in (1) since given width XY kernel can separate similar appearance objects at larger distances, see Sec. 6.2.3.

Note that our segmentation model (1) is different from fully connected CRF [69]. Like many MRF/CRF models the method in [69] is inappropriate for clustering as it lacks balancing. Its a denser version of the Potts model giving a trivial solution without a data term. In contrast, high-order pairwise clustering objectives are designed for balanced partitioning. In fact, our unary bounds for such objectives allow to combine them with fully connected CRF or any other MRF/CRF model with known solvers, e.g. mean field approximation used in [69].

Some earlier work also motivates a combination of pairwise clustering (e.g. NC) with MRF potentials like the Potts model [62]. They alter the Potts model to fit it to the standard trace-based formulation of NC. Our general bound approach can combine many pairwise clustering methods with any solvable discrete or continuous regularization potentials.

### 1.4.2 Main contributions

This paper proposes a new energy model (1) for multi-label image segmentation and general clustering, efficient move-making bound optimization algorithms, and demonstrates many useful applications. Our main contributions are outlined below:

- We propose a general multi-label segmentation or clustering energy combining pairwise clustering objectives (e.g. NC) with standard second or higher-order MRF regularization potentials. Pairwise clustering term can enforce balanced partitioning of observed image features and MRF terms can enforce many standard regularization constraints.
- We obtain *kernel* (exact) and *spectral* (approximate) bounds for common pairwise clustering criteria providing two *auxiliary functions* for our joint energy (1). In the context of standard MRF potentials (e.g. Potts, robust  $P^n$ -Potts, label cost) we propose move-making algorithms exploring new generalizations of  $\alpha$ -expansions and  $\alpha\beta$ -swap designed for multi-label bound optimization.<sup>7</sup>
- Our experiments demonstrate that typical NC applications benefit from extra MRF constraints, as well as, MRF segmentation benefit from the high-order NC term encouraging balanced partitioning of image features. In particular, NC+MRF framework works for higher-dimensional image features (e.g. RGBXY, RGBD, RGBM) where standard model-fitting clustering [23], [26], [12] fails.

The rest of the paper is organized as follows. Sections 2 and 3 present our spectral and kernel bounds for (1) and detail combinatorial move making graph cut algorithms for its optimization. Section 4 discusses a number of extensions for our bound optimization approach. Sections 5 analyses kernel and bandwidth selection strategies. Section 6 presents many proof-of-the-concept experiments where either pairwise clustering criteria benefit from the additional MRF constraints or common MRF formulations benefit from an additional clustering term for various high-dimensional features.

7. Our kernel and spectral bounds for pairwise criteria can be also integrated into auxiliary functions with other standard regularization potentials (truncated, cardinality, TV) addressed by discrete (e.g. message passing, relaxations) or continuous (e.g. convex, primal-dual) algorithms.

objective $E_A(S)$	matrix formulation $e(X)$ in $\sum_k e(S^k)$	concave relaxation $\bar{e}(X)$ (51)	$\mathcal{K}$ and $v$ in Lemma 1	kernel bound for $E_A(S)$ at $S_t$
AA (29)	$-\frac{X'AX}{1'X}$	$-\frac{X'(\delta I + A)X}{1'X}$	$\mathcal{K} = \delta I + A, \quad v = 1$	$\sum_k \nabla \bar{e}(S_t^k)' S^k + \text{const}$ for $\nabla \bar{e}$ in (52)
AC (38)	$\frac{X'(D-A)X}{1'X}$	$-\frac{X'(\delta I + A - D)X}{1'X}$	$\mathcal{K} = \delta I + A - D, \quad v = 1$	
NC (41)	$-\frac{X'AX}{d'X}$	$-\frac{X'(\delta D + A)X}{d'X}$	$\mathcal{K} = \delta D + A, \quad v = d$	

TABLE 2: *Kernel bounds* for different pairwise clustering objectives  $E_A(S)$ . The second column shows formulations of these objectives  $E_A(S) \equiv \sum_k e(S^k)$  using functions  $e$  over segment indicator vectors  $S^k \in \{0, 1\}^{|\Omega|}$ . The last column gives a unary (linear) upper bound for  $E_A(S)$  at  $S_t$  based on the first-order Taylor approximation of *concave relaxation* function  $\bar{e} : \mathcal{R}^\Omega \rightarrow \mathcal{R}^1$  (51).

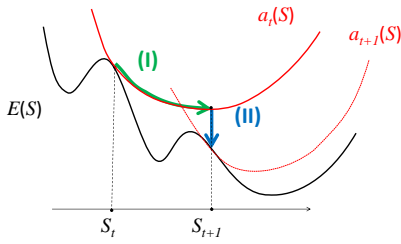


Fig. 4: Iteration  $t$  of the general bound optimization procedure for function  $E(S)$  using auxiliary functions (bounds)  $a_t(S)$ . *Step I* minimizes  $a_t(S)$ . *Step II* computes the next bound  $a_{t+1}(S)$ .

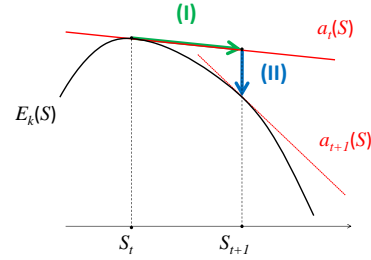


Fig. 5: *K-means as linear bound optimization*: KM procedures (23) or (24) correspond to optimization of linear auxiliary functions  $a_t(S)$  for KM objectives (Theorem 1). Optimum  $S_{t+1}$  is finite since optimization is over Boolean  $S^k \in \{0, 1\}^{|\Omega|}$ .

## 2 KERNEL BOUNDS

### 2.1 Bound optimization and K-means

In general, bound optimizers are iterative algorithms that optimize *auxiliary functions* (upper bounds) for a given energy  $E(S)$  assuming that these auxiliary functions are more tractable than the original difficult optimization problem [70], [71], [72], [37]. Let  $t$  be a current iteration index. Then  $a_t(S)$  is an auxiliary function of  $E(S)$  at current solution  $S_t$  if

$$E(S) \leq a_t(S) \quad \forall S \quad (45a)$$

$$E(S_t) = a_t(S_t). \quad (45b)$$

The auxiliary function is minimized at each iteration  $t$  (Fig. 4)

$$S_{t+1} = \arg \min_S a_t(S). \quad (46)$$

This procedure iteratively decreases original function  $E(S)$  since

$$E(S_{t+1}) \leq a_t(S_{t+1}) \leq a_t(S_t) = E(S_t).$$

We show that standard KM procedures (23), (24) correspond to bound optimization for K-means objective (18). Note that variables  $m_k$  in mixed objective  $F(S, m)$  (16) can be seen as relaxations of segment means  $\mu_{S^k}$  (17) in single-variable KM objective  $F(S)$  (18) since

$$\begin{aligned} \mu_{S^k} &= \arg \min_{m_k} \sum_{p \in S^k} \|\phi_p - m_k\|^2 \\ \text{and } F(S) &= \min_m F(S, m). \end{aligned} \quad (47)$$

**Theorem 1 (bound for KM).** *Standard iterative K-means procedures (23) or (24) can be seen as bound optimization methods for K-means objectives  $F(S)$  (18) (or (22)) using auxiliary function*

$$a_t(S) = F(S, \mu_t) \quad (48)$$

at any current segmentation  $S_t = \{S_t^k\}$  with means  $\mu_t = \{\mu_{S_t^k}\}$ .

*Proof.* (A-4) implies  $a_t(S) \geq F(S)$ . Since  $a_t(S_t) = F(S_t)$  then  $a_t(S)$  is a proper bound for  $F(S)$ . Re-segmentation step (23) gives optimal segments  $S_{t+1}$  minimizing the bound  $a_t(S)$ . Re-centering step minimizing  $F(S_{t+1}, m)$  for fixed segments gives means  $\mu_{t+1}$  defining bound  $a_{t+1}(S)$  for the next iteration.  $\square$

Standard iterations of KM algorithm (23) correspond to bound optimization for objective function  $F(S)$  in (18) as follows. Point re-assignment (23) is *step I* in Fig. 4 or Fig. 5 globally optimizing auxiliary function  $a_t(S) = F(S, \mu_t)$  in (48). Re-computation of means  $\mu_{t+1}$  is *step II* producing auxiliary function  $a_{t+1}(S)$  at  $S_{t+1}$  for the next iteration of bound optimization.

Theorem 1 could be generalized to *probabilistic K-means* [27] by stating that block-coordinate descent for distortion clustering or ML model fitting (14) is a bound optimization [37], [41]. Theorem 1 can also be extended to pairwise and weighted versions of KM. For example, one straightforward extension is to show that  $F^w(S, \mu_t^w)$  (32) with weighted means  $\mu_t^w = \{\mu_{S_t^k}^w\}$  (33) is a bound for weighted KM objective  $F^w(S)$  (35), e.g. see Th. 6 in Appendix A. Then, some bound for pairwise *wkKM* energy (36) can also be derived (Cor. 1, Appendix A). It follows that bounds

can be deduced for many pairwise clustering criteria using their reductions to various forms of  $k$ KM reviewed in Sec. 1.2.2 or 1.3.1.

Alternatively, the next Section 2.2 follows a more direct and intuitive approach to deriving pairwise clustering bounds motivated by the following simple observation. Note that function  $a_t(S)$  in Theorem 1 is *unary* with respect to  $S$ . Indeed, functions  $F(S, m)$  (16) or  $F^w(S, m)$  (32) can be written in the form

$$F(S, m) \equiv \sum_k \sum_p \|\phi_p - m_k\|^2 S_p^k \quad (49)$$

$$F^w(S, m) \equiv \sum_k \sum_p w_p \|\phi_p - m_k\|^2 S_p^k \quad (50)$$

highlighting the sum of unary terms for variables  $S_p^k$ . Thus, bounds for KM or weighted KM objectives are *modular* (linear) function of  $S$ . This simple technical fact has several useful implications that were previously overlooked. For example,

- in the context of bound optimization, KM can be integrated with many regularization potentials whose existing solvers that can easily work with extra unary (linear) terms
- in the context of real-valued relaxation of indicators  $S^k$ , linearity of upper bound  $a_t(S)$  (48) implies that the bounded function  $F(S) \in \mathcal{C}^1$  (22) is *concave*, see Fig. 5.

In Section 2.2 we confirm that many standard pairwise clustering objectives in Sections 1.2.2 and 1.3.1 have *concave relaxations*. Thus, their linear upper bounds easily follow from the corresponding first-order Taylor expansions, see Figure 5 and Table 2.

## 2.2 Kernel Bounds for AA, AC, and NC

The next lemma is needed to state a bound for our joint energy (1) in Theorem 2 for clustering terms AA, AC, or NC in Table 2.

**Lemma 1 (concave relaxation).** Consider function  $\hat{e} : \mathcal{R}^\Omega \rightarrow \mathcal{R}^1$  defined by matrix  $\mathcal{K}$  and vector  $w$  as

$$\hat{e}(X) := -\frac{X' \mathcal{K} X}{w' X}. \quad (51)$$

Function  $\hat{e}(X)$  above is concave over region  $w' X > 0$  assuming that matrix  $\mathcal{K}$  is positive semi-definite. (See Fig. 6)

*Proof.* Lemma 1 follows from the following expression for the Hessian of function  $\hat{e}$

$$\begin{aligned} -\frac{\nabla \nabla \hat{e}}{2} &= \frac{\mathcal{K}}{w' X} - \frac{\mathcal{K} X w' + w X' \mathcal{K}}{(w' X)^2} + \frac{w X' \mathcal{K} X w'}{(w' X)^3} \\ &\equiv \frac{1}{w' X} \left( I - \frac{X w'}{w' X} \right)' \mathcal{K} \left( I - \frac{X w'}{w' X} \right) \end{aligned}$$

which is positive semidefinite for  $w' X > 0$  as long as  $\mathcal{K}$  is.  $\square$

The first-order Taylor expansion at current solution  $X_t$

$$T_t(X) := \hat{e}(X_t) + \nabla \hat{e}(X_t)' (X - X_t)$$

is a bound for the concave function  $\hat{e}(X)$  (51). Its gradient<sup>8</sup>

$$\nabla \hat{e}(X_t) = w \frac{X_t' \mathcal{K} X_t}{(w' X_t)^2} - \mathcal{K} X_t \frac{2}{w' X_t} \quad (52)$$

implies linear bound  $T_t(X)$  for concave function  $\hat{e}(X)$  at  $X_t$

$$T_t(X) \equiv \nabla \hat{e}(X_t)' X. \quad (53)$$

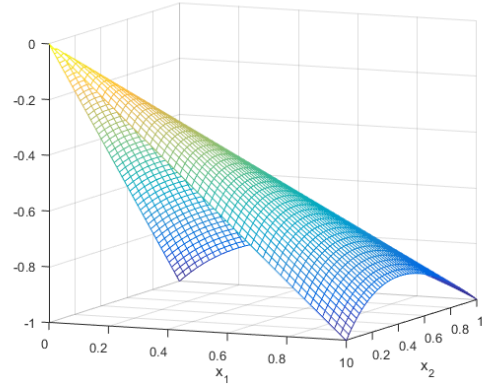


Fig. 6: Example: concave function  $\hat{e}(X) = -\frac{X' X}{1' X}$  for  $X \in [0, 1]^2$ .

As shown in the second column of Table 2, common pairwise clustering objectives defined by affinity matrix  $A$  such as AA (29), AC (38), and NC (41) have the form

$$E_A(S) = -\sum_k e(S^k)$$

with function  $e(X)$  as in (51) from Lemma 1. However, arbitrary affinity  $A$  may not correspond to a positive semi-definite  $\mathcal{K}$  in (51) and  $e(X)$  may not be convex for  $X \in \mathcal{R}^{|\Omega|}$ . However, the *diagonal shift* trick [38] in (30) works here as well. The third column in Table 2 shows concave function  $\hat{e}(X)$  that equals  $e(X)$  for any non-zero Boolean  $X \in \{0, 1\}^{|\Omega|}$ , up to a constant. Indeed, for AA

$$\hat{e}(X) = -\frac{X'(\delta I + A)X}{1' X} = -\frac{X' A X}{1' X} - \delta \stackrel{c}{=} e(X)$$

since  $X' X = 1' X$  for Boolean  $X$ . Clearly,  $\delta I + A$  is p.s.d. for sufficiently large  $\delta$  and Lemma 1 implies that first-order Taylor expansion  $T_t(X)$  (53) is a linear bound for convex function  $\hat{e}(X)$ . Equivalence between  $e$  and  $\hat{e}$  over Booleans allows to use  $T_t(X)$  as a bound for  $e$  when optimizing over indicators  $X$ . Function  $\hat{e} : \mathcal{R}^{|\Omega|} \rightarrow \mathcal{R}^1$  can be described as a *concave relaxation* of the high-order pseudo-boolean function  $e : \{0, 1\}^{|\Omega|} \rightarrow \mathcal{R}^1$ .

Concave relaxation  $\hat{e}$  for AC in Table 2 follows from the same diagonal shift  $\delta I$  as above. But NC requires diagonal shift  $\delta D$  with degree matrix  $D = \text{diag}(d)$  as in (43). Indeed,

$$\hat{e}(X) = -\frac{X'(\delta D + A)X}{d' X} = -\frac{X' A X}{d' X} - \delta \stackrel{c}{=} e(X) \quad (54)$$

since  $X' D X \equiv X' \text{diag}(d) X = d' X$  for any Boolean  $X$ . Clearly,  $\delta D + A$  is p.s.d. for sufficiently large  $\delta$  assuming  $d_p > 0$  for all  $p \in \Omega$ . Concave relaxations and the corresponding Taylor-based bounds for  $E_A(S)$  in Table 2 imply the following theorem.

**Theorem 2 (kernel bound).** For any affinity matrix  $A$  and any current solution  $S_t$  the following is an auxiliary function for joint energy (1) with any clustering term  $E_A(S)$  from Table 2

$$a_t(S) = \sum_k \nabla \hat{e}(S_t^k)' S^k + \gamma \sum_{c \in \mathcal{F}} E_c(S_c) \quad (55)$$

8. Function  $\hat{e}$  and gradient  $\nabla \hat{e}$  are defined only at non-zero indicators  $X_t$  where  $w' X_t > 0$ . We can formally extend  $\hat{e}$  to  $X = \mathbf{0}$  and make the bound  $T_t$  work for  $\hat{e}$  at  $X_t = \mathbf{0}$  with some *supergradient*. However,  $X_t = \mathbf{0}$  is not a problem in practice since it corresponds to an empty segment.



---

**Algorithm 1:**  $\alpha$ -Expansion for Kernel Cut

---

**Input** : Affinity Matrix  $\mathcal{A}$  of size  $|\Omega| \times |\Omega|$ ; initial labeling  $S_0^1, \dots, S_0^K$   
**Output**:  $S^1, \dots, S^K$ : partition of the set  $\Omega$   
 Find p.s.d. matrix  $\mathcal{K}$  as in Table 2. Set  $t := 0$ ;  
**while** not converged **do**  
   Set  $a_t(S)$  to be kernel bound (55) at current partition  $S_t$ ;  
   **for** each label  $\alpha \in \mathcal{L} = \{1, \dots, K\}$  **do**  
     Find  $S_t := \arg \min a_t(S)$  within one  $\alpha$  expansion of  $S_t$ ;  
   **end**  
   Set  $t := t + 1$ ;  
**end**

---

where  $\hat{e}$  and  $\nabla \hat{e}$  are defined in (51), (52) and  $\delta$  is large enough so that the corresponding  $\mathcal{K}$  in Table 2 is positive semi-definite.

### 2.3 Move-making algorithms

Combination (55) of regularization potentials with a unary/linear bound  $\sum_k \nabla \hat{e}(S_t^k)' S^k$  for high-order term  $E_A(S)$  can be optimized with many standard discrete or continuous multi-label methods including graph cuts [10], [73], message passing [74], LP relaxations [17], or well-known continuous convex formulations [19], [20], [21]. We focus on MRF regularizers (see Sec.1.1) commonly addressed by graph cuts [10]. We discuss some details of kernel bound optimization technique using such methods.

Step I of the bound optimization algorithm (Fig.4) using auxiliary function  $a_t(S)$  (55) for energy  $E(S)$  (1) with regularization potentials reviewed in Sec.1.1 can be done via move-making methods [10], [11], [12]. Step II requires re-evaluation of the first term in (55), i.e. the kernel bound for  $E_A$ . Estimation of gradients  $\nabla \hat{e}(S_t^k)$  in (52) has complexity  $O(K|\Omega|^2)$ .

Even though the global optimum of  $a_t$  at step I (Fig.4) is not guaranteed for general potentials  $E_c$ , it suffices to decrease the bound in order to decrease the energy, i.e. (45a) and (45b) imply

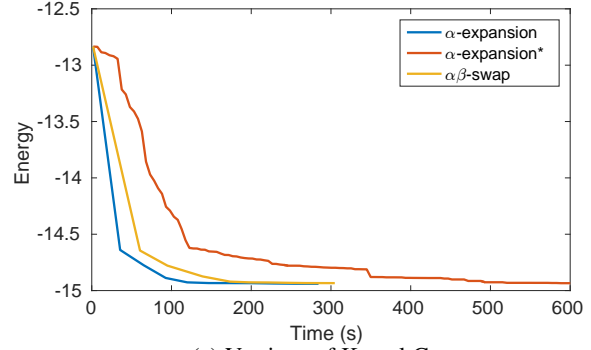
$$a_t(S_{t+1}) \leq a_t(S_t) \quad \Rightarrow \quad E(S_{t+1}) \leq E(S_t).$$

For example, Algorithm 1 shows a version of our kernel cut algorithm using  $\alpha$ -expansion [10] for decreasing bound  $a_t(S)$  in (55). Other moves are also possible, for example  $\alpha\beta$ -swap.

In general, tighter bounds work better. Thus, we do not run iterative move-making algorithms for bound  $a_t$  until convergence before re-estimating  $a_{t+1}$ . Instead, one can reestimate the bound either after each move or after a certain number of moves. One should decide the order of iterative move making and bound evaluation. In the case of  $\alpha$ -expansion, there are at least three options: updating the bound after single expansion step, or after single expansion loop, or after the convergence of  $\alpha$ -expansion. More frequent bound recalculation slows down the algorithm, but makes the bound tighter. The particular choice generally depends on the trade-off between the speed and solution quality. However, in our experiments more frequent update does not always improve the energy, see Fig.7. We recommend updating the bound after a single loop of expansions, see Alg.1. We also evaluated a swap move version of our kernel cut method with bound re-estimation after a complete  $\alpha\beta$ -swaps loop, see Fig.7.

## 3 DATA EMBEDDINGS AND SPECTRAL BOUNDS

This section shows a different bound optimization approach to pairwise clustering and joint regularization energy (1). In contrast to the bounds explicitly using affinity  $A$  or kernel matrices  $\mathcal{K}$  in Sec.2.2, the new approach is based on explicit use of isometric data embeddings  $\phi$ . While the general Mercer theorem guarantees



(a) Versions of Kernel Cut

Compare	against	# of wins	p-value <sup>†</sup>
$\alpha$ -expansion	$\alpha\beta$ -swap	135/200	$10^{-6}$
$\alpha$ -expansion	$\alpha$ -expansion*	182/200 <sup>‡</sup>	$10^{-34\ddagger}$

<sup>†</sup> The probability to exceed the given number of wins by random chance.

<sup>‡</sup> The algorithm stopped due to time limit (may cause incorrect number of wins).

(b) BSDS500 training dataset

Fig. 7: Typical energy evolution wrt different moves and frequency of bound updates.  $\alpha$ -expansion updates the bound after a round of expansions,  $\alpha$ -expansion\* updates the bound after each expansion move. Initialization is a regular  $5 \times 5$  grid of patches.

existence of such possibly infinite dimensional Hilbert space embedding, we show finite dimensional Euclidean embedding

$$\phi \longrightarrow \{\phi_p | p \in \Omega\} \subset \mathcal{R}^{|\Omega|}$$

with exact isometry (19,20) to kernels  $\mathcal{K}$  in Table 2 and lower dimensional embeddings

$$\tilde{\phi} \longrightarrow \{\tilde{\phi}_p | p \in \Omega\} \subset \mathcal{R}^m \quad \text{for } m \leq |\Omega|$$

that can approximate the same isometry with any accuracy level. The embeddings use eigen decompositions of the kernels.

Explicit embeddings allow to formulate exact or approximate spectral bounds for standard pairwise clustering objectives like AA, AC, NC. This approach is very closely related to spectral relaxation, see Sec. 3.3. For example, optimization of our approximate spectral bounds for  $m = K$  is similar to standard discretization heuristics using K-means over eigen vectors [8]. Thus, our bound optimization framework provides justification for such heuristics. More importantly, our spectral bounds allow to optimize joint energy (1) combining pairwise clustering objectives with common regularization terms.

Spectral bound is a useful alternative to kernel bounds in Sec. 2.2 with different complexity and other numerical properties. In particular, spectral bound optimization using lower dimensional Euclidean embeddings  $\tilde{\phi}$  for  $m \ll |\Omega|$  is often less sensitive to local minima. This may lead to better solutions, even though such  $\tilde{\phi}$  only approximately isometric to given pairwise affinities. For  $m = |\Omega|$  the spectral bound is mathematically equivalent to the kernel bound, but numerical representation is different.

### 3.1 Exact and approximate embeddings $\phi$ for $k$ KM

This section uses some standard methodology [75] to build finite-dimensional embedding  $\phi_p \equiv \phi(I_p)$  with exact or approximate isometry (19,20) to any given positive definite kernel  $k$  over finite data set  $\{I_p | p \in \Omega\}$ . As discussed in Sec. 1.2.2,  $k$ KM and other pairwise clustering methods are typically defined by affinities/kernels  $k$  and energy (22) rather than by high-dimensional embeddings  $\phi$  with basic KM formulation (18). Nevertheless, data embeddings  $\phi_p$  could be useful and some clustering techniques explicitly construct them [8], [76], [38], [48], [52], [49]. In particular, if dimensionality of the embedding space is relatively low then the basic iterative KM procedure (23) minimizing (18) could be more efficient than its kernel variant (24) for quadratic formulation (22). Even when working with a given kernel  $k$  it may be algorithmically beneficial to build the corresponding isometric embedding  $\phi$ . Below we discuss finite-dimensional Euclidean embeddings in  $\mathcal{R}^m$  ( $m \leq |\Omega|$ ) allowing to approximate standard pairwise clustering via basic KM.

First, we show an exact Euclidean embedding isometric to a given kernel. Any finite data set  $\{I_p | p \in \Omega\}$  and any given kernel  $k$  define a positive definite *kernel matrix*<sup>9</sup>

$$\mathcal{K}_{pq} = k(I_p, I_q)$$

of size  $|\Omega| \times |\Omega|$ . The *eigen decomposition* of this matrix

$$\mathcal{K} = V' \Lambda V$$

involves diagonal matrix  $\Lambda$  with non-negative eigen values and orthogonal matrix  $V$  whose rows are eigen vectors, see Fig.8(a). Non-negativity of the eigen values is important for obtaining decomposition  $\Lambda = \sqrt{\Lambda} \cdot \sqrt{\Lambda}$  allowing to define the following Euclidean space embedding

$$\phi_p := \sqrt{\Lambda} V_p \in \mathcal{R}^{|\Omega|} \quad (56)$$

where  $V_p$  are column of  $V$ , see Fig.8(a). This embedding satisfies isometry (19,20) since

$$\langle \phi_p, \phi_q \rangle = (\sqrt{\Lambda} V_p)' (\sqrt{\Lambda} V_q) = \mathcal{K}_{pq} = k(I_p, I_q).$$

Note that (56) defines a simple finite dimensional embedding  $\phi_p \equiv \phi(I_p)$  only for subset of points  $\{I_p | p \in \Omega\}$  in  $\mathcal{R}^N$  based on a discrete kernel, *i.e.* matrix  $\mathcal{K}_{pq}$ . In contrast, Mercer's theorem should produce a more general infinite dimensional Hilbert embedding  $\phi(x)$  for any  $x \in \mathcal{R}^N$  by extending the eigen decomposition to continuous kernels  $k(x, y)$ . In either case, however, the embedding space dimensionality is much higher than the original data space. For example,  $\phi_p$  in (56) has dimension  $|\Omega|$ , which is much larger than the dimension of data  $I_p$ , *e.g.* 3 for RGB colors.

Embedding (56) satisfying isometry (19,20) is not unique. For example, any decomposition  $\mathcal{K} = G' G$ , *e.g.* Cholesky [77], defines a mapping  $\phi_p^G := G_p$  with desired properties. Also, rotational matrices  $R$  generate a class of isometric embeddings  $\phi_p^R := R \phi_p$ .

It is easy to build lower dimensional embeddings by weakening the exact isometry requirements (19,20) following the standard *multi-dimensional scaling* (MDS) methodology [75], as detailed below. Consider given rank  $m < |\Omega|$  approximation  $\tilde{\mathcal{K}}$  for kernel matrix  $\mathcal{K}$  minimizing Frobenius norm errors [75]

$$\|\mathcal{K} - \tilde{\mathcal{K}}\|_F := \sum_{p,q \in \Omega} (\mathcal{K}_{pq} - \tilde{\mathcal{K}}_{pq})^2. \quad (57)$$

9. If  $k$  is given as a continuous kernel  $k(x, y) : \mathcal{R}^N \times \mathcal{R}^N \rightarrow \mathcal{R}$  matrix  $\mathcal{K}$  can be seen as its *restriction* to finite data set  $\{I_p | p \in \Omega\} \subset \mathcal{R}^N$ .

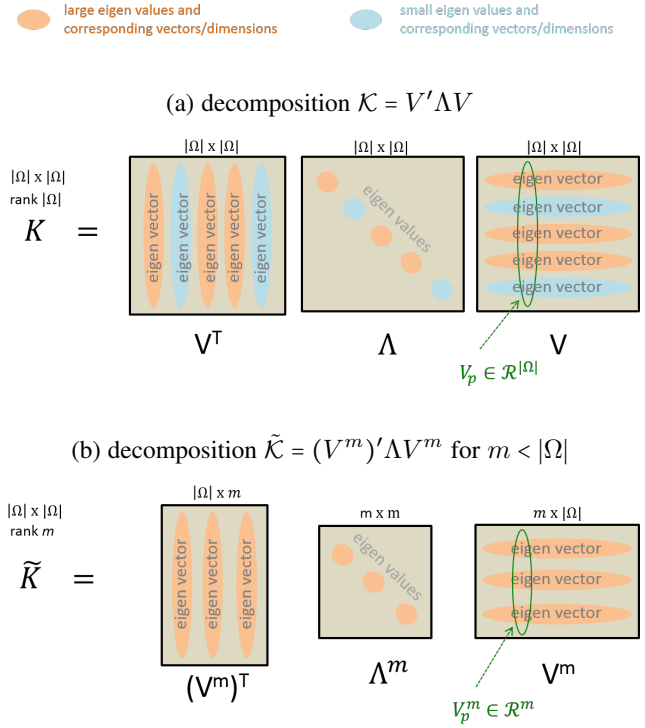


Fig. 8: Eigen decompositions for kernel matrix  $\mathcal{K}$  (a) and its rank  $m$  approximation  $\tilde{\mathcal{K}}$  (b) minimizing Frobenius errors (57) [75]. Decompositions (a,b) allow to build explicit embeddings (56,59) isometric to the kernels, as implied by the Mercer theorem.

It is well known [75], [77] that the minimum Frobenius error is achieved by

$$\tilde{\mathcal{K}} = (V^m)' \Lambda^m V^m$$

where  $V^m$  is a submatrix of  $V$  including  $m$  rows corresponding to the largest  $m$  eigen values of  $\mathcal{K}$  and  $\Lambda^m$  is the diagonal matrix of these eigen values, see Fig.8(b). The corresponding minimum Frobenius error is given by the norm of zeroed out eigen values

$$\|\mathcal{K} - \tilde{\mathcal{K}}\|_F = \sqrt{\lambda_{m+1}^2 + \dots + \lambda_{|\Omega|}^2}. \quad (58)$$

It is easy to check that lower dimensional embedding

$$\tilde{\phi}_p := \sqrt{\Lambda^m} V_p^m \in \mathcal{R}^m \quad (59)$$

is isometric with respect to approximating kernel  $\tilde{\mathcal{K}}$ , that is

$$\langle \tilde{\phi}_p, \tilde{\phi}_q \rangle = \tilde{\mathcal{K}}_{pq} \approx \mathcal{K}. \quad (60)$$

Fig. 9 shows examples of low-dimensional approximate isometry embeddings (59) for a Gaussian kernel. Note that  $\tilde{\phi}_p \in \mathcal{R}^m$  (59) can be obtained from  $\phi_p \in \mathcal{R}^{|\Omega|}$  (56) by selecting coordinates corresponding to dimensions of the largest  $m$  eigen values.

According to (58) lower dimensional embedding  $\tilde{\phi}_p$  in (59) is nearly-isometric to kernel matrix  $\mathcal{K}$  if ignored dimensions have sufficiently small eigen values. Then (59) may allow efficient approximation of kernel K-means. For example, if sufficiently many eigen values are close to zero then a small rank  $m$  approximation  $\tilde{\mathcal{K}}$  will be sufficiently accurate. In this case, we can use basic iterative K-means procedure directly in  $\mathcal{R}^m$  with  $O(|\Omega|m)$  complexity of each iteration. In contrast, each iteration of the standard kernel K-means (22) is  $O(|\Omega|^2)$  in general<sup>10</sup>.

10. Without  $KNN$  or other special kernel accelerations.

objective $E_A(S)$	matrix formulation $\epsilon(X)$ in $\sum_k \epsilon(S^k)$	equivalent $k$ KM (22,36) as in [38], [58]	eigen decomposition $V'\Lambda V = \dots$	embedding in $\mathcal{R}^m$ , $m \leq  \Omega $ with approx. isometry (60)	spectral bound for $E_A(S)$ at $S_t$
AA (29)	$-\frac{X'AX}{1'X}$	$\mathcal{K} = \delta\mathbf{I} + A$	$A$	$\tilde{\phi}_p = \sqrt{\delta\mathbf{I}^m + \Lambda^m} V_p^m$ (61)	$F(S, \mu_t)$ (49) for points $\tilde{\phi}_p$
AC (38)	$\frac{X'(D-A)X}{1'X}$	$\mathcal{K} = \delta\mathbf{I} + A - D$	$D - A$	$\tilde{\phi}_p = \sqrt{\delta\mathbf{I}^m - \Lambda^m} V_p^m$ (62)	
NC (41)	$-\frac{X'AX}{d'X}$	$\mathcal{K} = \delta D^{-1} + D^{-1}AD^{-1}$ weighted, $w_p = d_p$	$D^{-\frac{1}{2}}AD^{-\frac{1}{2}}$	$\tilde{\phi}_p = \sqrt{\frac{\delta\mathbf{I}^m + \Lambda^m}{d_p}} V_p^m$ (66)	$F^w(S, \mu_t^w)$ (50) for points $\tilde{\phi}_p$

TABLE 3: *Spectral bounds* for objectives  $E_A(S)$ . The third column shows p.d. kernel matrices  $\mathcal{K}$  for the equivalent  $k$ KM energy (22). Eigen decomposition for matrices in the forth column defines our Euclidean embedding  $\tilde{\phi}_p \in \mathcal{R}^m$  (fifth column) isometric to  $\mathcal{K}$  (60). Thus, K-means over  $\tilde{\phi}_p$  approximates  $k$ KM (22). Bounds for KM (last column) follow from Th. 1 & 6 where  $\mu_t = \{\mu_{S_t^k}\}$  are means (17) and  $\mu_t^w = \{\mu_{S_t^k}^w\}$  are weighted means (33). Functions  $F(S, m)$  and  $F^w(S, m)$  are modular (linear) w.r.t.  $S$ , see (49,50).

	spectral relaxation [8]	common discretization heuristic [78]	(embedding & K-means)
AA	$A\mathbf{u} = \lambda\mathbf{u}$	$\tilde{\phi}_p := U_p^K \equiv V_p^K$	$\Leftarrow V'\Lambda V = A$
AC	$(D - A)\mathbf{u} = \lambda\mathbf{u}$	$\tilde{\phi}_p := U_p^K \equiv V_p^K$	$\Leftarrow V'\Lambda V = D - A$
NC	$(D - A)\mathbf{u} = \lambda D\mathbf{u}$	$\tilde{\phi}_p := U_p^K \equiv [V^K D^{-\frac{1}{2}}]_p^n$	$\Leftarrow V'\Lambda V = D^{-\frac{1}{2}}AD^{-\frac{1}{2}}$

TABLE 4: *Spectral relaxation* and discretization heuristics for objectives for pairwise clustering objectives  $E_A(S)$  for affinity  $A$ . The corresponding *degree* matrix  $D$  is diagonal with elements  $d_p := \sum_q A_{pq}$ . To extract integer labeling from the relaxed solutions produced by the eigen systems (second column), spectral methods often apply basic KM to some ad hoc data embedding  $\tilde{\phi}$  (last column) based on the first  $K$  unit eigenvectors  $\mathbf{u}$ , the rows of matrix  $U^K$ . While our main text discusses some variants, the most basic idea [8], [78] is to use the columns of  $U^K$  as embedding  $\tilde{\phi}_p$ . For easier comparison, the last column also shows equivalent representations of this embedding based on the same eigen decompositions  $V'\Lambda V$  as those used for our isometry eigenmaps in Tab. 3. In contrast, our embeddings are derived from justified approximations of the original non-relaxed AA, AC, or NC objectives. Note that NC corresponds to a *weighted* case of K-means with data point weights  $w_p = d_p$  [52], [40], see (42) in Section 1.3.1.

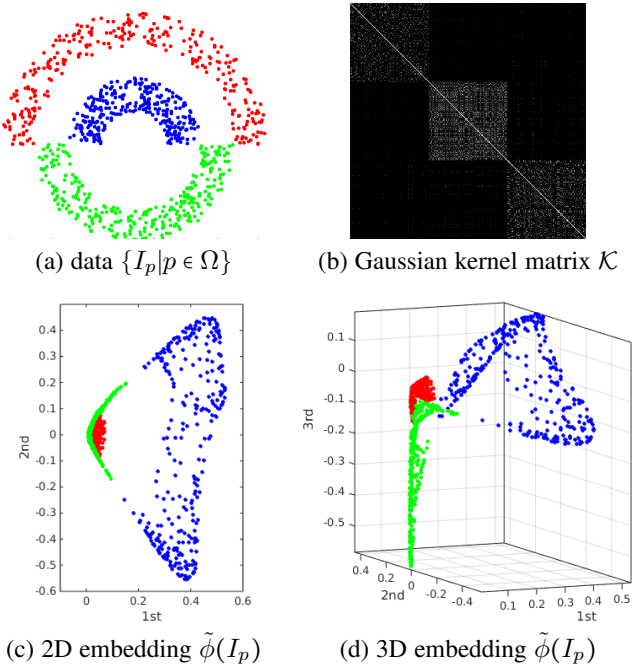


Fig. 9: Low-dimensional Euclidean embeddings (59) for  $m = 2$  and  $m = 3$  in (c,d) are approximately isometric to a given affinity matrix (b) over the data points in (a). The approximation error (58) decreases for larger  $m$ . While generated by standard MDS methodology [75], it is intuitive to call embeddings  $\phi$  in (56) and (59) as (exact or approximate) *isometry eigenmap* or *eigen isomap*.

There is a different way to justify approximate low-dimensional embedding  $\tilde{\phi}_p$  ignoring small eigen value dimensions in  $\phi_p$ . The exact  $k$ KM for  $\mathcal{K}$  corresponds to a basic K-means for points  $\phi_p$  in (56). This is equivalent to basic K-means in the space of columns  $V_p$  in orthonormal matrix  $V$  using weighted distance

$$\|V_p - \mu\|_\Lambda^2 := \sum_{i=1}^{|\Omega|} \lambda_i (V_p[i] - \mu[i])^2 = \|\phi_p - \sqrt{\Lambda}\mu\|^2$$

where index  $[i]$  specifies coordinates of the column vectors. An approximation of  $k$ KM can ignore coordinates for small enough eigen values with low weight in the distance measure above. This is equivalent to K-means for points (59).

### 3.2 Spectral Bounds for AA, AC, and NC

The last Section showed that  $k$ KM clustering with given p.s.d. kernel  $\mathcal{K}$  can be approximated by basic KM over low-dimensional Euclidean embedding  $\tilde{\phi} \in \mathcal{R}^m$  (59) with approximate isometry to  $\mathcal{K}$  (60). Below we use equivalence of standard pairwise clustering criteria to  $k$ KM, as discussed in Sections 1.2.2 and 1.3.1, to derive the corresponding low-dimensional embeddings for AA, AC, NC. Then, equivalence of KM to bound optimization (Theorem 1) allows to formulate our approximate *spectral bounds* for the pairwise clustering and joint energy (1). The results of this Section are summarized in Table 3. For simplicity, assume symmetric affinity matrix  $A$ . It not, equivalently replace  $A$  by  $\frac{A+A'}{2}$ .

**Average association (AA):** Diagonal shift  $\mathcal{K} = \delta\mathbf{I} + A$  in (30) converts AA (29) with  $A$  to equivalent  $k$ KM (22) with p.d. kernel  $\mathcal{K}$ . We seek rank- $m$  approximation  $\tilde{\mathcal{K}}$  minimizing Frobenius error



$\|\mathcal{K} - \tilde{\mathcal{K}}\|_F$ . Provided eigen decomposition  $A = V'\Lambda V$ , equation (59) gives low-dimensional embedding (also in Tab. 3)

$$\tilde{\phi}_p = \sqrt{\delta \mathbf{I}^m + \Lambda^m} V_p^m \quad (61)$$

corresponding to optimal approximation kernel  $\tilde{\mathcal{K}}$ . It follows that KM (23) over this embedding approximates AA objective (22). Note that the eigenvectors (rows of matrix  $V$ , Fig. 8) also solve the spectral relaxation for AA in Tab. 4. However, ad hoc discretization by KM over points  $V_p^K$  may differ from the result for points (61).

**Average cut (AC):** As follows from objective (38) and diagonal shift (30) [38], average cut clustering for affinity  $A$  is equivalent to minimizing  $k$ KM objective with kernel  $\mathcal{K} = \delta \mathbf{I} + A - D$  where  $D$  is a diagonal matrix of node degrees  $d_p = \sum_q A_{pq}$ . Diagonal shift  $\delta \mathbf{I}$  is needed to guarantee positive definiteness of the kernel. Eigen decomposition for  $D - A = V'\Lambda V$  implies  $\mathcal{K} = V'(\delta \mathbf{I} - \Lambda)V$ . Then, (59) implies rank- $m$  approximate isometry embedding (also in Tab. 3)

$$\tilde{\phi}_p = \sqrt{\delta \mathbf{I}^m - \Lambda^m} V_p^m \quad (62)$$

using the same eigenvectors (rows of  $V$ ) that solve AC's spectral relaxation in Tab. 4. However, standard discretization heuristic using KM over  $\tilde{\phi}_p = V_p^K$  may differ from the results for our approximate isometry embedding  $\tilde{\phi}_p$  (62) due to different weighting.

**Normalized cut (NC):** According to [40] and a simple derivation in Sec. 1.3.1 normalized cut for affinity  $A$  is equivalent to weighted  $k$ KM with kernel  $\mathcal{K} = \delta D^{-1} + D^{-1}AD^{-1}$  (44) and node weights  $w_p = d_p$  based on their degree. Weighted  $k$ KM (36) can be interpreted as KM in the embedding space with weights  $w_p$  for each point  $\phi_p$  as in (32,33). The only issue is computing  $m$ -dimensional embeddings approximately isometric to  $\mathcal{K}$ . Note that previously discussed solution  $\tilde{\phi}$  in (59) uses eigen decomposition of matrix  $\mathcal{K}$  to minimize the sum of quadratic errors between  $\mathcal{K}_{pq}$  and approximating kernel  $\tilde{\mathcal{K}}_{pq} = \langle \tilde{\phi}_p, \tilde{\phi}_q \rangle$ . This solution may still be acceptable, but in the context of weighted points it seems natural to minimize an alternative approximation measure taking  $w_p$  into account. For example, we can find rank- $m$  approximate affinity matrix  $\tilde{\mathcal{K}}$  minimizing the sum of weighted squared errors

$$\sum_{pq \in \Omega} w_p w_q (\mathcal{K}_{pq} - \tilde{\mathcal{K}}_{pq})^2 = \|D^{\frac{1}{2}}(\mathcal{K} - \tilde{\mathcal{K}})D^{\frac{1}{2}}\|_F. \quad (63)$$

$\mathcal{K} = \delta D^{-1} + D^{-1}AD^{-1}$  gives an equivalent Frobenius objective

$$\|D^{-\frac{1}{2}}(\delta D + A)D^{-\frac{1}{2}} - D^{\frac{1}{2}}\tilde{\mathcal{K}}D^{\frac{1}{2}}\|_F.$$

Consider rank- $m$  matrix  $\tilde{M} := D^{\frac{1}{2}}\tilde{\mathcal{K}}D^{\frac{1}{2}}$  as a new minimization variable. Its optimal value  $(V^m)'(\delta \mathbf{I}^m + \Lambda^m)V^m$  follows from  $D^{-\frac{1}{2}}(\delta D + A)D^{-\frac{1}{2}} = V'(\delta \mathbf{I} + \Lambda)V$  for eigen decomposition

$$D^{-\frac{1}{2}}AD^{-\frac{1}{2}} \equiv V'\Lambda V. \quad (64)$$

Thus, optimal rank- $m$  approximation kernel  $\tilde{\mathcal{K}}$  is

$$\tilde{\mathcal{K}} = D^{-\frac{1}{2}}(V^m)'(\delta \mathbf{I}^m + \Lambda^m)V^m D^{-\frac{1}{2}}. \quad (65)$$

It is easy to check that  $m$ -dimensional embedding (also in Tab. 3)

$$\tilde{\phi}_p = \sqrt{\frac{\delta \mathbf{I}^m + \Lambda^m}{d_p}} V_p^m \quad (66)$$

is isometric to kernel  $\tilde{\mathcal{K}}$ , that is  $\langle \tilde{\phi}_p, \tilde{\phi}_q \rangle = \tilde{\mathcal{K}}_{pq}$ . Therefore, weighted KM (32) over low-dimensional embedding  $\tilde{\phi}_p$  (66) with weights  $w_p = d_p$  approximates NC objective (41).

**Summary:** The ideas above can be summarized as follows. Assume AA, AC, or NC objectives  $E_A(S)$  with symmetric<sup>11</sup>  $A$ .

The third column in Table 3 shows kernels  $\mathcal{K}$  for equivalent  $k$ KM objectives  $F(S)$  (22,36). Following *eigenmap* approach (Fig. 8), we find rank- $m$  approximate kernel  $\tilde{\mathcal{K}} \approx \mathcal{K}$  minimizing Frobenius error  $\|\tilde{\mathcal{K}} - \mathcal{K}\|_F$  (57) or its weighted version (63) and deduce embeddings  $\tilde{\phi}_p \in \mathcal{R}^m$  (61), (62), (66) satisfying isometry

$$\tilde{\phi}_p' \tilde{\phi}_q = \tilde{\mathcal{K}}_{pq} \approx \mathcal{K}_{pq}.$$

Basic K-means objective  $\tilde{F}(S, m)$  (16,32) for  $\{\tilde{\phi}_p\}$  is equivalent to  $k$ KM energy  $\tilde{F}(S)$  (22,36) for kernel  $\tilde{\mathcal{K}} \approx \mathcal{K}$  and, therefore, approximates the original pairwise clustering objective

$$\tilde{F}(S, \mu_S) \stackrel{c}{=} \tilde{F}(S) \approx F(S) \stackrel{c}{=} E_A(S).$$

Theorem 1 gives unary (linear) bound  $\tilde{F}(S, \mu_t)$  (49,50) for objective  $\tilde{F}(S)$  (16,32). We refer to  $\tilde{F}(S, \mu_t)$  as a *spectral bound* for approximate optimization of  $E_A(S)$  (last column in Table 3).

Similarly to *kernel bound* in Section 2.2, *spectral bound* is useful for optimizing (1). In fact, for  $m = |\Omega|$  the spectral bounds (Tab.3) are algebraically equivalent to the kernel bounds (Tab.2) since  $\tilde{\mathcal{K}} = \mathcal{K}$ , see (58). For  $m < |\Omega|$  we have  $\tilde{\mathcal{K}} \approx \mathcal{K}$  and  $\tilde{F} \approx F$ . Therefore, we can iteratively minimize energy  $E(S)$  (1) by applying bound optimization to its *spectral approximation*

$$\tilde{E}(S) = \tilde{F}(S) + \gamma \sum_{c \in \mathcal{F}} E_c(S_c) \quad (67)$$

or its *weighted spectral approximation*

$$\tilde{E}(S) = \tilde{F}^w(S) + \gamma \sum_{c \in \mathcal{F}} E_c(S_c). \quad (68)$$

**Theorem 3 (spectral bound).** For any affinity matrix  $A$  assume sufficiently large diagonal shift  $\delta$  generating p.s.d. kernel  $\mathcal{K}$  as in Table 3. Then, auxiliary function

$$\tilde{a}_t(S) = \tilde{F}(S, \mu_t) + \gamma \sum_{c \in \mathcal{F}} E_c(S_c) \quad (69)$$

using  $\tilde{F}(S, m)$  (49,50) with embedding  $\{\tilde{\phi}_p\} \subset \mathcal{R}^m$  in Tab. 3 is a bound for joint energy (67,68) approximating (1) as  $m \rightarrow |\Omega|$ .

Approximation quality (58) depends on omitted eigen values  $\lambda_i$  for  $i > m$ . Representative examples in Fig. 10 show that relatively few eigen values may dominate the others. Thus, practically good approximation with small  $m$  is possible. Larger  $m$  are computationally expensive since more eigen values/vectors are needed. Interestingly, smaller  $m$  may give better optimization since K-means in higher-dimensional spaces may be more sensitive to local minima. Thus, spectral bound optimization for smaller  $m$  may find solutions with lower energy, see Fig. 11, even though the quality of approximation is better for larger  $m$ .

Similarly to the kernel bound algorithms discussed in Section 2.3 one can optimize the approximate spectral bound (69) for energy (1) using standard algorithms for regularization. This follows from the fact that the first term in (69) is unary (linear). Algorithms 2 shows a representative (approximate) bound optimization technique for (1) using move-making algorithms [79]. Note that for  $\gamma = 0$  (no regularization terms) our bound optimization Algorithm 2 reduces to basic K-means over approximate isometry embeddings  $\{\tilde{\phi}_p\} \subset \mathcal{R}^m$  similar but not identical to common discretization heuristics in spectral relaxation methods.

11. For non-symmetric  $A$  use affinity  $\frac{A+A'}{2}$  giving equivalent objectives.

---

**Algorithm 2:**  $\alpha$ -Expansion for Spectral Cut
 

---

**Input** : Affinity Matrix  $\mathcal{A}$  of size  $|\Omega| \times |\Omega|$ ; initial labeling  $S_0^1, \dots, S_0^K$   
**Output**:  $S^1, \dots, S^K$ : partition of the set  $\Omega$   
 Find top  $m$  eigen values/vectors  $\Lambda^m, V^m$  for a matrix in the  $4^{th}$  col. of Tab. 3;  
 Compute embedding  $\{\tilde{\phi}_p\} \in \mathcal{R}^m$  for some  $\delta$  and set  $t := 0$ ;  
**while** not converged **do**  
   Set  $\tilde{a}_t(S)$  to be the spectral bound (69) at current partition  $S_t$ ;  
   **for each** label  $\alpha \in \mathcal{L} = \{1, \dots, K\}$  **do**  
     Find  $S_t := \arg \min \tilde{a}_t(S)$  within one  $\alpha$  expansion of  $S_t$ ;  
   **end**  
   Set  $t := t + 1$ ;  
**end**

---

### 3.3 Relation to spectral clustering

Our approximation of pairwise clustering such as NC via basic KM over low dimensional embeddings  $\tilde{\phi}_p$  is closely related to popular spectral clustering algorithms [8], [76], [48] using eigen decomposition for various combinations of kernel, affinity, distortion, laplacian, or other matrices. Other methods also build low-dimensional Euclidean embeddings [76], [48], [49] for basic KM using motivation different from isometry and approximation errors with respect to given affinities. We are mainly interested in discussing relations to spectral methods approximately optimizing pairwise clustering criteria such as AA, AC, and NC [8].

Many spectral relaxation methods also use various eigen decompositions to build explicit data embeddings followed by basic K-means. In particular, the smallest or largest eigen vectors for the (generalized) eigenvalue problems in Table 4 give well-known exact solutions for the relaxed problems. In contrast to our approach, however, the final K-means stage in spectral methods is often presented without justification [8], [78], [67] as a heuristic for quantizing the relaxed continuous solutions into a discrete labeling. It is commonly understood that

“... there is nothing principled about using the K-means algorithm in this step” (Sec. 8.4 in [78])

or that

“... K-means introduces additional unwarranted assumptions.” (Sec. 4 in [59])

Also, typical spectral methods use  $K$  eigenvectors solving the relaxed  $K$ -cluster problems followed by KM quantization. In contrast, we choose the number of eigen vectors  $m$  based on Frobenious error for isometry approximation (58). Thus, number  $m$  is independent from the predefined number of clusters.

Below we juxtapose our approximate isometry low-dimensional embeddings in Table 3 with embeddings used for ad-hoc discretization by the standard spectral relaxation methods in Table 4. While such embeddings are similar, they are not identical. Thus, our Frobenious error argument offers a justification and minor corrections for KM heuristics in spectral methods, even though the corresponding methodologies are unrelated. More importantly, our bound formulation allows integration of pairwise clustering with additional regularization constraints (1).

**Embeddings in spectral methods for NC:** Despite similarity, there are differences between our low-dimensional embedding (66) provably approximating kernel  $\mathcal{K} = \delta D^{-1} + D^{-1}AD^{-1}$  for the  $k$ KM formulation of NC [52], [40] and common ad-hoc embeddings used for KM discretization step in the spectral relaxation methods. For example, one such discretization heuristic [8], [78] uses embedding  $\tilde{\phi}_p$  (right column in Tab. 4) defined by the columns of matrix  $U^K$  whose rows are the  $K$  top (unit) eigenvectors of the standard eigen system (left column). It is easy to

verify that the rows of matrix  $VD^{-\frac{1}{2}}$  are non-unit eigenvectors for the generalized eigen system for NC. The following relationship

$$\tilde{\phi}_p = U^K \equiv [V^K D^{-\frac{1}{2}}]^{rn}$$

where operator  $[\cdot]^{rn}$  normalizes matrix rows, demonstrates certain differences between ad hoc embeddings used by many spectral relaxation methods in their heuristic K-means discretization step and justified approximation embedding (66) in Tab. 3. Note that our formulation scales each embedding dimension, i.e. rows in matrix  $V^K D^{-\frac{1}{2}}$ , according to eigen values instead of normalizing these rows to unit length.

There are other common variants of embeddings for the K-means discretization step in spectral relaxation approaches to the normalized cut. For example, [80], [66], [67] use

$$\tilde{\phi}_p = [\Lambda^{-\frac{1}{2}} U]_p^K$$

for discretization of the relaxed NC solution. The motivation comes from the physics-based *mass-spring system* interpretation [80] of the generalized eigenvalue system.

Some spectral relaxation methods motivate their discretization procedure differently. For example, [59], [52] find the closest integer solution to a *subspace* of equivalent solutions for their particular very similar relaxations of NC based on the same eigen decomposition (64) that we used above. Yu and Shi [59] represent the subspace via matrix

$$X' \equiv [\sqrt{\Lambda^m} V^m D^{-\frac{1}{2}}]^{cn}$$

where columns differ from our embedding  $\tilde{\phi}(I_p)$  in (66) only by normalization. Theorem 1 by Bach and Jordan [52] equivalently reformulates the distance between the subspace and integer labelings via a *weighted* K-means objective for embedding

$$\tilde{\phi}_p = \sqrt{\frac{1}{d_p}} V_p^m \quad (70)$$

and weights  $w_p = d_p$ . This embedding is different from (66) only by eigen value scaling.

Interestingly, a footnote in [52] states that NC is equivalent to weighted KM objective (32) for exact isometry embedding

$$\phi_p = \frac{1}{d_p} G_p \in \mathcal{R}^{|\Omega|} \quad (71)$$

based on any decomposition  $A \equiv G'G$ . For example, our exact isometry map (66) for  $m = |\Omega|$  and  $G = \sqrt{\Lambda}VD^{\frac{1}{2}}$  is a special case. While [52] reduce NC to K-means<sup>12</sup>, their low-dimensional embedding  $\tilde{\phi}$  (70) is derived to approximate the subspace of relaxed NC solutions. In contrast, low-dimensional embedding (66) approximates the exact isometry map  $\phi$  ignoring relaxed solutions. It is not obvious if decomposition  $A \equiv G'G$  for the exact embedding (71) can be used to find any approximate lower-dimensional embeddings like (66).

## 4 OTHER OPTIMIZATION IDEAS

This Section outlines several extensions for optimization methods presented in Sec.2 and 3. For example, we vary diagonal shifts  $\delta$  to reduce Frobenious approximation error  $\|\tilde{\mathcal{K}} - \mathcal{K}\|_F$  (58) between the optimal rank- $m$  matrix  $\tilde{\mathcal{K}}$  and kernels  $\mathcal{K} = A + \delta I$ , see Sec.4.1. We

12. KM procedure (23) (weighted version) is not practical for objective (32) for points  $\phi_p$  in  $\mathcal{R}^{|\Omega|}$ . Instead, Dhillon et al. [40] later suggested *pairwise* KM procedure (24) (weighted version) using kernel  $\mathcal{K}_{pq} \equiv \langle \phi_p, \phi_q \rangle$ .

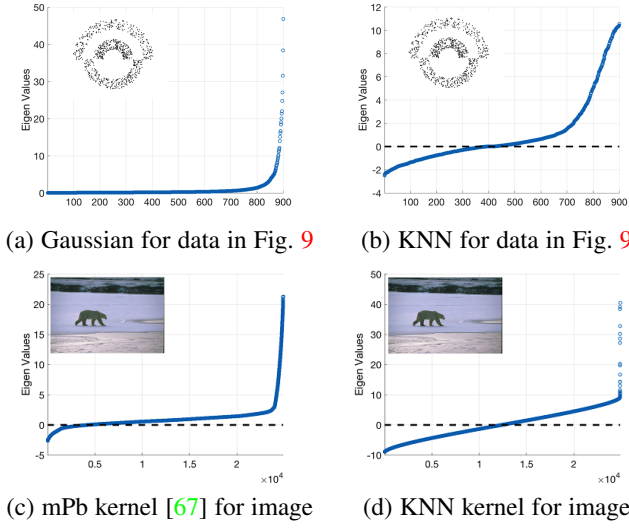


Fig. 10: Spectrum of eigenvalues of typical kernel matrices for synthetic data (top row) or real image color (bottom row). This helps us to select approximate embedding so as to have small approximation error (58). For example, with fixed width gaussian kernel in (a), it suffices to select a few top eigenvectors since the remaining eigenvalues are negligible. Note that the spectrum elevates with increasing diagonal shift  $\delta$  in (61). In principle, we can find the optimal shift for a given number of dimensions  $m$  to minimize approximation error.

also discuss *pseudo-bound* [37] and *trust region* [81] as alternative approximate optimization concepts that may improve our bound optimization framework for high-order energy (1), see Sec.4.2.

#### 4.1 Extensions for spectral bound optimization

We derive low-dimensional embeddings (61), (62), (66) in a principled way allowing to estimate approximation errors with respect to the exact pairwise clustering criteria. Frobenius errors (58) depend on embedding dimensionality  $m$  and diagonal shift  $\delta$  that can increase or decrease all eigen values  $\lambda_i$ , see Fig.10. Unlike typical discretization heuristics in spectral relaxation methods, our choice of  $m$  is not restricted to the fixed number of clusters  $K$ . Moreover, for each fixed  $m$  we can find optimal shift  $\delta$  minimizing the sum of squared norms of omitted eigen values as follows.

For simplicity we focus on AA with symmetric affinity  $A = V' \Lambda V$  even though our technique can be easily extended to AC and NC. Diagonal shift  $\delta$  ensures positive semi-definiteness of the kernel matrix  $\mathcal{K}(\delta) = \delta \mathbf{I} + A$  for an equivalent  $k$ KM. For approximate low dimensional embedding (61) it is enough to guarantee positive semi-definiteness of rank- $m$  approximating kernel  $\tilde{\mathcal{K}}(\delta)$

$$\tilde{\mathcal{K}}(\delta) = (V^m)'(\delta \mathbf{I}^m + \Lambda^m)V^m.$$

Thus one should use  $\delta$  such that all eigenvalues  $\lambda_i$  for  $i \leq m$  are non-negative. Given this restriction one can choose  $\delta$  to minimize Frobenius approximation error (58):

$$\min_{\delta} \|\mathcal{K}(\delta) - \tilde{\mathcal{K}}(\delta)\|_F, \quad \text{s.t.} \quad \delta \geq -\min_{i \leq m} \lambda_i. \quad (72)$$

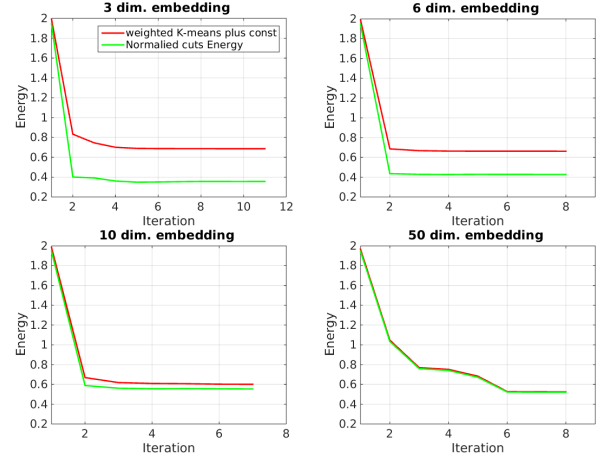


Fig. 11: For data and affinity matrix in Fig. 9, we run weighted K-means with our approximate embedding. The approximation errors  $\|\mathcal{K} - \tilde{\mathcal{K}}\|_F^2 / \|\mathcal{K}\|_F^2$  for 3, 6, 10 and 50 dim. embedding are 58%, 41%, 27% and 3% respectively. We compute weighted K-means energy (up to a const) and normalized cuts energy for solution obtained at each iteration. We observed that normalized cuts energy indeed tends to decrease during iterations of K-means. Even 10 dim. embedding gives good alignment between K-means energy and normalized cuts energy. Higher dimensional embedding gives better energy approximation, but not necessarily better solution with lower energy.

Making use of (58), the objective in (72) is  $\sum_{i=m+1}^{|\Omega|} (\lambda_i + \delta)^2$  giving optimum

$$\delta^* = -\frac{\sum_{i=m+1}^{|\Omega|} \lambda_i}{|\Omega| - m} = -\frac{\text{tr}(\mathcal{K}(0) - \tilde{\mathcal{K}}(0))}{|\Omega| - m}$$

automatically satisfying the constraint in (72). Indeed,  $-\delta^*$  is the mean value of the discarded eigenvalues  $\lambda_i$ , so the shifted discarded eigenvalues  $(\lambda_i + \delta^*)$  must contain both positive and negative values. Since  $\tilde{\mathcal{K}}(\delta^*)$  and  $\Lambda^m$  use the largest eigenvalues  $\{\lambda_i | i \leq m\}$  we have

$$\min_{i \leq m} (\lambda_i + \delta^*) \geq \max_{i > m} (\lambda_i + \delta^*) \geq 0$$

and the constraint in (72) is satisfied. In practice the effect of the diagonal shift mainly depends on the whole spectrum of eigenvalues for a particular affinity matrix, see Figure 10.

#### 4.2 Pseudo-bound and trust region methods

Our bound optimization approach to energy (1) can be extended in several ways. For example, following *pseudo-bound* optimization ideas [37], parametric methods [56] can be used to optimize our bounds with additional *perturbation terms* reducing sensitivity to local minima. It also makes sense to use our (spectral) bounds as an approximating functional for (1) in the context of trust region approach to optimization [81]. We also note that parametric methods can explore all diagonal shifts  $\delta$  alleviating the need for expensive eigen decomposition of large matrices.

**Pseudo-bound optimization:** Consider the following definition introduced in [37].

**Definition 1. (pseudo-bound)** Given energy  $E(S)$  and parameter  $\eta \in \mathcal{R}$ , functional  $B_t(S, \eta)$  is a pseudo-bound for energy



$E(S)$  at current solution  $S_t$  if there exists at least one  $\eta'$  such that  $B_t(S, \eta')$  is an auxiliary function of  $E(S)$  at  $S_t$ .

Instead of using an auxiliary function, one can optimize a family of pseudo-bounds that includes at least one proper bound. This guarantees that original functional  $E(S)$  decreases when the best solution is selected among the global minima for the whole family [37]. In the meanwhile, such pseudo-bounds may approximate  $E(S)$  better than a single auxiliary function, even though they come from the same class of sub-modular (globally optimizable) functionals. The experiments of [37] confirmed that pseudo-bounds significantly outperform the optimization quality obtained by a single auxiliary function in the context of several high-order segmentation functionals, e.g., entropy [82], Bhattacharyya measure [83] and KL divergence [72]<sup>13</sup>. If the pseudo-bounds are monotone w.r.t. parameter  $\eta$ , we can find all global minima for the whole family in polynomial time via parametric max-flow algorithm [56]. This practical consideration is important when building a pseudo-bound family. For instance, [37] built pseudo-bounds by simply adding monotone unary terms  $\eta|S^k|$  to the auxiliary functions. We can use a similar *perturbation term* in the context of auxiliary functions in Table 2 and 3.

As a proof-of-the-concept, we included Figure 12 demonstrating one synthetic binary clustering example. It uses standard NC objective (41) with p.d. Gaussian kernel (requiring no diagonal shift) and no additional regularization terms. Basic kernel bound optimization converges to a weak local minimum, while pseudo-bound optimization over all parameters  $\eta$  in perturbation term  $\eta|S^k|$  achieves a much better solution with lower energy. This toy example suggests that pseudo-bound approach may compete with standard spectral relaxation methods [8].

A different perturbation term is motivated by using diagonal shift as a perturbation parameter  $\eta = \delta$ . Besides improving optimization, efficient search over  $\delta$  may make it unnecessary to compute expensive eigen-value decompositions when estimating diagonal shift for proper p.s.d. kernels/affinities in the third columns of Table 2 and 3. Consider function  $e(X)$  defined by symmetric affinities  $A$  and weights  $w$

$$e(X) := -\frac{X'AX}{w'X}$$

which is similar to  $\bar{e}(X)$  in (51) except that  $A$  is not necessarily positive definite. Thus,  $e(X)$  may not be concave as a function of relaxed continuous argument  $X$ , see Lemma 1. Pseudo-bound for clustering objectives in the general form  $E_A(S) = \sum_k e(S^k)$  can be derived from diagonal shift  $\delta W + A$  for  $W := \text{diag}(w)$  resulting in equivalent objectives.

**Theorem 4 (pseudo-bound).** *Consider pairwise clustering objectives in form  $E_A(S) := \sum_k e(S^k)$ . The following is a pseudo-bound of  $E_A(S)$  at  $S_t$*

$$B_t(S, \delta) \stackrel{c}{=} \sum_k \nabla e(S_t^k)' S^k + \delta \sum_k \frac{(1 - 2S_t^k)' W S^k}{w' S_t^k} \quad (73)$$

becoming a proper auxiliary function for  $\delta \geq -\lambda_0(W^{-\frac{1}{2}}AW^{-\frac{1}{2}})$  where  $\lambda_0$  denotes the smallest eigen value of the matrix. The corresponding pseudo-bound for the joint energy combining high-order clustering term  $E_A$  with regularization terms in (1) is

$$B_t(S, \delta) + \gamma \sum_{c \in \mathcal{F}} E_c(S_c). \quad (74)$$

13. The segmentation functionals considered in [37] are completely different from the pairwise clustering energies we consider in this work

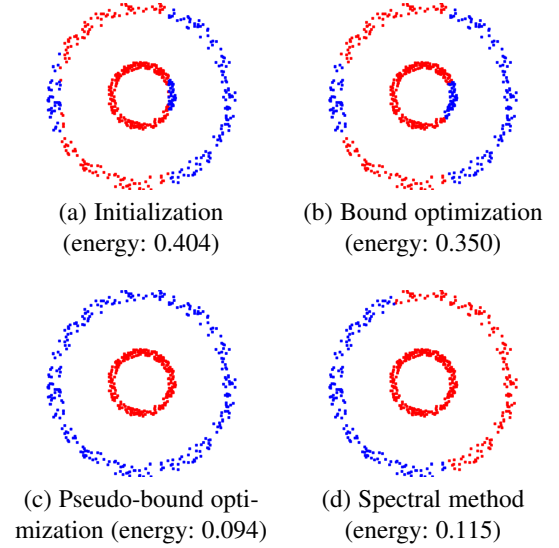


Fig. 12: Normalized cut (NC) objective (41). This proof-of-the-concept example shows that our *pseudo-bound* optimization (c) is less sensitive to local minima compared to the standard  $k$ KM algorithm (bound optimizer) in (b). Pseudo-bound approach can also compete with spectral relaxation methods [8] in (d).

*Proof.* Implied by Lemma 2 (Appendix D) after omitting  $\delta K$ , which is a constant w.r.t.  $S$  not affecting optimization.  $\square$

Theorem 4 provides pseudo-bound (74) for joint energy (1) combining AA, AC, NC objectives in Table 2 with regularization potentials. When the number of segments is  $K = 2$  parametric max-flow methods [56] could be used to explore all distinct optimal solutions  $S(\delta)$  for pseudo-bound (74) for all  $\delta$ . In particular, this search covers  $\delta$  where (74) is a proper bound removing the need for explicitly evaluating  $\lambda_0(D^{-\frac{1}{2}}AD^{-\frac{1}{2}})$  via expensive eigen-value decomposition. However, in contrast to the common perturbation term  $\eta|S^k|$  [37], it is easy to check that the second term in  $B_t(S, \delta)$  (73) is not *monotonic* [56] with respect to  $\delta$ . Thus, there is no guarantee that optimal object segments  $S^k(\delta)$  form a nested sequence w.r.t. parameter  $\delta$  and that the number of such distinct discrete solutions is bounded by  $1 + |\Omega|$ .

Note that a parametric search could also be implemented for  $K > 2$  in the context of move making algorithms, see Section 2.3, using parametric max-flow [56] to explore all  $\delta$  at each expansion or other move [10]. If the number of distinct solutions for all  $\delta$  gets too large at each expansion due to lack of monotonicity, one can use simple practical heuristics. For example, restricted expansion moves can be limited to “monotone” subsets of pixels with either positive or negative unary potential with respect to  $\delta$ .

Pseudo-bound  $B_t(S, \delta)$  (73) could be useful for pairwise clustering without no regularization when monotonicity is not needed to guarantee efficiency. Indeed, for  $K = 2$  a unary potential for each pixel in (73) changes its sign only once as parameter  $\delta$  increases. It is enough to sort all critical values of  $\delta$  changing at least one pixel in order to traverse all (at most  $1 + |\Omega|$ ) distinct solutions for pseudo bound (73) in a linear time. For  $K > 2$  it is easy to check that the optimal label for each pixel changes at most  $K - 1$  times as  $\delta$  increases<sup>14</sup>. Critical values of  $\delta$  for all pixels can

14. The optimal value of a unary potential for each pixels is the lower envelope of  $K$  linear functions of  $\delta$ , which has at most  $K - 1$  breakpoints.

be sorted so that all (at most  $1 + (K - 1)|\Omega|$ ) distinct solutions for pseudo bound (73) can be explored in a linear time.

**Trust region optimization:** Non-monotonicity of the second (perturbation) term in (73) follows from the factor  $(1 - 2S_t^k)$  assigning unary potentials of different signs to pixels inside and outside the current segment  $S_t^k$ . This term can be represented as

$$\delta \sum_k \frac{(1 - 2S_t^k)' W S_t^k}{w' S_t^k} \equiv \delta \sum_k \|S_t^k - S^k\|_w$$

where  $\|S_t^k - S^k\|_w$  is a weighted Hamming distance between  $S^k$  and the current segment  $S_t^k$ . Thus, instead of bounds, functions (73) and (74) can be treated as Lagrangians for the constrained optimization of the unary or higher-order approximations of the corresponding objectives over *trust region* [81]

$$\|S_t^k - S^k\|_w \leq \tau.$$

In this case, parameter  $\delta$  is a Lagrange multiplier that can be adaptively changed from iteration to iteration [81], rather than exhaustively explored at each iteration. Note that it may still be useful to add a common monotone perturbation term as in [37]

$$\eta |S^k| \equiv \eta \mathbf{1}' S^k$$

that can be efficiently explored at each iteration. This corresponds to a combination of pseudo-bound and trust region techniques.

## 5 PARZEN ANALYSIS & BANDWIDTH SELECTION

This section discusses connections of  $k$ KM clustering to Parzen densities providing probabilistic interpretations for many equivalent pairwise clustering objectives discussed in our work. In particular, this section gives insights on practical selection of kernels or their bandwidth. We discuss extreme cases and analyze adaptive strategies. For simplicity, we mainly focus on Gaussian kernels, even though the analysis applies to other types of positive normalized kernels.

Note that standard Parzen density estimate for the distribution of data points within segment  $S^k$  can be expressed using normalized Gaussian kernels [84], [44]

$$\mathcal{P}_\sigma(I_p | S^k) = \frac{\sum_{q \in S^k} k(I_p, I_q)}{|S^k|}. \quad (75)$$

It is easy to see that  $k$ KM energy (22) is exactly the following high-order Parzen density energy

$$F(S) \stackrel{c}{=} - \sum_k \sum_{p \in S^k} \mathcal{P}_k(I_p | S^k). \quad (76)$$

This probabilistic interpretation of  $k$ KM gives an additional point of view for comparing it with pKM clustering with log-likelihood energy (14). Instead of parametric ML models  $k$ KM uses Parzen density estimates. Another difference is absence of the log in (76). Omitting the log reduces the weight of low probability points, that is, outliers. In contrast, log-likelihoods in (14) are highly sensitive to outliers. To address this problem, pKM methods often use heuristics like mixing the desired probability model  $\mathcal{P}$  with a uniform distribution, e.g.  $\tilde{\mathcal{P}}(\cdot | \theta) := \epsilon + (1 - \epsilon)\mathcal{P}(\cdot | \theta)$ .

### 5.1 Extreme bandwidth cases

Parzen energy (76) is also useful for analyzing two extreme cases of kernel bandwidth: large kernels approaching the data range and small kernels approaching the data resolution. This section analyses these two extreme cases.

**Large bandwidth and basic K-means:** Consider Gaussian kernels of large bandwidth  $\sigma$  approaching the data range. In this case Gaussian kernels  $k$  in (75) can be approximated (up to a scalar) by Taylor expansion  $1 - \frac{\|I_p - I_q\|^2}{2\sigma^2}$ . Then, Parzen density energy (76) becomes (up to a constant)

$$\sum_k \frac{\sum_{p,q \in S^k} \|I_p - I_q\|^2}{2\sigma^2 |S^k|}$$

which is proportional to the pairwise formulation for the basic K-means or *variance criteria* in Tab.1 with Euclidean metric  $\|\cdot\|$ . That is,  $k$ KM for large bandwidth Gaussian kernels reduces to the basic K-means in the original data space instead of the high-dimensional embedding space.

In particular, this proves that as the bandwidth gets too large  $k$ KM loses its ability to find non-linear separation of the clusters. This also emphasizes the well-known bias of basic K-means to equal size clusters [27], [85].

**Small bandwidth and Gini criterion:** Very different properties could be shown for the opposite extreme case of small bandwidth approaching data resolution. It is easy to approximate Parzen formulation of  $k$ KM energy (76) as

$$F(S) \stackrel{c}{\approx} - \sum_k |S^k| \cdot \langle \mathcal{P}_\sigma(S^k), d_s^k \rangle \quad (77)$$

where  $\mathcal{P}_\sigma(S^k)$  is kernel-based density (75) and  $d_s^k$  is a “true” continuous density for the sample of intensities  $\{I_p | p \in S^k\}$  in segment  $S^k$ . Approximation (77) follows directly from the same Monte-Carlo estimation argument in Appendix C with the only difference being  $f = -\mathcal{P}_\sigma(S^k)$  instead of  $-\log \mathcal{P}(\theta_S)$ .

If kernels have small bandwidth optimal for accurate Parzen density estimation<sup>15</sup> we get  $\mathcal{P}_\sigma(S^k) \approx d_s^k$  further reducing (77) to approximation

$$\stackrel{c}{\approx} - \sum_k |S^k| \cdot \langle d_s^k, d_s^k \rangle$$

that proves the following property.

**Property 1.** Assume small bandwidth Gaussian kernels optimal for accurate Parzen density estimation. Then kernel K-means energy (76) can be approximated by the standard Gini criterion for clustering [35]:

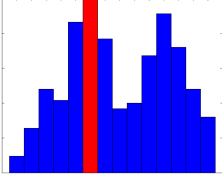
$$E_G(S) := \sum_k |S^k| \cdot G(S^k) \quad (78)$$

where  $G(S^k)$  is the Gini impurity for the data points in  $S^k$

$$G(S^k) := 1 - \langle d_s^k, d_s^k \rangle \equiv 1 - \int_x d_s^k(x)^2 dx. \quad (79)$$

Similarly to entropy, *Gini impurity*  $G(S^k)$  can be viewed as a measure of sparsity or “peakedness” for continuous or discrete distributions. Both Gini and entropy clustering criteria are widely used for decision trees [35], [36]. In this discrete context Breiman [35] analyzed theoretical

15. Bandwidth near inter-point distances avoids density oversmoothing.



properties of Gini criterion (78) for the case of histograms  $\mathcal{P}_h$  where  $G(S^k) = 1 - \sum_x \mathcal{P}_h(x|S^k)^2$ . He proved that for  $K = 2$  the minimum of the Gini criterion is achieved by sending all data points within the highest-probability bin to one cluster and the remaining

data points to the other cluster, see the color encoded illustration above. We extend Brieman's result to the continuous Gini criterion (78)-(79).

**Theorem 5 (Gini Bias,  $K = 2$ ).** *Let  $d_\Omega$  be a continuous probability density function over domain  $\Omega \subseteq \mathcal{R}^n$  defining conditional density  $d_\Omega^k(x) := d_\Omega(x|x \in S^k)$  for any non-empty subset  $S^k \subset \Omega$ . Then, continuous version of Gini clustering criterion (78) achieves its optimal value at the partitioning of  $\Omega$  into regions  $S^1$  and  $S^0 = \Omega \setminus S^1$  such that*

$$S^1 = \arg \max_x d_\Omega(x).$$

*Proof.* See Appendix E and Proposition 2.  $\square$

The bias to small dense clusters is practically noticeable for small bandwidth kernels, see Fig.14(d). Similar empirical bias to tight clusters was also observed in the context of average association (22) in [8]. As kernel gets wider the continuous Parzen density (75) no longer approximates the true distribution  $d_s$  and Gini criterion (78) is no longer valid as an approximation for  $k$ KM energy (76). In practice, *Gini bias* gradually disappears as bandwidth gets wider. This also agrees with the observations for wider kernel in average association [8]. As discussed earlier, in the opposite extreme case when bandwidth get very large (approaching data range)  $k$ KM converges to basic K-means or *variance criterion*, which has very different properties. Thus, kernel K-means properties strongly depend on the bandwidth.

The extreme cases for kernel K-means, *i.e.* Gini and variance criteria, are useful to know when selecting kernels. Variance criteria for clustering has bias to equal cardinality segments [27], [85]. In contrast, Gini criteria has bias to small dense clusters (Theorem 5). To avoid these biases kernel K-means should use kernels of width that is neither too small nor too large. Our experiments compare different strategies with fixed and adaptive-width kernels (Sec.5.2). Equivalence of kernel-K-means to many standard clustering criteria such as *average distortion*, *average association*, *normalized cuts*, *etc*(see Sec.1.2.2) also suggest kernel selection strategies based on practices in the prior literature.

## 5.2 Adaptive kernels via Nash embedding and KNN

As discussed in Sec.5.1, kernel width should neither be too small nor too large. We propose adaptive kernels designed to equalize the density in highly dense regions in the color space. The following equation interprets adaptive Gaussian kernels via Riemannian distances in the color space (left picture in Fig.13)

$$\begin{aligned} k_p(I_p, I_q) &= e^{-\frac{\|I_p - I_q\|^2}{2\sigma_p^2}} \\ &= e^{-\frac{(I_p - I_q)' \Sigma_p^{-1} (I_p - I_q)}{2}}. \end{aligned}$$

According to Nash embedding theorem [86], this Riemannian color space can be isometrically embedded into a Euclidean space, so that the last expression above is equal to

$$= e^{-\frac{\|I'_p - I'_q\|^2}{2}} = k(I'_p, I'_q)$$

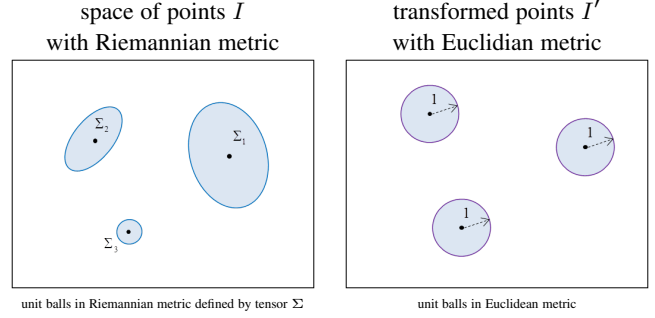


Fig. 13: *Nash embedding*: adaptive non-normalized Gaussian kernels define isometric transformation of the color space modifying density. Ellipsoids are mapped to balls.

where  $k$  is a fixed-width Gaussian kernel in the new transformed space (right picture in Fig.13). Thus, non-normalized Gaussian kernels of adaptive width  $\sigma_p$  (or covariance matrix  $\Sigma_p$ , in general) define some color space transformation, *Nash embedding*, that locally stretches or shrinks the space. After this transformation, clustering is done using a fixed (homogeneous) Gaussian kernel of constant width.

Figure 13 helps to illustrate how Nash embedding changes the color space density. The number of points in a unit (Euclidean) ball neighborhood in the transformed space is equal to the number of points in the corresponding unit (Riemannian) ball in the original space:

$$K = d' \cdot V_1 = d \cdot V_\sigma$$

where  $d$  and  $d'$  are local densities in the original and transformed spaces. Thus, kernel width  $\sigma_p$  can be selected adaptively based on any desired transformation of density  $d'(d)$  according to formula

$$\sigma_p \sim \sqrt[n]{\frac{d'(d_p)}{d_p}} \quad (80)$$

where  $d_p := d(I_p)$  is an observed local density for points in the color space. This local density can be evaluated using any common estimator, *e.g.* Parzen approach gives

$$d(I_p) \sim \sum_q \frac{1}{\Delta_q^n} \cdot e^{-\frac{\|I_p - I_q\|^2}{2\Delta_q^2}} \quad (81)$$

where  $\Delta_q$  could be adaptive or fixed  $\Delta_q = \text{const}$ , according to any standard technique for density estimation [84].

To address Breiman bias one can use density equalizing transforms  $d'(d) = \text{const}$  or  $d' = \frac{1}{\alpha} \log(1 + \alpha d)$ , which even up the highly dense parts of the color space. Formula (80) works for any target transform  $d'(d)$ . Once adaptive kernels  $\sigma_p$  are chosen, Nash theory also allows to obtain empirical scatter plots  $d'(d)_\Omega := \{(d'(I'_p), d(I_p)) | p \in \Omega\}$ , for example, to compare it with the selected “theoretical” plot  $d'(d)$ . Estimates  $d(I_p)$  are provided in (81) and the density estimate for Nash embedding are

$$d'(I'_p) \sim \sum_q e^{-\frac{\|I'_p - I'_q\|^2}{2}} = \sum_q e^{-\frac{\|I_p - I_q\|^2}{2\sigma_q^2}}. \quad (82)$$

Note the difference between empirical density estimates for  $d'$  in (82) and  $d$  in (81): the former uses the sum of *non-normalized* kernels of selected adaptive width  $\sigma_q$  in (80) and the latter is the sum of *normalized* kernels of width  $\Delta_q$  based on chosen density estimator. While parameter  $\sigma_q$  directly controls the density



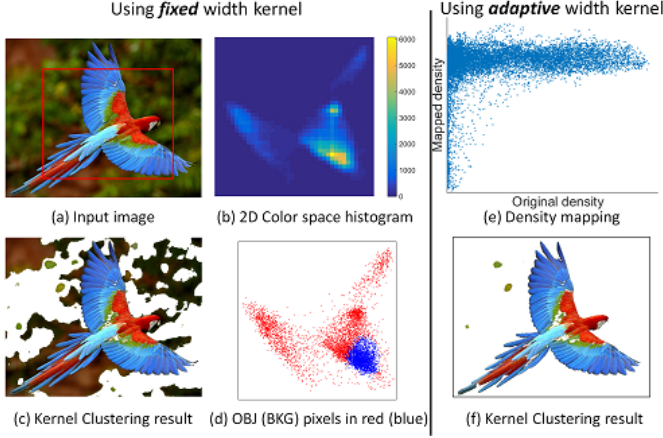


Fig. 14: (a)-(d): Breiman bias for fixed (small) kernel. (e) Empirical density transform for adaptive kernels (80) with  $d'(d) = \text{const}$ . Color space density equalization counters Breiman bias. (f) Segmentation for adaptive kernels.

transformation,  $\Delta$  plays a fairly minor role concerning the quality of estimating density  $d$ .

Figure 14(e) illustrates the empirical density mapping  $d'(d)_\Omega$  induced by adaptive kernels (80) for  $d'(d) = \text{const}$ . Notice a density-equalization effect within high density areas in the color space addressing the Breiman bias.

The const density mapping can be approximated using  $KNN$  graph. To be specific, the symmetric  $KNN$  kernel in this paper is defined as follows:

$$k_{pq} = k(f_p, f_q) = \begin{aligned} &[f_p \in KNN(f_q)] \\ &+ [f_q \in KNN(f_p)] \end{aligned} \quad (83)$$

where  $KNN(f_p)$  is a set of  $K$  nearest neighbors of  $f_p$ . The affinity between  $f_p$  and  $f_q$  achieves maximum value of 2 if they are mutually each other's  $KNN$ s.

## 6 EXPERIMENTS

This section is divided into two parts. The first part (Sec.6.1) shows the benefits of extra MRF regularization for kernel & spectral clustering, e.g. normalized cut. We consider pairwise Potts, label cost and robust bin consistency term, as discussed in Sec.1.1. We compare to spectral clustering [8], [66] and kernel K-means [40], which can be seen as degenerated versions for spectral and kernel cuts (respectively) without MRF terms. We show that MRF helps normalized cut in segmentation and image clustering. In the second part (Sec.6.2) we replace the log-likelihoods in model-fitting methods, e.g. GrabCut [26], by pairwise clustering term, e.g. AA and NC. This is particularly advantageous for high dimension features (location, depth, motion).

**Implementation details:** For segmentation, our kernel cut uses  $KNN$  kernel (83) for pixel features  $I_p$ , which can be concatenation of LAB (color), XY (location) and M (motion or optical flow) [87]. We choose 400 neighbors and randomly sample 50 neighbors for each pixel. Sampling does not degrade our segmentation but expedites bound evaluation. We also experiment with popular  $mPb$  contour based affinities [67] for segmentation. The window radius is set to 5 pixels.

For contrast-sensitive regularization, we use standard penalty  $w_{pq} = \frac{1}{d_{pq}} e^{-0.5\|I_p - I_q\|_2^2/\beta}$  for (2), where  $\beta$  is the average of  $\|I_p -$

$I_q\|_2^2$  over a 8-connected neighborhood and  $d_{pq}$  is the distance between pixels  $p$  and  $q$  in the image plane. We set  $w_{pq} = \frac{1}{d_{pq}}$  for length regularization.

For GrabCut, we used histogram-based probability model, as is common in the literature [82], [88]. We tried various bin size for spatial and depth channels. We extract GIST [89] features for image clustering and use Gaussian kernel to build a dense affinities matrix.

With fixed width Gaussian kernel used in Fig. 14, naive implementation of kernel bound evaluation in (55) is of  $O(|\Omega|^2)$  time complexity. The bottleneck is the evaluation of  $\mathcal{K}X_t$  and  $X_t' \mathcal{K}X_t$  in derivative  $\nabla \hat{e}(X_t)$  (52). In this case, we resort to fast approximate dense filtering method in [90], which takes  $O(|\Omega|)$  time. Also notice that the time complexity of the approach in [90] grows exponentially with data dimension  $N$ . A better approach for high-dimensional dense filtering is proposed in [91], which is of time  $O(|\Omega| \times N)$ . We stick to [90] for low-dimensional color space in experiments in Fig. 14.

### 6.1 MRF helps Kernel & Spectral Clustering

Here we add MRF regulation terms to typical normalized cut applications, such as unsupervised multi-label segmentation [67] and image clustering [92]. Our kernel and spectral cuts are used to optimize the joint energy of normalized cut and MRF (1).

#### 6.1.1 Normalized Cut with Potts Regularization

Spectral clustering [8] typically solves a (generalized) eigen problem, followed by simple clustering method such as K-means on the eigenvectors. However, it is known that such paradigm results in undesirable segmentation in large uniform regions [67], [66], see examples in Fig. 15. Obviously such edge mis-alignment can be penalized by contrast-sensitive Potts term. Our spectral cut and kernel cut get better segmentation boundaries. As is in [40] we use spectral initialization.

Tab. 5 gives quantitative results on BSDS500 dataset. Number of segments in ground truth is provided to each method. It shows that kernel and spectral cut give better covering, PRI (probabilistic rand index) and VOI (variation of information) than spectral clustering. Fig. 15 gives sample results. Kernel K-means [40] gives results similar to spectral clustering and hence are not shown.

#### 6.1.2 Normalized Cuts with Label Cost [12]

Unlike spectral clustering, our kernel and spectral cuts do not need the number of segments beforehand. We use kernel cut to optimize a combination of the normalized cut, Potts model and label costs terms. The label cost (4) penalizes each label by constant  $h_k$ . The energy is minimized by  $\alpha$ -expansion and  $\alpha\beta$ -swap moves in Sec.2.3. We sample initial models from patches, as in [12]. Results with different label cost are shown in Fig. 16. Due to sparsity prior for normalized cut, our kernel and spectral cuts automatically prune *weak* models and determine the number of segments, yet yield regularized segmentation. We use  $KNN$  affinity for normalized cut and  $mPb$  [67] based Potts regularization.

#### 6.1.3 Normalized Cut with High Order Consistency Term [11], [13], [14]

It is common that images come with multiple tags, such as those in Flickr platform or the LabelMe dataset [89]. We study how to utilize tag-based group prior for image clustering [92].



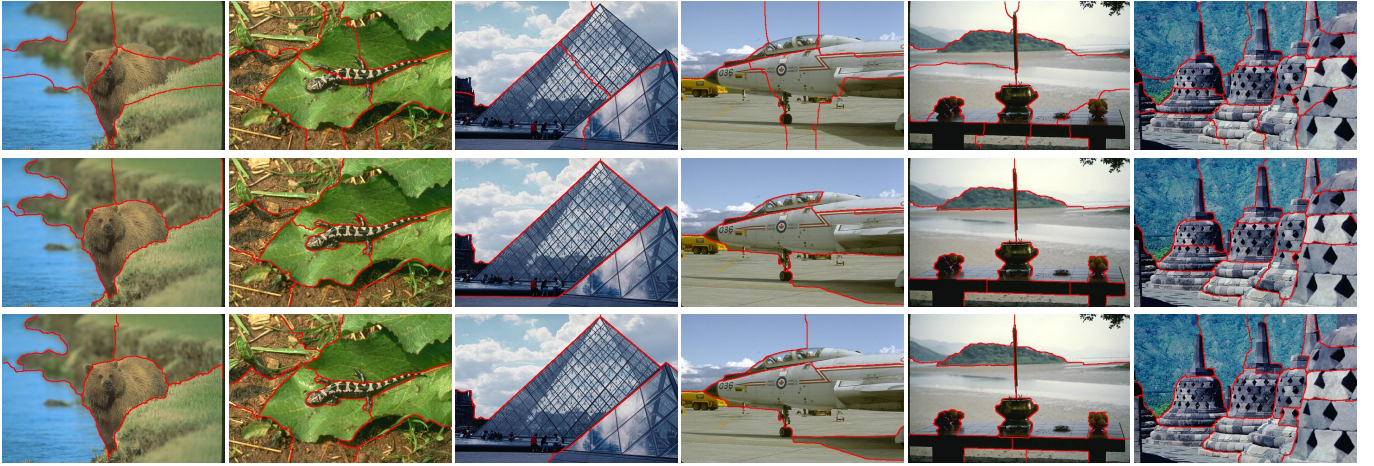


Fig. 15: Sample results on BSDS500. Top row: spectral clustering. Middle & Bottom rows: our Kernel & Spectral Cuts.

method	Covering	PRI	VOI
Spectral Clustering	0.34	0.76	2.76
Our Kernel Cut	0.41	<b>0.78</b>	2.44
Our Spectral Cut	<b>0.42</b>	<b>0.78</b>	<b>2.34</b>

TABLE 5: Results of spectral clustering (K-means on eigenvectors) and our Kernel Cut & Spectral Cut on BSDS500 dataset. For this experiment mPb-based kernel is used [67].

We experiment on the LabelMe dataset [89] which contains 2,600 images of 8 scene categories (coast, mountain, forest, open country, street, inside city, tall buildings and highways). We use the same GIST feature, affinity matrix and group prior as used in [92]. We found the group prior to be noisy. The dominant category in each group occupies only 60%-90% of the group. The high-order consistency term is defined on each group. For each group, we introduce an energy term that is akin to the *robust*  $P^n$ -Potts [11], which can be exactly minimized within a single  $\alpha\beta$ -swap or  $\alpha$ -expansion move. Notice that here we have to use robust consistency potential instead of rigid ones.

Our kernel cut minimizes NC plus the *robust*  $P^n$ -Potts term. Spectral cut minimizes energy of (67). Normalized mutual information (NMI) is used as the measure of clustering quality. Perfect clustering with respect to ground truth has NMI value of 1.

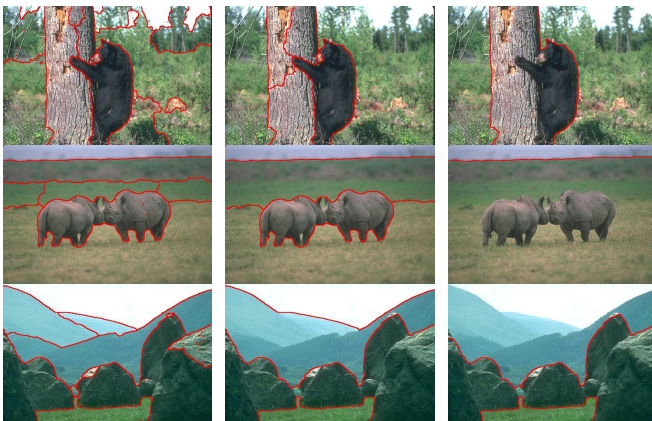


Fig. 16: From left to right label cost  $h_k(4)$  is increased.

Spectral clustering and kernel K-means [40] give NMI value of 0.542 and 0.572 respectively. Our kernel cut and spectral cut significantly boost the NMI to 0.683 and 0.681. Fig. 17 shows the results with respect to different amount of image tags used. The left most points correspond to the case when no group prior is given. We optimize over the weight of high order consistency term, see Fig. 17. Note that it's not the case the larger the weight the better since the grouping prior is noisy.

## 6.2 Kernel & Spectral Clustering helps MRF

In typical MRF applications we replace the log-likelihood terms by average association or normalized cut. We evaluated our Kernel Cut (fixed width kernel or  $KNN$ ) in the context of interactive segmentation, and compared with the commonly used GrabCut algorithm [26]. In Sec. 6.2.1, we show that our kernel cut is less sensitive to choice of regularization weight  $\gamma$ . We further report results on the GrabCut dataset of 50 images and the Berkeley dataset in Sec. 6.2.2. We experiment with both (i) contrast-sensitive edge regularization, (ii) length regularization and (iii) color clustering (i.e., no regularization) so as to assess to what extent the algorithms benefit from regularization.

From Sec. 6.2.3 to Sec. 6.2.6, we also report segmentation results of our kernel cut with high-dimensional features  $I_p$ , including location, texture, depth, and motion respectively.

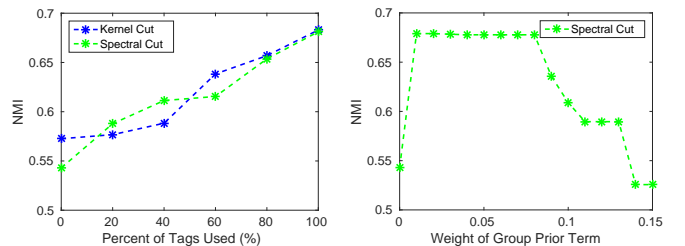


Fig. 17: Incorporating group prior achieves better NMI for image clustering. Here we use tags-based group prior. Our method achieved better NMI when more images are tagged. The right plot shows how the weight of bin consistency term affects our method.

### 6.2.1 Robustness to regularization weight

We first run all algorithms without smoothness. Then, we experiment with several values of  $\gamma$  for the contrast-sensitive edge term. In the experiments of Fig. 18 (a) and (b), we used the yellow boxes as initialization. For a clear interpretation of the results, we did not use any additional hard constraint. Without smoothness, our Kernel Cut yielded much better results than model fitting. Regularization significantly benefited the latter, as the decreasing blue curve in (a) indicates. For instance, in the case of the zebra image, model fitting yielded a plausible segmentation when assisted with a strong regularization. However, in the presence of noisy edges and clutter, as is the case of the chair image in (b), regularization did not help as much. Note that for small regularization weights  $\gamma$  our method is substantially better than model fitting. Also, the performance of our method is less dependent on regularization weight and does not require fine tuning of  $\gamma$ .

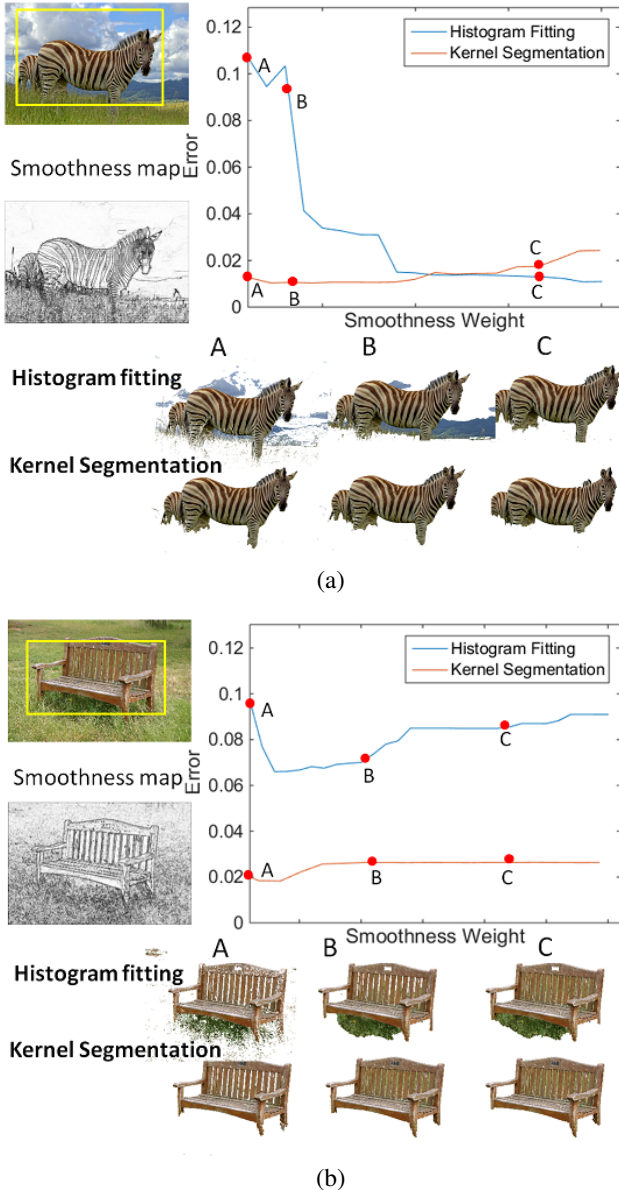


Fig. 18: Illustration of robustness to smoothness weight.

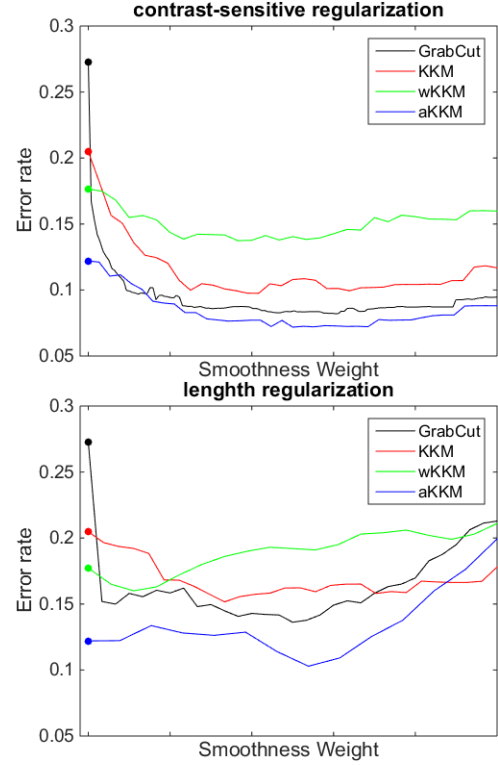


Fig. 19: Average error vs. regularization weights for different algorithms on the GrabCut dataset.

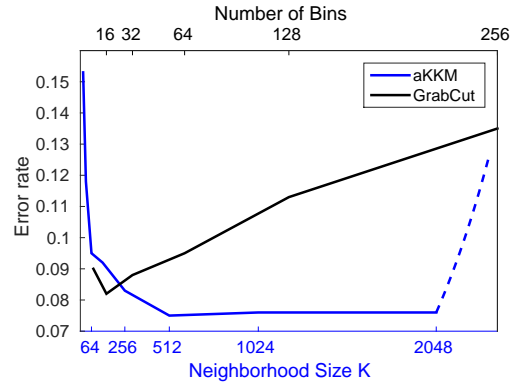


Fig. 20: Our method aKKM is robust to choice of  $K$  while GrabCut is sensitive to bin size for histograms.

### 6.2.2 Segmentation on GrabCut & Berkeley datasets.

First, we report results on the GrabCut database (50 images) using the bounding boxes provided in [93]. For each image the error is the percentage of mis-labeled pixels. We compute the average error over the dataset.

We test different smoothness weights and plot the error curves<sup>16</sup> in Fig. 19. Table 6 reports the best error for each method. For contrast-sensitive regularization GrabCut gets good results (8.2%). However, without edges (Euclidean or no regularization) GrabCut gives much higher errors (13.6% and 27.2%). In contrast, aKKM (Kernel Cut with adaptive kernel) gets only 12.2% doing a better job in color clustering without any help from the

<sup>16</sup> The smoothness weights for different energies are not directly comparable; Fig. 19 shows all the curves for better visualization.



boundary smoothness	color clustering term			
	GrabCut	KKM	wKKM	aKKM
none	27.2	20.4	17.6	<b>12.2</b>
Euclidean length	13.6	15.1	16.0	<b>10.2</b>
contrast-sensitive	8.2	9.7	13.8	<b>7.1</b>

TABLE 6: Box-based interactive segmentation (Fig.21). Error rates (%) are averaged over 50 images in GrabCut dataset.

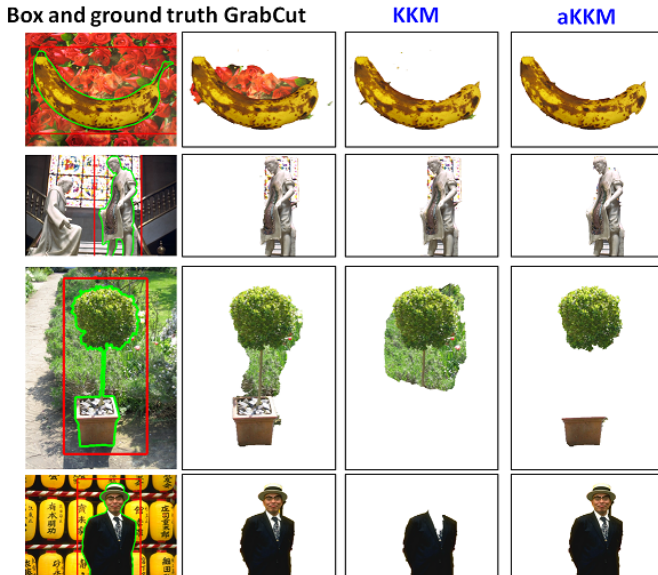


Fig. 21: Sample results for GrabCut and our kernel methods with fixed & adaptive widths (KKM, aKKM), see Tab.6.

edges. In case of contrast-sensitive regularization, our method outperformed GrabCut (7.1% vs. 8.2%) but both methods benefit from strong edges in the GrabCut dataset. Fig. 20 shows that our Kernel Cut is also robust to the hyper-parameter, i.e.  $K$  for nearest neighbours, unlike GrabCut.

Figure 21 gives some sample results. The top row shows a failure case for GrabCut where the solution aligns with strong edges. The second row show a challenging image where our adaptive kernel method (aKKM) works well. The third and fourth rows shows failure cases for fixed-width kernel (KKM) due to Brieman’s bias where image segments of uniform color are separated; see green bush and black suit. Our adaptive approach (aKKM) addresses this bias.

We also tested seeds-based segmentation on a different database [94] with ground truth, see Tab.7 and Fig.22.

### 6.2.3 Segmentation of similar appearance objects

Even though objects may have similar appearances or look similar to the background (e.g. the top row in Fig.24), we assume that the objects of interest are compact and have different locations. This assumption motivates using XY coordinates of pixels as extra feature for distinguishing similar or camouflaged objects. XY feature has also been used in [95] to build space-variant color distribution. However, such distribution used in MRF-MAP inference [95] would still overfit the data [41]. Let  $I_p \in \mathcal{R}^5$  be the augmented color-location feature  $I_p = [l_p, a_p, b_p, \beta x_p, \beta y_p]$  at pixel  $p$  where  $[l_p, a_p, b_p]$  is its color,  $[x_p, y_p]$  are its image coordinates, and  $\beta$  is a scaling parameter. Note that the edge-based Potts model [4] also uses the XY information. Location features in

boundary smoothness	color clustering term		
	BJ	GrabCut	aKKM
none	12.4	12.4	<b>7.6</b>
contrast-sensitive	3.2	3.7	<b>2.8</b>

TABLE 7: Seeds-based interactive segmentation (Fig.22). Error rates (%) are averaged over 82 images from Berkeley database. Methods get the same seeds entered by four users. We removed 18 images with multiple nearly-identical objects (see Fig.24) from 100 image subset in [94]. (GrabCut and aKKM give 3.8 and 3.0 errors on the whole database.)

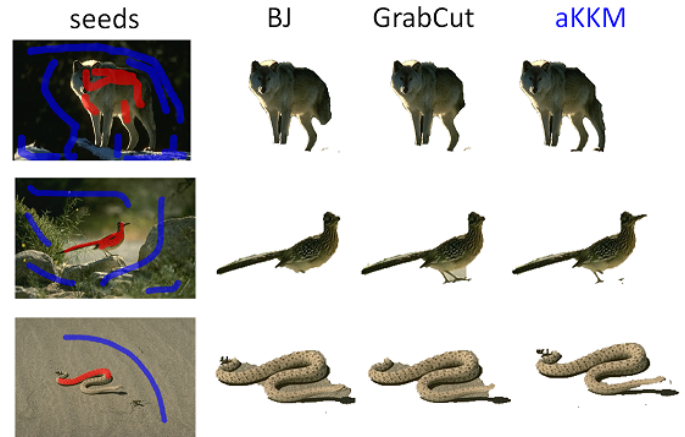


Fig. 22: Sample results for BJ [4], GrabCut [26], and our adaptive kernel segmentation (aKKM), see Tab.7.

the clustering and regularization terms have complementary effect: the former solves appearance camouflage while the latter gets edge alignment.

We test the effect of adding XY into feature space for GrabCut and Kernel Cut. We try various  $\beta$  for Kernel Cut. Fig.23 shows the effect of different  $\beta$  on KNNs of a pixel.

We report quantitative results on 18 images with similar objects and camouflage from the Berkeley database [96]. Seeds are used here. Fig. 25 shows average errors for multi-object dataset. We vary the spatial bin size for GrabCut and  $\beta$  for Kernel Cut. The connection range is the average geometric distance between a pixel and its  $k^{th}$  nearest neighbor. **The right-most point of the curves corresponds to the absence of XY features.** GrabCut does not benefit from XY features. Kernel Cut achieves the best error rate of 2.9% with connection range of 50 pixels.

We report quantitative results on a multi-objects and camouflage database we collected. The 18 selected images are from the Berkeley segmentation database [96] and we generate strokes for selecting one object among multiple similar objects, see example images and segmentations in Fig. 24. Fig. 25 shows the average error rates for GrabCut and Kernel Cut. Fig. 26 gives multi-label segmentation of similar objects in one image with seeds using our algorithm. We optimize kernel bound with move-making for NC plus smoothness term, as discussed in Sec. 2.2. Fig. 26 (c) shows energy convergence.

### 6.2.4 Texture segmentation

The goal of this experiment is to demonstrate scalability of our method to highly dimensional data. First, desaturated images from GrabCut database [26] are convolved with 48 filters from [97]. This yields a 48-dimensional descriptor for each pixel. Secondly,



Fig. 23: Visualization of a pixel's K-Nearest-Neighbours for RGB feature (left) or RGBXY feature (right).

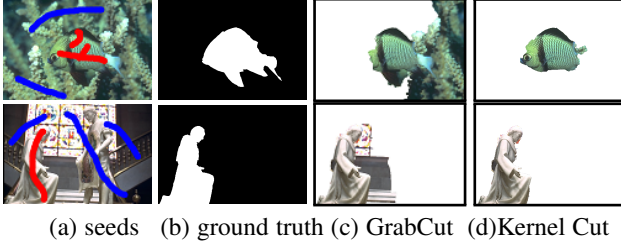


Fig. 24: Sample results using RGBXY+XY.

these descriptors are clustered into 32 textons by K-means. Thirdly, for each pixel we build a 32-dimensional normalized histogram of textons in  $5 \times 5$  vicinity of the pixel. Then the gray-scale intensity<sup>17</sup> of a pixel is augmented by the corresponding texton histogram scaled by a factor  $w$ . Finally, resulting 33-dimensional feature vectors are used for segmentation. We show the result of Kernel Cut with respect to  $w$  in Fig. 27. We compare our results with GrabCut with various bin sizes for texture features.

### 6.2.5 Segmentation with depth features

Over a last few years depth sensors have been widely and successfully used for various computer vision problems such as 3D modeling [99], [100], semantic segmentation [101], [102], [98], [103], motion flow estimation [104], *etc.* This section describes a few experiments, that use an additional depth channel for interactive segmentation.

In order to evaluate the methods (GrabCut and Kernel Cut) with respect to performance on RGBD data an appropriate database is required. We manually selected 64 images from NYUv2 database [98] of densely labeled indoor RGBD scenes. The database was initially used for semantic segmentation. For the selected images we provide bounding boxes and ground truth for interactive binary segmentation. In contrast to GrabCut database, the prepared dataset consist of low-quality images: there are camera motion artifacts, underexposed and overexposed regions, out of focus images. These artifacts make the color-based segmentation problem harder.

Both tested methods require defining several parameters. All of them have smoothness weight  $\gamma$  for MRF regularization. In addition, GrabCut is parameterized by the size of histogram bins, while Kernel Cut requires to set number  $K$  of nearest neighbors. We used the same  $K$  as in the previous sections for Kernel Cut. We optimize the results of GrabCut over the size of color bins and  $\gamma$ . We also optimize the results of Kernel Cut over  $\gamma$ .

One of the objectives of the experiment is to study the relation of the performance of the methods and the “importance” of D-

17. We found that for the GrabCut database adding texture features to RGB does not improve the results.

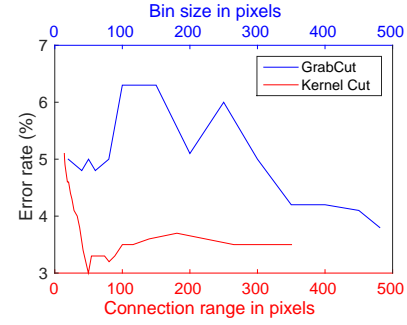


Fig. 25: Error on Multi-objects dataset. We vary spatial bin-size for GrabCut and weight  $\beta$  in  $[l, a, b, \beta X, \beta Y]$  for Kernel Cut.

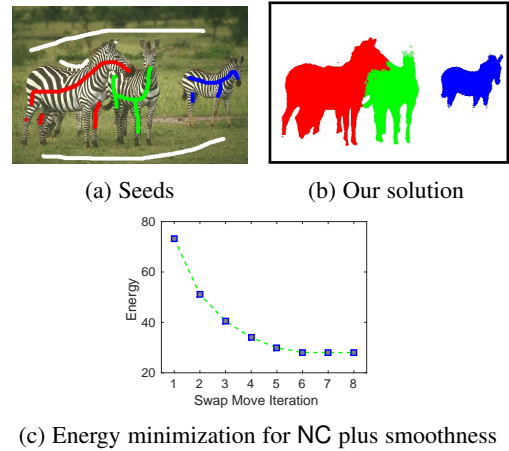


Fig. 26: Multi-label segmentation for similar objects.

channel. In case of GrabCut the measure of D-channel importance is the size of the bins. There are two extremes. First, if all pixels fall into the same bin w.r.t. D-channel the method will not be able to differentiate pixels with different depths. That corresponds to the lowest importance. On the other end, all pixels with different depth would be treated independently. That corresponds to highest importance of D-channel. In case of Kernel Cut the importance is defined by scaling factor  $\beta$ , which is used in the definition of the feature vector of a pixel:  $[R, G, B, \beta D]$ .

The average error statistics for GrabCut and Kernel Cut with respect to importance of the depth dimension are shown in Fig. 29. The examples of segmentation are shown in Fig. 28. The optimal value of  $\beta$  suggests that for that particular database D-channel contains strictly more information than RGB channels. On the other hand, GrabCut failed to improve given the additional channel.

### 6.2.6 Motion segmentation

This subsection shows two applications using our proposed framework for *motion segmentation* in binary and multi-label settings. In addition to location and depth features used above, we show segmentation results for motion. Figs. 30, 31 and 32 compare motion segmentations using different feature spaces: RGB features, XY feature, M feature (optical flow) and their combinations (RGBM or RGBXY or RGBXYM). Here we use Kernel Cut for the normalized cut energy combined with MRF regularization.



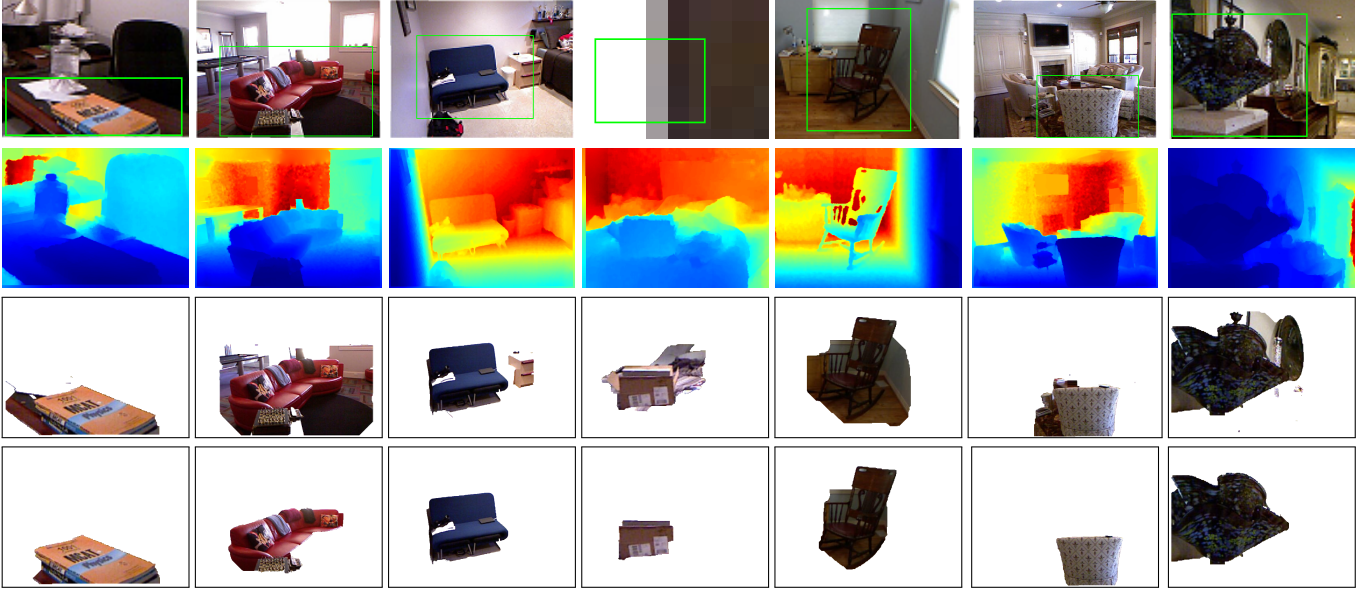


Fig. 28: RGBD+XY examples. The first two rows show original images with bounding box and color-coded depth channel. The third row shows the results of Grabcut, the fourth row shows the results of Kernel Cut. Parameters of the methods were independently selected to minimize average error rate over the database. The parameters of the algorithms were selected to minimize the average error over the dataset.

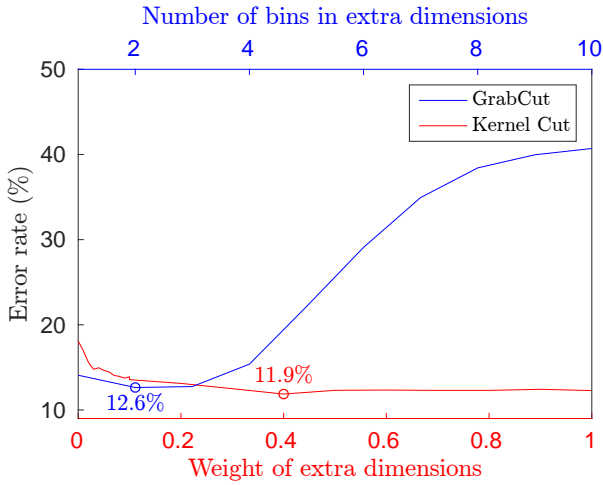


Fig. 27: The average errors of GrabCut and Kernel Cut methods for texture segmentation over 50 desaturated images from GrabCut database [26]. We optimize the result of GrabCut with respect to smoothness weight and bin sizes in the intensity dimension. We optimize the result of Kernel Cut with respect to smoothness weight.

**Motion segmentation example 1:** For videos in FBMS-59 dataset [105], our algorithm runs on individual frames, instead of 3D volume. Segmentation of previous frame is taken as initialization for the next frame and strokes are provided *only* for the first frame. We used recent optical flow algorithm in [87] to generate M features. Results for selected frames are in Figs. 30 and 31. Instead of tracks from all frames in [107], our segmentation of each frame uses only motion estimation between two consecutive frames. Our approach jointly optimizes feature space clustering and XY regularization (normalized cut + Potts), while [107] first

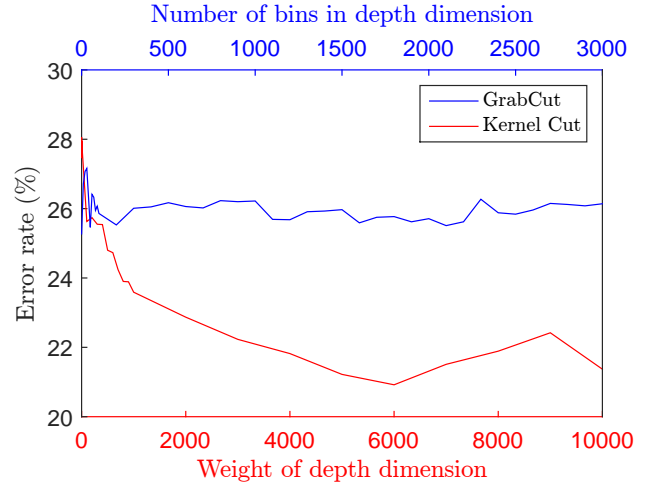


Fig. 29: The average errors of GrabCut and Kernel Cut methods over 64 images selected from NYUv2 database [98].

clusters semi-dense tracks using normalized cuts [105] and then obtains dense image segmentation using regularization.

**Motion segmentation example 2:** We also experiment with Kitti dataset [106]. Figure 32 shows the multi-label segmentation using either color information RGB+XY (the first row) or motion MXY+XY (the second row). We use the provided ground-truth motion field as a source of M channel. Note that the motion field is known only for approximately 20% of pixels. To build an affinity graph, we construct a KNN graph from pixels that have motion information. The regularization over 8-neighborhood on the pixel grid naturally interpolates the segmentation labels during the optimization procedure.



Fig. 30: Motion segmentation using our framework for the sequence *horses01* in FBMS-59 dataset [105]. Motion feature alone ( $M+XY$  in (c)) is not sufficient to obtain fine segmentation. Our framework successfully utilize motion feature (optical flow) to separate the horse from the barn, which have similar appearances.

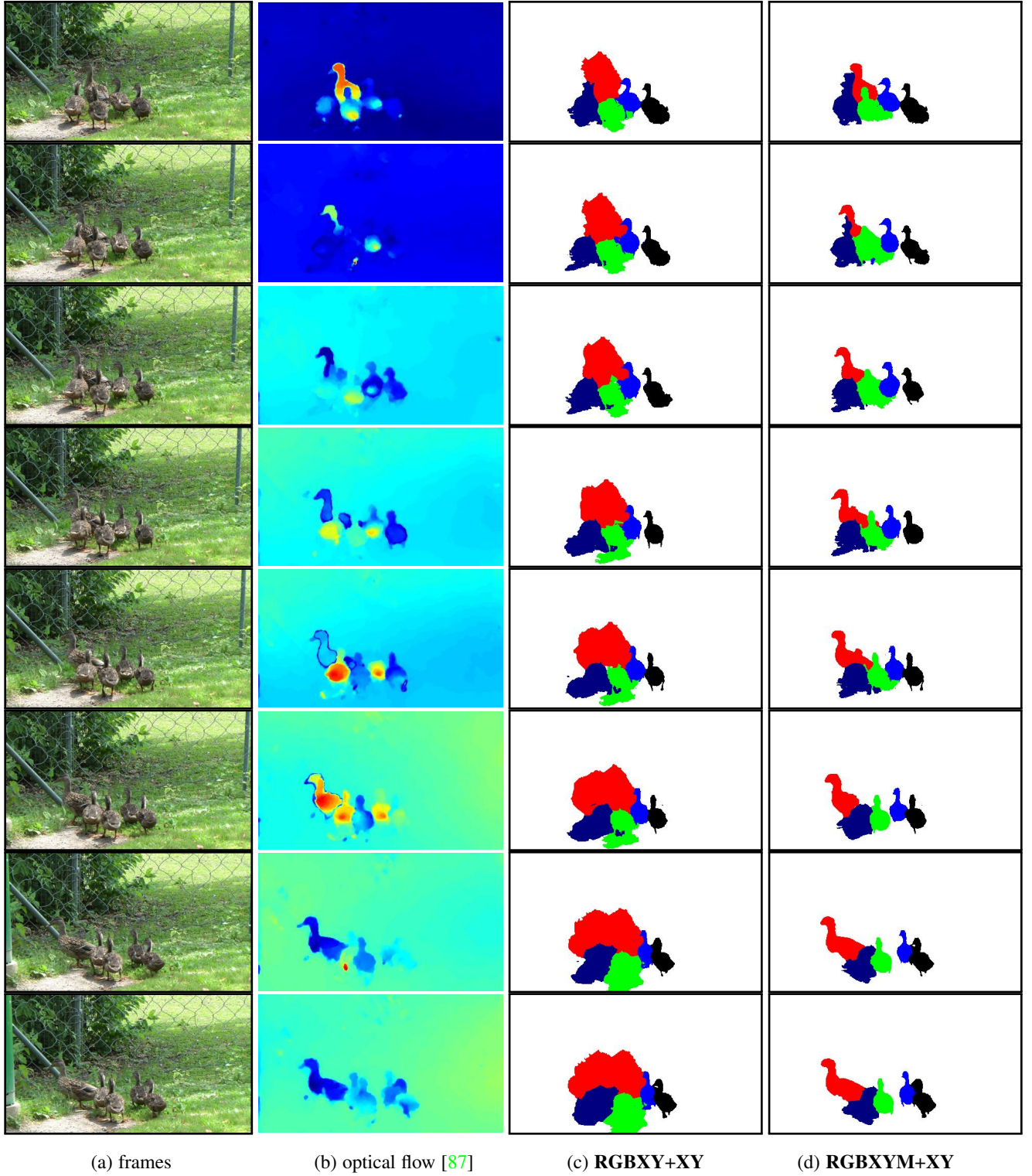


Fig. 31: Multi-label motion segmentation using our framework for the sequence *ducks01* in FBMS-59 dataset [105]. This video is challenging since the ducks here have similar appearances and even spatially overlap with each other. However, different ducks come with different motions, which helps our framework to better separate individual ducks.



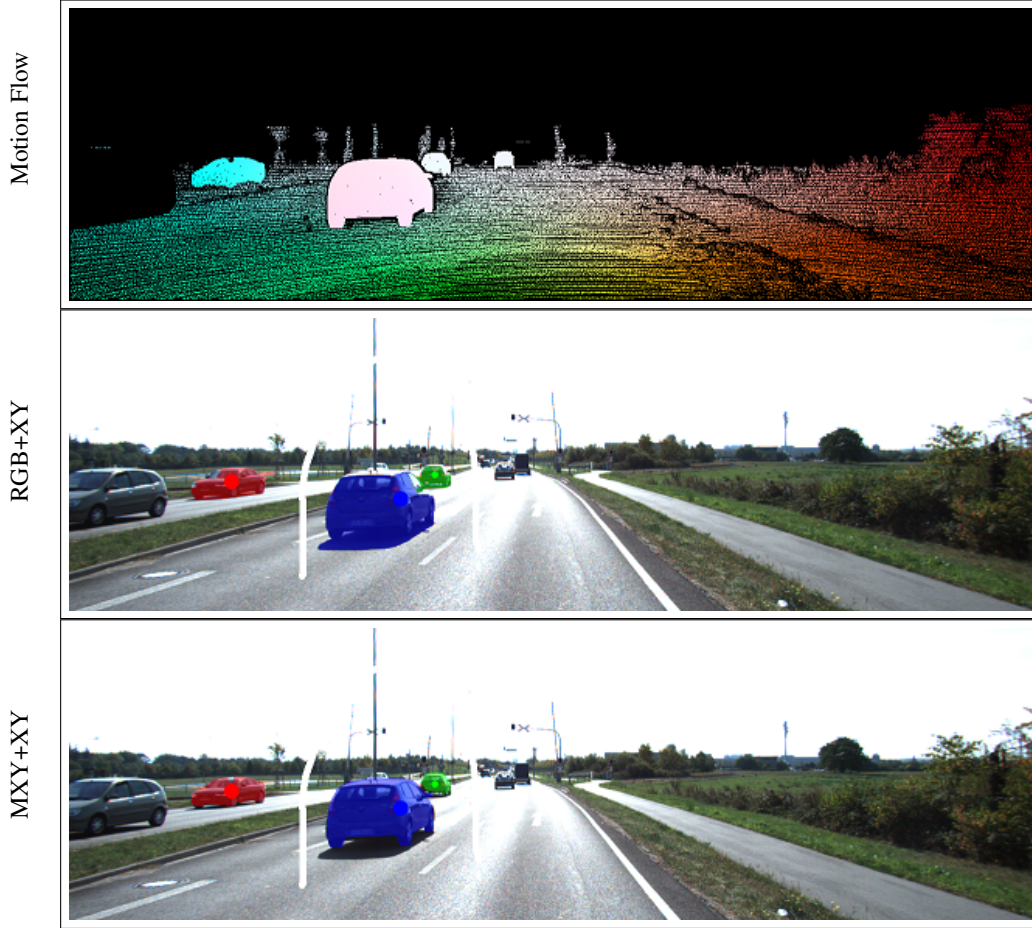


Fig. 32: Motion segmentation for image 000079\_10 from *KITTI* [106] dataset. The first row shows the motion flow. Black color codes the pixels that do not have motion information. The second row shows color-based segmentation. The third row shows motion based segmentation with location features. We also tried M+XY segmentation, but it does not work as well as MXY+XY above. The results for RGBMXY+XY were not significantly different from MXY+XY.

## APPENDIX A (WEIGHTED KM AND AA)

This Appendix reviews weighted kernel K-means (*wkKM*) in detail. In particular, it describes generalizations of KM procedures (23) and (24) to the weighted case and shows that they also correspond to linear bound optimization by extending Theorem 1 in Sec. 2.1. We provide an alternative derivation for the kernel bound for NC. The Appendix also discusses equivalence of weighted AA with arbitrary affinity to *wkKM* with p.s.d. kernel and explains the corresponding *diagonal shift*.

**Weighted kernel K-means (*wkKM*):** As discussed in Section 1.2.2, weighted K-means corresponds to objective (36)

$$F^w(S) = \sum_k \sum_{p \in S^k} w_p \|\phi_p - \mu_{S^k}^w\|^2 \quad (\text{A-1})$$

$$\stackrel{c}{=} - \sum_k \frac{S^{k'} W \mathcal{K} W S^k}{S^{k'} w} \quad (\text{A-2})$$

where  $\|\cdot\|$  is the Euclidean norm,  $w := \{w_p | p \in \Omega\}$  are predefined weights,  $\phi_p \equiv \phi(I_p)$  is an *embedding* of data points in some high-dimensional space, and  $\mu_{S^k}^w$  is a weighted cluster mean (33). Consistently with Sec. 1.2.2 we use diagonal matrix  $W = \text{diag}(w)$  and embedding matrix  $\phi := [\phi_p]$  implying identities (34) and matrix formulation (A-2) with p.s.d. kernel

$$\mathcal{K} = \phi' \phi$$

of dot products  $\mathcal{K}_{pq} = \phi_p' \phi_q$ . The constant connecting equivalent objectives (A-1) and (A-2) is  $\sum_{p \in \Omega} w_p \|\phi_p\|^2$ .

In the context of weighted energy (A-1) the basic KM algorithm [28] is the *block-coordinate descent* for *mixed* objective (32)

$$\begin{aligned} F^w(S, m) &:= \sum_k \sum_{p \in S^k} w_p \|\phi_p - m_k\|^2 \\ &\stackrel{c}{=} \sum_k \left( w \|m_k\|^2 - 2W \phi' m_k \right)' S^k \end{aligned} \quad (\text{A-3})$$

where the second linear algebraic formulation<sup>18</sup> generalizes (49) and highlights modularity (linearity) with respect to  $S$ . Variables  $m_k$  can be seen as “relaxed” segment means  $\mu_{S^k}^w$  in (A-1). Yet, energies (A-3) and (A-1) are equivalent since their global minimum is achieved at the same optimal segmentation  $S$ . Indeed,

$$\begin{aligned} \mu_{S^k}^w &= \arg \min_{m_k} \sum_{p \in S^k} w_p \|\phi_p - m_k\|^2 \\ \Rightarrow F^w(S) &= \min_m F^w(S, m). \end{aligned} \quad (\text{A-4})$$

**Weighted KM and bound optimization:** The weighted case of procedure (23) replaces  $\mu_{S^k}$  (17) by weighted mean  $\mu_{S^k}^w$  (33)

$$\left( \begin{array}{l} \text{weighted KM} \\ \text{procedure} \end{array} \right) \quad S_p \leftarrow \arg \min_k \|\phi_p - \mu_{S^k}^w\|. \quad (\text{A-5})$$

18. It is obtained by opening the square of the norm and applying algebraic identities (34). Formulation (A-3) omits the same constant as (A-2).



Assuming  $\phi_p \in \mathcal{R}^m$  each iteration's complexity  $\mathcal{O}(|\Omega|Km)$  is linear with respect to the number of data points  $|\Omega|$ .

Implicit  $k$ KM procedure (24) generalizes to the weighted case as follows. Similarly to Sec.8.2.2 in [50] and our derivation of (24) in Sec.1.2.2, the square of the objective in (A-5) and (33) give

$$\|\phi_p\|^2 - 2\phi_p' \mu_{S_t^k} + \|\mu_{S_t^k}\|^2 = -2 \frac{\phi_p' \phi W S_t^k}{S_t^{k'w}} + \frac{S_t^{k'w} W \phi' \phi W S_t^k}{(S_t^{k'w})^2}.$$

Since the crossed term is a constant at  $p$ , the right hand side gives an equivalent objective for computing  $S_p$  in (A-5). Using  $\mathcal{K} = \phi' \phi$  and indicator vector  $\mathbf{1}_p$  for element  $p$  we get generalization of (24)

$$\left( \begin{array}{c} \text{weighted} \\ k\text{KM} \\ \text{procedure} \end{array} \right) S_p \leftarrow \arg \min_k \frac{S_t^{k'w} W \mathcal{K} W S_t^k}{(S_t^{k'w})^2} - 2 \frac{\mathbf{1}_p' W \mathcal{K} W S_t^k}{S_t^{k'w}}. \quad (\text{A-6})$$

In contrast to procedure (A-5), this approach has iterations of quadratic complexity  $\mathcal{O}(|\Omega|^2)$ . However, it avoids the explicit use of high-dimensional embeddings  $\phi_p$  replacing them by the kernel matrix  $\mathcal{K}$  in all computations, a.k.a. the *kernel trick*.

Generalizing Theorem 1 in Sec. 2.1 we can interpret weighted KM procedures (A-5, A-6) as linear bound optimization.

**Theorem 6 (bound for (35, A-1)).** *Weighted KM procedures (A-5) or (A-6) can be seen as bound optimization methods for weighted K-means objective  $F^w(S)$  (35) or (A-1) using auxiliary function*

$$a_t(S) := F^w(S, \mu_t^w) \quad (\text{A-7})$$

at any current segmentation  $S_t = \{S_t^k\}$  with means  $\mu_t^w = \{\mu_{S_t^k}^w\}$ .

*Proof.* Indeed, (A-4) implies  $a_t(S) \geq F^w(S)$ . Since  $a_t(S_t) = F^w(S_t)$  then  $a_t(S)$  is a proper bound for  $F^w(S)$ . Re-segmentation step (A-5) produces optimal segments  $S_{t+1}$  minimizing the bound  $a_t(S)$ . Re-centering step minimizing  $F^w(S_{t+1}, m)$  for fixed segments produces means  $\mu_{t+1}^w$  defining the bound  $a_{t+1}(S)$  for the next iteration.  $\square$

Since algebraic formulations (A-3) and (A-2) omit the same constant we also get the following Corollary.

**Corollary 1 (bound for (36, A-2)).** *Weighted KM procedures (A-5) or (A-6) can be seen as bound optimization methods for  $wk$ KM objective  $F^w(S)$  in (A-2) using auxiliary function*

$$a_t(S) := \sum_k \left( w \|\mu_{S_t^k}^w\|^2 - 2W \phi' \mu_{S_t^k}^w \right)' S^k \quad (\text{A-8})$$

$$\equiv \sum_k \left( w \frac{S_t^{k'w} W \mathcal{K} W S_t^k}{(w' S_t^k)^2} - W \mathcal{K} W S_t^k \frac{2}{w' S_t^k} \right)' S^k \quad (\text{A-9})$$

at any current segmentation  $S_t := \{S_t^k\}$  with means  $\mu_t^w := \{\mu_{S_t^k}^w\}$ .

*Proof.* The first expression follows from Th. 6 and formula (A-3) for  $F^w(S, m)$  at  $m = \mu_t^w$ . Also, (33) and  $\mathcal{K} = \phi' \phi$  imply the second expression for bound  $a_t(S)$ .  $\square$

The second expression for  $a_t(S)$  in Corollary 1 allows to obtain a linear bound for NC objective (41). For simplicity, assume positive definite affinity  $A$ . As follows from [52], [40], [58] and a simple derivation in our Sec. 1.3.1, normalized cut (41) with p.d. affinity  $A$  is equivalent to  $wk$ KM (36, A-2) with weights and kernel in (42)

$$w = d := A\mathbf{1} \quad \text{and} \quad \mathcal{K} = W^{-1} A W^{-1}.$$

Then, (A-9) implies the following linear bound for NC

$$\sum_k \left( d \frac{S_t^{k'w} A S_t^k}{(d' S_t^k)^2} - A S_t^k \frac{2}{d' S_t^k} \right)' S^k$$

that agrees with the *kernel bound* for NC in Table 2.

**Equivalence of weighted AA and AD to  $wk$ KM:** Figure 33 extends Figure 3 by relating weighted generalizations of standard pairwise clustering objectives to  $wk$ KM. The equivalence of objectives in Figure 33 can be verified by simple algebra. One additional simple property below is also needed. It is easy to prove.

**Proposition 1. (e.g. Roth et al. [38])** *For any symmetric matrix  $M$  define*

$$\tilde{M} := M + \delta I$$

where  $I$  is an identity matrix. Then, matrix  $\tilde{M}$  is positive semi-definite (psd) for any scalar  $\delta \geq -\lambda_0(M)$  where  $\lambda_0$  is the smallest eigen value of its argument.

## APPENDIX B (WEAK KERNEL K-MEANS)

For Hilbertian distortions  $\|\cdot\|_d = \|\cdot\|_k^2$  with p.s.d. kernels we can show that pairwise  $k$ KM approach (21) is “stronger” than a pointwise pKM approach (13) using the same metric. In this case pKM can be called *weak kernel K-means*, see Figure 34. Equivalent  $k$ KM formulation (18) guarantees more complex decision boundaries, see Fig.1(h), compared to pKM energy (13)

$$\begin{aligned} & \sum_k \sum_{p \in S^k} \|I_p - m_k\|_k^2 \quad (\text{B-1}) \\ & \equiv \sum_k \sum_{p \in S^k} \|\phi(I_p) - \phi(m_k)\|^2 \end{aligned}$$

with isometric kernel distance  $\|\cdot\|_k$  and some point  $m_k$  in the original space, Fig.1(g). Indeed, any  $m_k$  in the original space corresponds to some search point  $\phi(m_k)$  in the high-dimensional embedding space, while the opposite is false. Thus, optimization of (21) and (18) has larger search space than (B-1). It is also easy to check that energy (B-1) is an upper bound for (21) at any  $S$ . For this reason we refer to distortion energy (B-1) with kernel distance  $\|\cdot\|_k$  and explicit  $m_k$  in the original space as *weak kernel K-means*. Pointwise energy (B-1) is an example of pKM (13), while pairwise energy (21) with the same kernel metric is  $k$ KM.

Note that weak kernel K-means (B-1) for Gaussian kernel corresponds to *K-modes* closely related to *mean-shift* [110], [39], as discussed below. Some results comparing K-modes (weak  $k$ KM) to regular  $k$ KM are shown in Fig.1(g,h). Figure 34 illustrates general relations between kernel K-means (21) and probabilistic K-means (13,14). It includes a few examples discussed earlier and some more examples discussed below.

**K-modes and mean-shift:** Weak kernel K-means using unary formulation (B-1) with kernel distance  $\|\cdot\|_k$  and explicit optimization of  $m_k$  in the original data space is closely related to *K-modes* approach to clustering continuous [30] or discrete [111], [112] data. For example, for Gaussian kernel distance  $\|\cdot\|_k$  energy (B-1) becomes

$$- \sum_k \sum_{p \in S^k} e^{-\frac{\|I_p - m_k\|^2}{2\sigma^2}}$$

or, using Parzen densities  $\mathcal{P}_\sigma(\cdot | S^k)$  for points  $\{I_p | p \in S^k\}$ ,

$$= - \sum_k |S^k| \cdot \mathcal{P}_\sigma(m_k | S^k). \quad (\text{B-2})$$

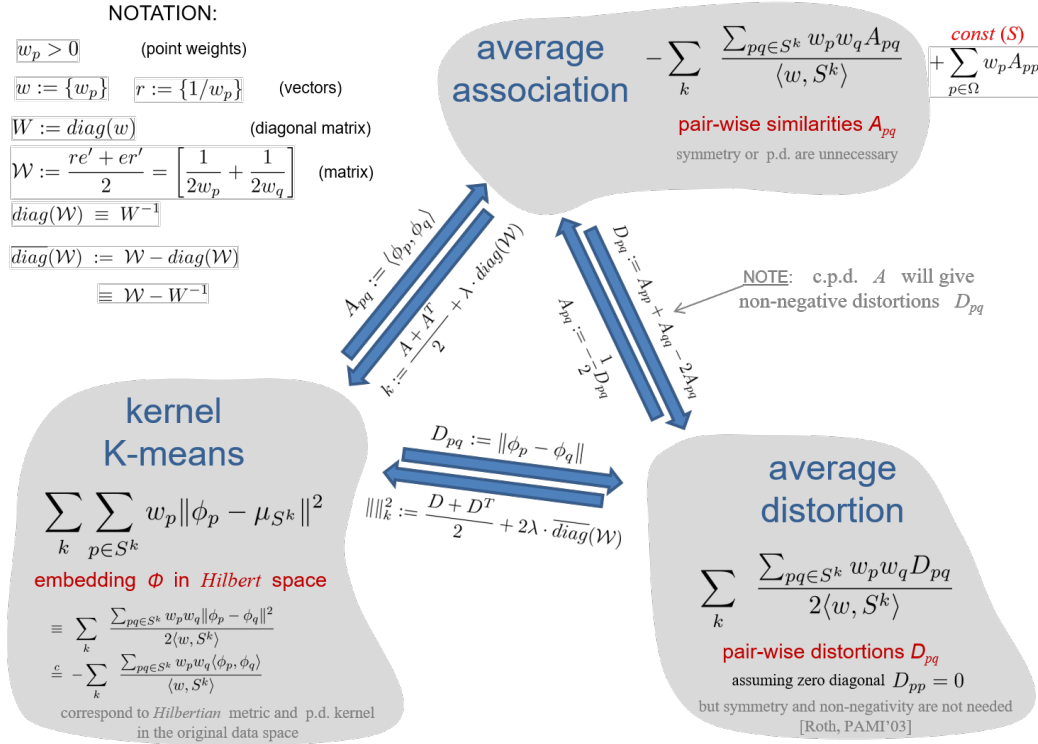


Fig. 33: Equivalence of *kernel K-means* (*kKM*), *average distortion* (*AD*), *average association* (*AA*) for the general case of weighted points. Typically, *kKM* is associated with *positive semi-definite* (p.s.d.) or *conditionally positive-definite* (c.p.d.) kernels [108] and Hilbertian distortions [47]. The above formulations of *AA* and *AD* make no assumptions for association matrix  $A$  and distortions  $D$  except for zero diagonal in  $D$ . Then, equivalence of *AD* and *AA* objectives (up to a constant) is straightforward. Roth et al. [38] reduce non-weighted case of *AD* to *kKM*. For arbitrary  $D$  they derive Hilbertian distortion  $\|k\|_k^2$  with an equivalent *AD* energy (up to a constant) and explicitly construct the corresponding embedding  $\phi$ . We show Hilbertian metric  $\|k\|_k^2$  for the general weighted case of *AD*, see *AD*→*kKM* above. Dhillon et al. [40], [58] prove that *normalized cuts* is a special case of weighted *kKM* and construct the corresponding p.d. kernel. Sec. 1.3.1 shows a simpler reduction of *normalized cuts* to weighted *kKM*. Similarly to [38], an equivalent p.d. kernel could be constructed for any association matrix  $A$ , see *AA*→*kKM* above. Note that the formulas for  $A$ -equivalent p.d. kernel and  $D$ -equivalent Hilbertian metric require some sufficiently large diagonal shift  $\delta$ . Roth et al. [38] relate proper  $\delta$  to the smallest eigen value of  $A = -\frac{D}{2}$ . Our weighted formulation requires the eigen value of  $\text{diag}(\mathcal{W})^{-\frac{1}{2}} \cdot A \cdot \text{diag}(\mathcal{W})^{-\frac{1}{2}}$ .

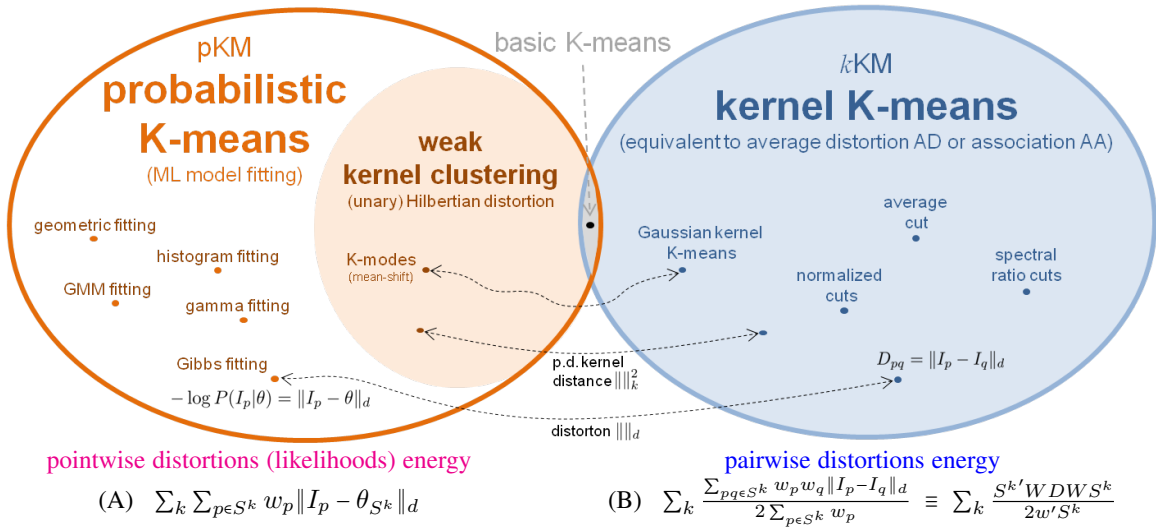


Fig. 34: Clustering with (A) pointwise and (B) pairwise distortion energies generalizing (13) and (26) for points with weights  $w = \{w_p\}$ . Pointwise distortion relates a data point and a model as log-likelihood function  $\|I_p - \theta\|_d = -\ln \mathcal{P}(I_p|\theta)$ . Pairwise distortion is defined by matrix  $D_{pq} = \|I_p - I_q\|_d$ . Weighted *AD* or *AA* for arbitrary metrics are equivalent to weighted *kKM*, see Figures 3 and 33. As shown in [38], [40] *average cut*, *normalized cut* [8], and *spectral ratio cut* [109] are examples of (weighted) *kKM*.

Clearly, optimal  $m_k$  are modes of Parzen densities in each segment. K-modes objective (B-2) can be seen as an energy-based formulation of mean-shift clustering [110], [39] with a fixed number of clusters. Formal objective allows to combine color clustering via (B-2) with geometric regularization in the image domain [29]. If needed, the number of clusters (modes) can be regularized by adding *label cost* [12]. In contrast, mean-shift segmentation [39] clusters RGBXY space combining color and spatial information. The number of clusters is indirectly controlled by the bandwidth.

Note that K-modes energy (B-2) follows from a weak  $k$ KM approach (B-1) for arbitrary positive normalized kernels. Such kernels define different Parzen densities, but they all lead to energy (B-2) where optimal  $m_k$  are modes of the corresponding densities. Therefore, different kernels in (B-1) give different modes in (B-2).

Many optimization methods can be used for K-modes energy. For example, it is possible to use iterative (block-coordinate descent) approach typical of K-means methods: one step reclusters points and the other step locally refinement the modes, e.g. using mean-shift operation [29]. For better optimization, local refinement of the mode in each cluster can be replaced by the best mode search tracing all points within each cluster using mean-shift. RANSAC-like sampling procedure can be used for some compromise between speed and quality. It is also possible to use exhaustive search for the strongest mode in each cluster over observed discrete features and then locally refine each cluster's mode with mean-shift.

It is also interesting that discrete version of K-modes for histograms [111], [112] define modes  $m_k = (m_k^1, \dots, m_k^j, \dots)$  combining *marginal modes* for all attributes or dimensions  $j$ . Implicitly, they use distortion  $\|\cdot\|_k$  for discrete kernel  $k(x, y) = \sum_j [x^j = y^j]$  where  $[\cdot]$  are *Iverson brackets*. Marginal modes could be useful for aggregating sparse high-dimensional data.

Analogously, we can also define a continuous kernel for *marginal modes* as

$$k(x, y) = \sum_j e^{\frac{-(x^j - y^j)^2}{2\sigma^2}}. \quad (\text{B-3})$$

Note that this is different from the standard Gaussian kernel

$$e^{\frac{-\|x - y\|^2}{2\sigma^2}} = \prod_j e^{\frac{-(x^j - y^j)^2}{2\sigma^2}},$$

which leads to regular modes energy (B-2). It is easy to check that kernel (B-3) corresponds to weak  $k$ KM energy

$$\begin{aligned} & - \sum_k \sum_j \sum_{p \in S^k} e^{\frac{-(I_p^j - m_k^j)^2}{2\sigma^2}} \\ &= - \sum_k |S_k| \cdot \sum_j \mathcal{P}_\sigma^j(m_k^j | S^k) \end{aligned}$$

where  $\mathcal{P}_\sigma^j$  is a marginal Parzen density for dimension  $j$ .

## APPENDIX C (ENTROPY CLUSTERING)

First, we show that (14) reduces to (15) for descriptive models. Indeed, assume  $\mathcal{P}(\theta) \equiv \mathcal{P}(\cdot | \theta)$  is a continuous density of a sufficiently descriptive class (e.g. GMM). For any function  $f(x)$  Monte-Carlo estimation gives for any subset  $S \subset \Omega$

$$\sum_{p \in S} f(I_p) \approx |S| \cdot \int f(x) d_s(x) dx \equiv |S| \cdot \langle f, d_s \rangle$$

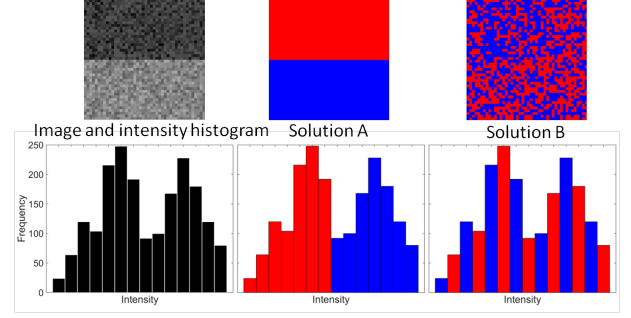


Fig. 35: *Histograms in color spaces.* Entropy criterion (15) with histograms can not tell a difference between A and B: bin permutations do not change the histogram's entropy.

where  $d_s$  is a “true” density for intensities  $\{I_p | p \in S\}$  and  $\langle \cdot, \cdot \rangle$  is a dot product. If  $f = -\log \mathcal{P}(\theta_s)$  and  $d_s \approx \mathcal{P}(\theta_s)$  then (14) implies (15) for differential entropy  $H(S) := H(\mathcal{P}(\theta_s))$ . For histograms  $\mathcal{P}_h(S) \equiv \mathcal{P}_h(\cdot | S)$  entropy-based interpretation (15) of (14) is exact for discrete entropy

$$H(S) := - \sum_x \mathcal{P}_h(x | S) \cdot \log \mathcal{P}_h(x | S) \equiv - \langle \mathcal{P}_h(S), \log \mathcal{P}_h(S) \rangle.$$

Intuitively, minimization of the entropy criterion (15) favors clusters with tight or “peaked” distributions. This criterion is widely used in categorical clustering [34] or decision trees [35], [36] where the entropy evaluates histograms over “naturally” discrete features. Below we discuss limitations of the entropy clustering criterion with either discrete histograms or continuous GMM densities in the context of color feature spaces.

**The case of histograms:** In this case the key problem for color space clustering is illustrated in Fig.35. Once continuous color space is broken into bins, the notion of proximity between the colors in the nearby bins is lost. Since bin permutations do not change the histogram entropy, criterion (15) can not distinguish the quality of clusterings A and B in Fig.35; some permutation of bins can make B look very similar to A.

**The case of GMM densities:** In this case the problem of entropy clustering (15) is different. In general, continuous density estimators commonly use Gaussian kernels, which preserve the notion of continuity in the color space. Indeed, the (differential) entropy for any reasonable continuous density estimate will see a significant difference between the clusters in A and B, see Fig.35.

We observe that the main issue for entropy criterion (15) with GMM densities is related to optimization problems. In this case high-order energies (15) or (14) require joint optimization of discrete variables  $S_p$  and a large number of additional continuous parameters for optimum GMM density  $\mathcal{P}(\cdot | \theta_S)$ . That is, the use of complex parametric probability models leads to complex high-order *mixed* objective functions. Typical block coordinate descent methods [23], [26] iterating optimization of  $S$  and  $\theta$  are sensitive to local minima, see Figures 2 and 1(e). Better solutions like Figure 1(f) have lower energy, but they can not be easily found unless initialization is very good.

These problems of pKM with histograms or GMM may explain why descriptive model fitting is not common in the learning community for clustering high-dimensional continuous spaces. Instead of pKM they often use a different extension of K-means, that is *kernel K-means* ( $k$ KM) or related pairwise clustering criteria like Normalize Cut (NC), see Sec.1.2.2 and 1.3.1.

## APPENDIX D (PSEUDO BOUND LEMMA)

**Lemma 2.** Consider function  $e : \{0, 1\}^{|\Omega|} \rightarrow \mathcal{R}^1$  defined by any symmetric matrix  $A$  and (strictly) positive vector  $w$  as

$$e(X) = -\frac{X'AX}{w'X}.$$

Function  $T_t$  is a pseudo-bound of  $e(X)$  at  $X_t$  for  $W := \text{diag}(w)$

$$T_t(X, \delta) := \nabla e(X_t)'X + \delta \left( \frac{(1 - 2X_t)'WX}{w'X_t} + 1 \right) \quad (\text{D-1})$$

where  $\nabla e(X) = w \frac{X'AX}{(w'X)^2} - AX \frac{2}{w'X}$ . Furthermore,  $T_t(X, \delta)$  is an auxiliary function for  $e(X)$  for all  $\delta \geq -\lambda_0(W^{-\frac{1}{2}}AW^{-\frac{1}{2}})$  where  $\lambda_0$  denotes the smallest eigen value of the matrix.

*Proof.* Diagonal shift  $\delta W$  for matrix  $A$  defines function

$$\widehat{e}_\delta(X) := -\frac{X'(\delta W + A)X}{w'X} \equiv e(X) - \delta \frac{X'WX}{w'X}.$$

According to Lemma 1 function  $\widehat{e}_\delta$  is concave for any  $\delta \geq -\lambda_0$  since  $(\delta W + A)$  is p.s.d. for such  $\delta$ . Thus, (53) defines a Taylor-based linear upper bound for  $\widehat{e}_\delta$  for  $\delta \geq -\lambda_0$

$$\nabla \widehat{e}_\delta(X_t)'X.$$

We have  $\widehat{e}_\delta(X) = e(X) - \delta$  for Boolean  $X$  where  $X'WX = w'X$ . Thus, the following upper bound is valid for optimizing  $e(X)$  over  $X \in \{0, 1\}^{|\Omega|}$  at  $\delta \geq -\lambda_0$

$$T_t(X, \delta) = \nabla \widehat{e}_\delta(X_t)'X + \delta. \quad (\text{D-2})$$

where the definition of  $\widehat{e}_\delta$  above yields gradient expression

$$\begin{aligned} \nabla \widehat{e}_\delta(X_t) &= \nabla e(X_t) - \delta \frac{2(w'X_t)WX_t - (X_t'WX_t)w}{(w'X_t)^2} \\ &= \nabla e(X_t) + \delta \frac{W(1 - 2X_t)}{w'X_t} \end{aligned}$$

where  $W1 = w$  for matrix  $W = \text{diag}(w)$  and  $X_t'WX_t = w'X_t$  for any  $X_t$  since all iterations explore only Boolean solutions.  $\square$

## APPENDIX E (PROOF OF Gini Bias THEOREM 5)

Let  $d_\Omega$  be a continuous probability density function over domain  $\Omega \subseteq \mathcal{R}^n$  defining conditional density

$$d_S(x) := d_\Omega(x|x \in S) \quad (\text{E-1})$$

for any non-empty subset  $S \subset \Omega$  and expectation

$$\mathbf{E}z := \int z(x)d_\Omega(x)dx$$

for any function  $z : \Omega \rightarrow \mathcal{R}^1$ .

Suppose  $\Omega$  is partitioned into two sets  $S$  and  $\bar{S}$  such that  $S \cup \bar{S} = \Omega$  and  $S \cap \bar{S} = \emptyset$ . Note that  $S$  here and in the statement of Theorem 5 is not a discrete set of observations, which is what  $S$  means in the rest of the paper. Theorem 5 states a property of a fully continuous version of Gini criterion (78) that follows from an additional application of Monte-Carlo estimation allowing to replace discrete set cardinality  $|S|$  by probability  $w$  of a continuous subset  $S$

$$w := \int_S d_\Omega(x)dx = \int d_\Omega(x) \cdot [x \in S]dx = \mathbf{E}[x \in S].$$

Then, minimization of  $E_G(S)$  in (78) corresponds to maximization of the following objective function

$$L(S) := w \int d_S^2(x)dx + (1 - w) \int d_{\bar{S}}^2(x)dx. \quad (\text{E-2})$$

Note that conditional density  $d_S$  in (E-1) can be written as

$$d_S(x) = d_\Omega(x) \cdot \frac{[x \in S]}{w} \quad (\text{E-3})$$

where  $[\cdot]$  is an indicator function. Eqs. (E-3) and (E-2) give

$$L(S) = \frac{1}{w} \int d_\Omega^2(x)[x \in S]dx + \frac{1}{1 - w} \int d_\Omega^2(x)[x \in \bar{S}]dx.$$

Introducing notation

$$I := [x \in S] \quad \text{and} \quad F := d_\Omega(x)$$

allows to further rewrite objective function  $L(S)$  as

$$L(S) = \frac{\mathbf{E}IF}{\mathbf{E}I} + \frac{\mathbf{E}F(1 - I)}{1 - \mathbf{E}I}.$$

Without loss of generality assume that  $\frac{\mathbf{E}F(1 - I)}{1 - \mathbf{E}I} \leq \frac{\mathbf{E}FI}{\mathbf{E}I}$  (the opposite case would yield a similar result). We now need the following lemma.

**Lemma 3.** Let  $a, b, c, d$  be some positive numbers, then

$$\frac{a}{b} \leq \frac{c}{d} \implies \frac{a}{b} \leq \frac{a + c}{b + d} \leq \frac{c}{d}.$$

*Proof.* Use reduction to a common denominator.  $\square$

Lemma 3 implies inequality

$$\frac{\mathbf{E}F(1 - I)}{1 - \mathbf{E}I} \leq \mathbf{E}F \leq \frac{\mathbf{E}FI}{\mathbf{E}I} \quad (\text{E-4})$$

which is needed to prove the Proposition below.

**Proposition 2. (Gini-bias)** Assume that subset  $S_\varepsilon \subset \Omega$  is

$$S_\varepsilon := \{x : d_\Omega(x) \geq \sup_x d_\Omega(x) - \varepsilon\}. \quad (\text{E-5})$$

Then

$$\sup_S L(S) = \lim_{\varepsilon \rightarrow 0} L(S_\varepsilon) = \mathbf{E}d_\Omega + \sup_x d_\Omega(x). \quad (\text{E-6})$$

*Proof.* Due to monotonicity of expectation we have

$$\frac{\mathbf{E}FI}{\mathbf{E}I} \leq \frac{\mathbf{E}(I \sup_x d_\Omega(x))}{\mathbf{E}I} = \sup_x d_\Omega(x). \quad (\text{E-7})$$

Then (E-4) and (E-7) imply

$$L(S) = \frac{\mathbf{E}FI}{\mathbf{E}I} + \frac{\mathbf{E}F(1 - I)}{1 - \mathbf{E}I} \leq \sup_x d_\Omega(x) + \mathbf{E}F. \quad (\text{E-8})$$

That is, the right part of (E-6) is an upper bound for  $L(S)$ .

Let  $I_\varepsilon \equiv [x \in S_\varepsilon]$ . It is easy to check that

$$\lim_{\varepsilon \rightarrow 0} \frac{\mathbf{E}F(1 - I_\varepsilon)}{1 - \mathbf{E}I_\varepsilon} = \mathbf{E}F. \quad (\text{E-9})$$

Definition (E-5) also implies

$$\lim_{\varepsilon \rightarrow 0} \frac{\mathbf{E}FI_\varepsilon}{\mathbf{E}I_\varepsilon} \geq \lim_{\varepsilon \rightarrow 0} \frac{\mathbf{E}(\sup_x d_\Omega(x) - \varepsilon)I_\varepsilon}{\mathbf{E}I_\varepsilon} = \sup_x d_\Omega(x).$$

This result and (E-7) conclude that

$$\lim_{\varepsilon \rightarrow 0} \frac{\mathbf{E}FI_\varepsilon}{\mathbf{E}I_\varepsilon} = \sup_x d_\Omega(x). \quad (\text{E-10})$$

Finally, the limits in (E-9) and (E-10) imply

$$\begin{aligned} \lim_{\varepsilon \rightarrow 0} L(S_\varepsilon) &= \lim_{\varepsilon \rightarrow 0} \frac{\mathbf{E}F(1 - I_\varepsilon)}{1 - \mathbf{E}I_\varepsilon} + \lim_{\varepsilon \rightarrow 0} \frac{\mathbf{E}FI_\varepsilon}{\mathbf{E}I_\varepsilon} \\ &= \mathbf{E}d_\Omega + \sup_x d_\Omega(x). \end{aligned}$$

This equality and bound (E-8) prove (E-6).  $\square$



## ACKNOWLEDGEMENTS

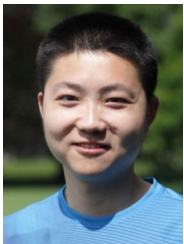
We would like to thank Carl Olsson (Lund University) for highly stimulating discussions and useful feedback at different stages of the project. Anders Eriksson (Lund University) helped with related work. We also thank Jianbo Shi (UPenn) for his feedback and for his spectral-relaxation optimization code for normalized cuts.

## REFERENCES

- [1] S. Geman and D. Geman, "Stochastic relaxation, Gibbs distributions, and the Bayesian restoration of images," *IEEE transactions on Pattern Analysis and Machine Intelligence*, vol. 6, pp. 721–741, 1984. **1**
- [2] D. Mumford and J. Shah, "Optimal approximations by piecewise smooth functions and associated variational problems," *Comm. Pure Appl. Math.*, vol. 42, pp. 577–685, 1989. **1**
- [3] V. Caselles, R. Kimmel, and G. Sapiro, "Geodesic active contours," *International Journal of Computer Vision*, vol. 22, no. 1, pp. 61–79, 1997. **1, 2**
- [4] Y. Boykov and M.-P. Jolly, "Interactive graph cuts for optimal boundary & region segmentation of objects in N-D images," in *ICCV*, vol. I, July 2001, pp. 105–112. **1, 2, 8, 23**
- [5] Y. Boykov and V. Kolmogorov, "Computing geodesics and minimal surfaces via graph cuts," in *International Conference on Computer Vision*, vol. I, 2003, pp. 26–33. **1, 2**
- [6] T. Pock, A. Chambolle, D. Cremers, and H. Bischof, "A convex relaxation approach for computing minimal partitions," in *IEEE conference on Computer Vision and Pattern Recognition (CVPR)*, 2009. **1**
- [7] C. C. Aggarwal and C. K. Reddy, Eds., *Data Clustering: Algorithms and Applications*. Chapman & Hall / CRC, 2014. **1**
- [8] J. Shi and J. Malik, "Normalized cuts and image segmentation," *IEEE Transactionson Pattern Analysis and Machine Intelligence (PAMI)*, vol. 22, pp. 888–905, 2000. **1, 3, 4, 5, 6, 7, 8, 11, 12, 13, 15, 17, 19, 20, 30**
- [9] S. Li, *Markov Random Field Modeling in Image Analysis*, 3rd ed. Springer-Verlag, 2009. **1**
- [10] Y. Boykov, O. Veksler, and R. Zabih, "Fast approximate energy minimization via graph cuts," *IEEE transactions on Pattern Analysis and Machine Intelligence*, vol. 23, no. 11, pp. 1222–1239, November 2001. **1, 2, 8, 11, 17**
- [11] P. Kohli, P. H. Torr *et al.*, "Robust higher order potentials for enforcing label consistency," *International Journal of Computer Vision*, vol. 82, no. 3, pp. 302–324, 2009. **1, 2, 8, 11, 20, 21**
- [12] A. Delong, A. Osokin, H. Isack, and Y. Boykov, "Fast Approximate Energy Minimization with Label Costs," *Int. J. of Computer Vision (IJCV)*, vol. 96, no. 1, pp. 1–27, January 2012. **1, 2, 3, 5, 8, 11, 20, 31**
- [13] K. Park and S. Gould, "On learning higher-order consistency potentials for multi-class pixel labeling," in *ECCV*, 2012. **2, 20**
- [14] M. Tang, L. Gorelick, O. Veksler, and Y. Boykov, "Grabcut in one cut," in *International Conference on Computer Vision (ICCV)*, Sydney, Australia, December 2013. **2, 3, 8, 20**
- [15] J. S. Yedidia, W. T. Freeman, and Y. Weiss, "Constructing free-energy approximations and generalized belief propagation algorithms," *IEEE Transactions on Information Theory*, vol. 51, no. 7, pp. 2282–2312, 2005. **2**
- [16] V. Kolmogorov, "Convergent tree-reweighted message passing for energy minimization," *Pattern Analysis and Machine Intelligence, IEEE Transactions on*, vol. 28, no. 10, pp. 1568–1583, 2006. **2**
- [17] T. Werner, "A linear programming approach to max-sum problem: A review," *Pattern Analysis and Machine Intelligence, IEEE Transactions on*, vol. 29, no. 7, pp. 1165–1179, 2007. **2, 11**
- [18] J. H. Kappes, B. Andres, F. A. Hamprecht, C. Schnörr, S. Nowozin, D. Batra, S. Kim, B. X. Kausler, T. Kröger, J. Lellmann *et al.*, "A comparative study of modern inference techniques for structured discrete energy minimization problems," *International Journal of Computer Vision*, vol. 115, no. 2, pp. 155–184, 2015. **2**
- [19] A. Chambolle, "An algorithm for total variation minimization and applications," *Journal of Mathematical imaging and vision*, vol. 20, no. 1-2, pp. 89–97, 2004. **2, 11**
- [20] A. Chambolle and T. Pock, "A first-order primal-dual algorithm for convex problems with applications to imaging," *Journal of Mathematical Imaging and Vision*, vol. 40, no. 1, pp. 120–145, 2011. **2, 11**
- [21] D. Cremers, M. Rousson, and R. Deriche, "A review of statistical approaches to level set segmentation: integrating color, texture, motion and shape," *International journal of computer vision*, vol. 72, no. 2, pp. 195–215, 2007. **2, 11**
- [22] Y. Boykov and G. Funka-Lea, "Graph cuts and efficient N-D image segmentation," *International Journal of Computer Vision (IJCV)*, vol. 70, no. 2, pp. 109–131, 2006. **2**
- [23] S. C. Zhu and A. Yuille, "Region competition: Unifying snakes, region growing, and Bayes/MDL for multiband image segmentation," *IEEE Trans. on Pattern Analysis and Machine Intelligence*, vol. 18, no. 9, pp. 884–900, Sept. 1996. **2, 3, 5, 8, 31**
- [24] T. Chan and L. Vese, "Active contours without edges," *IEEE Trans. Image Processing*, vol. 10, no. 2, pp. 266–277, 2001. **2, 8**
- [25] I. B. Ayed, A. Mitiche, and Z. Belhadj, "Multiregion level set partitioning of synthetic aperture radar images," *IEEE Transactions on Pattern Analysis and Machine Intelligence (PAMI)*, vol. 27, no. 5, pp. 793–800, 2005. **2, 3, 5**
- [26] C. Rother, V. Kolmogorov, and A. Blake, "Grabcut - interactive foreground extraction using iterated graph cuts," in *ACM trans. on Graphics (SIGGRAPH)*, 2004. **2, 3, 5, 8, 20, 21, 23, 25, 31**
- [27] M. Kearns, Y. Mansour, and A. Ng, "An Information-Theoretic Analysis of Hard and Soft Assignment Methods for Clustering," in *Conf. on Uncertainty in Artificial Intelligence (UAI)*, August 1997. **2, 3, 5, 8, 9, 18, 19**
- [28] R. O. Duda, P. E. Hart, and D. G. Stork, *Pattern Classification*. John Wiley & Sons, 2001. **2, 5, 28**
- [29] M. B. Salah, A. Mitiche, and I. B. Ayed, "Effective level set image segmentation with a kernel induced data term," *IEEE Transactions on Image Processing*, vol. 19, no. 1, pp. 220–232, 2010. **2, 5, 7, 31**
- [30] M. A. Carreira-Perpinan and W. Wang, "The K-Modes Algorithm for Clustering," in *arXiv:1304.6478v1 [cs.LG]*, April 2013. **2, 29**
- [31] K. K. Sung and T. Poggio, "Example based learning for viewbased human face detection," *IEEE Trans. on Pattern Analysis and Machine Intelligence (TPAMI)*, vol. 20, pp. 39–51, 1995. **3, 5**
- [32] M. Rousson and D. R., "A variational framework for active and adaptive segmentation of vector valued images," in *Workshop on Motion and Video Computing*, 2002. **3, 5**
- [33] A. Mitiche and I. B. Ayed, *Variational and Level Set Methods in Image Segmentation*. Springer, 2010. **3**
- [34] T. Li, S. Ma, and M. Ogihara, "Entropy-based criterion in categorical clustering," in *Int. Conf. on M. Learning*, 2004. **3, 31**
- [35] L. Breiman, "Technical note: Some properties of splitting criteria," *Machine Learning*, vol. 24, no. 1, pp. 41–47, 1996. **3, 5, 18, 31**
- [36] G. Louppe, L. Wehenkel, A. Suter, and P. Geurts, "Understanding variable importances in forests of randomized trees," in *NIPS*, 2013, pp. 431–439. **3, 18, 31**
- [37] M. Tang, I. B. Ayed, and Y. Boykov, "Pseudo-bound optimization for binary energies," in *European Conference on Computer Vision (ECCV)*, 2014, pp. 691–707. **3, 9, 16, 17, 18**
- [38] V. Roth, J. Laub, M. Kawanabe, and J. Buhmann, "Optimal cluster preserving embedding of nonmetric proximity data," *IEEE Transactions on Pattern Analysis and Machine Intelligence (PAMI)*, vol. 25, no. 12, pp. 1540–1551, 2003. **5, 6, 7, 10, 12, 13, 14, 29, 30**
- [39] D. Comaniciu and P. Meer, "Mean shift: a robust approach toward feature space analysis," *IEEE Transactions on Pattern Analysis and Machine Intelligence (PAMI)*, vol. 24, no. 5, pp. 603–619, 2002. **5, 7, 29, 31**
- [40] I. Dhillon, Y. Guan, and B. Kulis, "Kernel k-means, spectral clustering and normalized cuts," in *KDD*, 2004. **4, 5, 6, 7, 13, 14, 15, 20, 21, 29, 30**
- [41] M. Tang, I. B. Ayed, D. Marin, and Y. Boykov, "Secrets of grabcut and kernel k-means," in *International Conference on Computer Vision (ICCV)*, Santiago, Chile, December 2015. **5, 8, 9, 23**
- [42] V. Vapnik, *Statistical Learning Theory*. Wiley, 1998. **4**
- [43] K. Muller, S. Mika, G. Ratsch, K. Tsuda, and B. Scholkopf, "An introduction to kernel-based learning algorithms," *IEEE Trans. on Neural Networks*, vol. 12, no. 2, pp. 181–201, 2001. **4**
- [44] M. Girolami, "Mercer kernel-based clustering in feature space," *IEEE Transactions on Neural Networks*, vol. 13, no. 3, pp. 780–784, 2002. **4, 18**
- [45] R. Chitta, R. Jin, T. C. Havens, and A. K. Jain, "Scalable kernel clustering: Approximate kernel k-means," in *KDD*, 2011, pp. 895–903. **4**
- [46] S. Jayasumana, R. Hartley, M. Salzmann, H. Li, and M. Harandi, "Kernel methods on riemannian manifolds with gaussian rbf kernels," *IEEE Transactions on Pattern Analysis and Machine Intelligence*, vol. In press, 2015. **4**
- [47] M. Hein, T. N. Lal, and O. Bousquet, "Hilbertian metrics on probability measures and their application in svms," *Pattern Recognition*, vol. LNCS 3175, pp. 270–277, 2004. **4, 30**

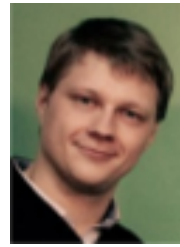
- [48] M. Belkin and P. Niyogi, "Laplacian eigenmaps for dimensionality reduction and data representation," *Neural computation*, vol. 15, no. 6, pp. 1373–1396, 2003. **4, 12, 15**
- [49] Y. Yu, C. Fang, and Z. Liao, "Piecewise flat embedding for image segmentation," in *Proceedings of the IEEE International Conference on Computer Vision*, 2015, pp. 1368–1376. **4, 12, 15**
- [50] J. Shawe-Taylor and N. Cristianini, *Kernel Methods for Pattern Analysis*. Cambridge University Press, 2004. **4, 29**
- [51] K.-R. Müller, S. Mika, G. Rätsch, K. Tsuda, and B. Schölkopf, "An introduction to kernel-based learning algorithms," *IEEE Transactions on Neural Networks*, vol. 12, no. 2, pp. 181–201, 2001. **4**
- [52] F. Bach and M. Jordan, "Learning spectral clustering," *Advances in Neural Information Processing Systems (NIPS)*, vol. 16, pp. 305–312, 2003. **6, 7, 12, 13, 15, 29**
- [53] I. Cox, S. Rao, and Y. Zhong, "Ratio Regions": A Technique for Image Segmentation," in *International Conference on Pattern Recognition (ICPR)*, 1996, pp. 557–564. **7**
- [54] I. Jermyn and H. Ishikawa, "Globally optimal regions and boundaries as minimum point weight cycles," *IEEE Transactions on Pattern Analysis and Machine Intelligence (PAMI)*, vol. 23, no. 10, pp. 1075–1088, 2001. **7**
- [55] S. Wang and J. M. Siskind, "Image segmentation with ratio cut," *IEEE Transactions on Pattern Analysis and Machine Intelligence (PAMI)*, vol. 25, no. 6, pp. 675–690, 2003. **7**
- [56] V. Kolmogorov, Y. Boykov, and C. Rother, "Applications of parametric maxflow in computer vision," in *IEEE International Conference on Computer Vision (ICCV)*, 2007. **7, 16, 17**
- [57] D. S. Hochbaum, "Polynomial time algorithms for ratio regions and a variant of normalized cut," *IEEE Transactions on Pattern Analysis and Machine Intelligence*, vol. 32, no. 5, pp. 889–898, 2010. **7**
- [58] I. Dhillon, Y. Guan, and B. Kulis, "Weighted graph cuts without eigenvectors: A multilevel approach," *IEEE Transactions on Pattern Analysis and Machine Learning (PAMI)*, vol. 29, no. 11, pp. 1944–1957, November 2007. **7, 13, 29, 30**
- [59] S. Yu and J. Shi, "Multiclass spectral clustering," in *International Conference on Computer Vision (ICCV)*, 2003. **7, 15**
- [60] T. Hofmann and J. Buhmann, "Pairwise data clustering by deterministic annealing," *IEEE Transactions on Pattern Analysis and Machine Intelligence (PAMI)*, vol. 19, no. 1, pp. 1–14, January 1997. **7**
- [61] R. Duda, P. Hart, and D. Stork, *Pattern classification*. John Wiley & Sons, 2001. **7**
- [62] B. Kulis, S. Basu, I. Dhillon, and R. Mooney, "Semi-supervised graph clustering: a kernel approach," *Machine Learning*, vol. 74, no. 1, pp. 1–22, January 2009. **7, 8**
- [63] S. X. Yu and J. Shi, "Segmentation given partial grouping constraints," *IEEE Transactions on Pattern Analysis and Machine Intelligence (PAMI)*, vol. 26, no. 2, pp. 173–183, 2004. **7, 8**
- [64] L. Xu, W. Li, and D. Schuurmans, "Fast normalized cut with linear constraints," in *IEEE Conf. on Computer Vision and Pattern Recognition (CVPR)*, 2009, pp. 2866–2873. **7**
- [65] A. Eriksson, C. Olsson, and F. Kahl, "Normalized cuts revisited: A reformulation for segmentation with linear grouping constraints," *Journal of Mathematical Imaging and Vision*, vol. 39, no. 1, pp. 45–61, 2011. **7, 8**
- [66] J. Malik, S. Belongie, T. Leung, and J. Shi, "Contour and texture analysis for image segmentation," *International journal of computer vision*, vol. 43, no. 1, pp. 7–27, 2001. **8, 15, 20**
- [67] P. Arbelaez, M. Maire, C. Fowlkes, and J. Malik, "Contour detection and hierarchical image segmentation," *Pattern Analysis and Machine Intelligence, IEEE Transactions on*, vol. 33, no. 5, pp. 898–916, 2011. **8, 15, 16, 20, 21**
- [68] S. E. Chew and N. D. Cahill, "Semi-supervised normalized cuts for image segmentation," in *The IEEE International Conference on Computer Vision (ICCV)*, December 2015. **8**
- [69] P. Krahenbuhl and V. Koltun, "Efficient inference in fully connected CRFs with Gaussian edge potentials," in *NIPS*, 2011. **8**
- [70] K. Lange, D. R. Hunter, and I. Yang, "Optimization transfer using surrogate objective functions," *Journal of Computational and Graphical Statistics*, vol. 9, no. 1, pp. 1–20, 2000. **9**
- [71] M. Narasimhan and J. A. Bilmes, "A submodular-supermodular procedure with applications to discriminative structure learning," in *UAI*, 2005, pp. 404–412. **9**
- [72] I. Ben Ayed, L. Gorelick, and Y. Boykov, "Auxiliary cuts for general classes of higher order functionals," in *IEEE conference on Computer Vision and Pattern Recognition (CVPR)*, Portland, Oregon, June 2013, pp. 1304–1311. [Online]. Available: <http://www.csd.uwo.ca/~yuri/Abstracts/cvpr13-auxcut-abs.shtml> **9, 17**
- [73] H. Ishikawa, "Exact optimization for Markov Random Fields with convex priors," *IEEE transactions on Pattern Analysis and Machine Intelligence*, vol. 25, no. 10, pp. 1333–1336, 2003. **11**
- [74] V. Kolmogorov, "Convergent Tree-Reweighted Message Passing for Energy Minimization," *IEEE transactions on Pattern Analysis and Machine Intelligence*, vol. 28, no. 10, pp. 1568–1583, October 2006. **11**
- [75] T. F. Cox and M. A. Cox, *Multidimensional scaling*. CRC Press, 2000. **12, 13**
- [76] A. Ng, M. Jordan, and Y. Weiss, "On spectral clustering: analysis and an algorithm," in *Advances in neural information processing systems (NIPS)*, vol. 2, 2002, pp. 849–856. **12, 15**
- [77] G. H. Golub and C. F. Van Loan, *Matrix computations*. JHU Press, 2012, vol. 3. **12**
- [78] U. Von Luxburg, "A tutorial on spectral clustering," *Statistics and computing*, vol. 17, no. 4, pp. 395–416, 2007. **13, 15**
- [79] Y. Boykov, O. Veksler, and R. Zabih, "Fast approximate energy minimization via graph cuts," *Pattern Analysis and Machine Intelligence, IEEE Transactions on*, vol. 23, no. 11, pp. 1222–1239, 2001. **14**
- [80] S. Belongie and J. Malik, "Finding boundaries in natural images: A new method using point descriptors and area completion," in *Proceedings of the European Conference on Computer Vision (ECCV)*, 1998. **15**
- [81] L. Gorelick, F. R. Schmidt, and Y. Boykov, "Fast trust region for segmentation," in *IEEE conference on Computer Vision and Pattern Recognition (CVPR)*, Portland, Oregon, June 2013, pp. 1714–1721. [Online]. Available: <http://www.csd.uwo.ca/~yuri/Abstracts/cvpr13-itr-abs.shtml> **16, 18**
- [82] S. Vicente, V. Kolmogorov, and C. Rother, "Joint optimization of segmentation and appearance models," in *International Conf. on Computer Vision (ICCV)*, 2009. **17, 20**
- [83] I. Ben Ayed, H.-M. Chen, K. Punithakumar, I. Ross, and S. Li, "Graph cut segmentation with a global constraint: Recovering region distribution via a bound of the bhattacharyya measure," in *CVPR*, 2010, pp. 3288–3295. **17**
- [84] C. M. Bishop, *Pattern Recognition and Machine Learning*. Springer, August 2006. **18, 19**
- [85] Y. Boykov, H. N. Isack, C. Olsson, and I. B. Ayed, "Volumetric bias in segmentation and reconstruction: Secrets and solutions," *CoRR*, vol. abs/1505.00218, 2015. **18, 19**
- [86] J. Nash, "The imbedding problem for riemannian manifolds," *Annals of Mathematics*, vol. 63, no. 1, pp. 20–63, 1956. **19**
- [87] T. Brox and J. Malik, "Large displacement optical flow: descriptor matching in variational motion estimation," *IEEE Transactions on Pattern Analysis and Machine Intelligence*, vol. 33, no. 3, pp. 500–513, 2011. **20, 25, 26, 27**
- [88] V. Lempitsky, A. Blake, and C. Rother, "Image segmentation by branch-and-mincut," in *ECCV*, 2008. **20**
- [89] A. Oliva and A. Torralba, "Modeling the shape of the scene: A holistic representation of the spatial envelope," *International journal of computer vision*, vol. 42, no. 3, pp. 145–175, 2001. **20, 21**
- [90] S. Paris and F. Durand, "A fast approximation of the bilateral filter using a signal processing approach," in *Computer Vision—ECCV 2006*. Springer, 2006, pp. 568–580. **20**
- [91] A. Adams, J. Baek, and M. A. Davis, "Fast high-dimensional filtering using the permutohedral lattice," *Computer Graphics Forum*, vol. 29, no. 2, pp. 753–762, 2010. **20**
- [92] M. D. Collins, J. Liu, J. Xu, L. Mukherjee, and V. Singh, "Spectral clustering with a convex regularizer on millions of images," in *Computer Vision—ECCV 2014*. Springer, 2014, pp. 282–298. **20, 21**
- [93] V. Lempitsky, P. Kohli, C. Rother, and T. Sharp, "Image segmentation with a bounding box prior," in *Int. Conference on Computer Vision (ICCV)*, 2009, pp. 277–284. **22**
- [94] K. McGuinness and N. E. Oconnor, "A comparative evaluation of interactive segmentation algorithms," *Pattern Recognition*, vol. 43, no. 2, pp. 434–444, 2010. **23**
- [95] C. Nieuwenhuis and D. Cremers, "Spatially varying color distributions for interactive multilabel segmentation," *IEEE transactions on pattern analysis and machine intelligence*, vol. 35, no. 5, pp. 1234–1247, 2013. **23**
- [96] D. Martin, C. Fowlkes, D. Tal, and J. Malik, "A database of human segmented natural images and its application to evaluating segmentation algorithms and measuring ecological statistics," in *Computer Vision, 2001. ICCV 2001. Proceedings. Eighth IEEE International Conference on*, vol. 2. IEEE, 2001, pp. 416–423. **23**
- [97] M. Varma and A. Zisserman, "A statistical approach to texture classification from single images," *International Journal of Computer Vision*, vol. 62, no. 1–2, pp. 61–81, 2005. **23**

- [98] P. K. Nathan Silberman, Derek Hoiem and R. Fergus, "Indoor segmentation and support inference from rgbd images," in *ECCV*, 2012. 24, 25
- [99] M. Dou, J. Taylor, H. Fuchs, A. Fitzgibbon, and S. Izadi, "3d scanning deformable objects with a single rgbd sensor," in *Proceedings of the IEEE Conference on Computer Vision and Pattern Recognition*, 2015, pp. 493–501. 24
- [100] R. A. Newcombe, S. Izadi, O. Hilliges, D. Molyneaux, D. Kim, A. J. Davison, P. Kohi, J. Shotton, S. Hodges, and A. Fitzgibbon, "Kinect-fusion: Real-time dense surface mapping and tracking," in *Mixed and augmented reality (ISMAR), 2011 10th IEEE international symposium on*. IEEE, 2011, pp. 127–136. 24
- [101] Z. Deng, S. Todorovic, and L. J. Latecki, "Semantic segmentation of rgbd images with mutex constraints," in *International Conference on Computer Vision (ICCV)*, Santiago, Chile, December 2015. 24
- [102] V. Gulshan, V. Lempitsky, and A. Zisserman, "Humanising grabcut: Learning to segment humans using the kinect," in *Computer Vision Workshops (ICCV Workshops), 2011 IEEE International Conference on*. IEEE, 2011, pp. 1127–1133. 24
- [103] X. Ren, L. Bo, and D. Fox, "Rgb(d) scene labeling: Features and algorithms," in *Computer Vision and Pattern Recognition (CVPR), 2012 IEEE Conference on*. IEEE, 2012, pp. 2759–2766. 24
- [104] J.-M. Gottfried, J. Fehr, and C. S. Garbe, "Computing range flow from multi-modal kinect data," in *Advances in Visual Computing*. Springer, 2011, pp. 758–767. 24
- [105] T. Brox and J. Malik, "Object segmentation by long term analysis of point trajectories," in *Computer Vision—ECCV 2010*. Springer, 2010, pp. 282–295. 25, 26, 27
- [106] M. Menze and A. Geiger, "Object scene flow for autonomous vehicles," in *Conference on Computer Vision and Pattern Recognition (CVPR)*, 2015. 25, 28
- [107] P. Ochs and T. Brox, "Object segmentation in video: a hierarchical variational approach for turning point trajectories into dense regions," in *Computer Vision (ICCV), 2011 IEEE International Conference on*. IEEE, 2011, pp. 1583–1590. 25
- [108] B. Schölkopf, "The kernel trick for distances," in *Advances in Neural Information Processing Systems (NIPS)*, 2001, pp. 301–307. 30
- [109] P. Chan, M. Schlag, and J. Zien, "Spectral k-way ratio cut partitioning," vol. 13, pp. 1088–1096, 1994. 30
- [110] Y. Cheng, "Mean shift, mode seeking, and clustering," *IEEE Transactions on Pattern Analysis and Machine Intelligence (PAMI)*, vol. 17, no. 8, pp. 790–799, 1995. 29, 31
- [111] Z. Huang, "Extensions to the k-means algorithm for clustering large data sets with categorical values," *Data mining and knowledge discovery*, vol. 2, no. 3, pp. 283–304, 1998. 29, 31
- [112] A. Chaturvedi, P. E. Green, and J. D. Carroll, "K-modes clustering," *Journal of Classification*, vol. 18, no. 1, pp. 35–55, 2001. 29, 31



**Meng Tang** is a PhD candidate in computer science at the University of Western Ontario, Canada, supervised by Prof. Yuri Boykov. He obtained MSc in computer science in 2014 from the same institution for his thesis titled "Color Separation for Image Segmentation". Previously in 2012 he received B.E. in Automation from the Huazhong University of Science and Technology, China. He is interested in image segmentation and semi-supervised data clustering. He is also obsessed and has experiences on discrete

optimization problems for computer vision and machine learning.



supervision of Yuri Boykov. His research is focused on designing general unsupervised and semi-supervised methods for accurate image segmentation and object delineation.



**Ismail Ben Ayed** received the PhD degree (with the highest honor) in computer vision from the Institut National de la Recherche Scientifique (INRS-EMT), Montreal, QC, in 2007. He is currently Associate Professor at the Ecole de Technologie Supérieure (ETS), University of Quebec, where he holds a research chair on Artificial Intelligence in Medical Imaging. Before joining the ETS, he worked for 8 years as a research scientist at GE Healthcare, London, ON, conducting research in medical image analysis. He

also holds an adjunct professor appointment at the University of Western Ontario (since 2012). Ismail's research interests are in computer vision, optimization, machine learning and their potential applications in medical image analysis.



**Yuri Boykov** received "Diploma of Higher Education" with honors at Moscow Institute of Physics and Technology (department of Radio Engineering and Cybernetics) in 1992 and completed his Ph.D. at the department of Operations Research at Cornell University in 1996. He is currently a full professor at the department of Computer Science at the University of Western Ontario. His research is concentrated in the area of computer vision and biomedical image analysis. In particular, he is interested in problems

of early vision, image segmentation, restoration, registration, stereo, motion, model fitting, feature-based object recognition, photo-video editing and others. He is a recipient of the Helmholtz Prize (Test of Time) awarded at International Conference on Computer Vision (ICCV), 2011 and Florence Bucke Science Award, Faculty of Science, The University of Western Ontario, 2008.